Dissertation
zur Erlangung der Doktorwürde
an der
Gesamtfakultät für Mathematik,
Ingenieur- und Naturwissenschaften
der
Ruprecht-Karls-Universität Heidelberg

Thema:

Identifying ferroelectricity in organic compounds

vorgelegt von:

Maximilian Litterst

Gutachter: Professor Dr. Martin Kemerink
Professor Dr. Alexander Colsmann

Abstract

A. English

Organic ferroelectric materials promise flexible, biocompatible, and easily fabricated alternatives to their inorganic counterparts for applications in, amongst others, sensors, actuators and memory. However, their widespread adoption is hindered by a persistent performance gap. Closing this gap requires the discovery of novel materials with superior intrinsic properties, alongside a deeper understanding of the structure-property relationships that govern their behavior. This thesis presents an experimental investigation of several organic compounds recently identified by a data-mining study as potential room-temperature ferroelectrics. The primary goals were to validate these predictions, characterize novel ferroelectric phenomena, and ultimately refine the predictive screening process.

Polycrystalline thin films of the candidate materials were electrically investigated using capacitance-voltage spectroscopy and polarization hysteresis measurements. Despite large differences in stability and background conductivity, all compounds exhibited ferroelectric behavior at room temperature, with relatively large polarization and small coercive field values. Specifically, the ferroelectric properties of one material show a strong dependency on the ambient humidity, whereas another showed a strong coupling between background conductivity and ferroelectric switching. Of the remaining two compounds, one was found to be unstable at room temperature whereas the other displayed multiple polymorphs, complicating reproducibility and limiting their practical potential.

Given its unique humidity-dependence, the first material was investigated in detail with frequency-, temperature- and humidity-dependent ferroelectric switching measurements. We observed a pronounced dependence of the ferroelectric properties on switching frequency, temperature and, strikingly, ambient humidity. Interestingly, the ferroelectric behavior appears to be coupled to the complex electrical conductivity. We interpret our findings in terms of a multi-step polarization reversal mechanism, involving a combination of proton transfer and molecular rotations, where the former is thought to also be responsible for the observed long-range charge transport. These properties may find application in new classes of tunable or environment-responsive ‘smart’ materials. Overall, this work not only introduces new functional organic materials but also confirms that data-mining strategies are a powerful paradigm for accelerating their discovery and builds a basis on which these studies can be improved upon.

B. German

Organische Ferroelektrika versprechen flexible, biokompatible und leicht herstellbare Alternativen zu ihren anorganischen Gegenstücken für Anwendungen unter anderem in Sensoren, Aktuatoren und Speichermedien. Ihre breite Anwendung wird jedoch durch ein anhaltendes Leistungsdefizit erschwert. Das Schließen dieser Lücke erfordert die Entdeckung neuartiger Materialien mit überlegenen intrinsischen Eigenschaften sowie ein tieferes Verständnis der Struktur-Eigenschafts-Beziehungen, die ihr Verhalten bestimmen.

Diese Arbeit präsentiert eine experimentelle Untersuchung mehrerer organischer Verbindungen, die kürzlich durch eine Datenbank-Studie als potenzielle Raumtemperatur-Ferroelektrika identifiziert wurden. Die Hauptziele bestanden darin, diese Vorhersagen zu validieren, neuartige ferroelektrische Phänomene zu charakterisieren und letztendlich den prädiktiven Screening-Prozess zu verfeinern.

Polykristalline Dünnschichten der Kandidatenmaterialien wurden mittels Kapazitäts-Spannungs-Spektroskopie und Polarisations-Hysterese-Messungen elektrisch untersucht. Trotz großer Unterschiede in Stabilität und Hintergrundleitfähigkeit zeigten alle Verbindungen ferroelektrisches Verhalten bei Raumtemperatur, mit relativ großer Polarisation und kleinen Koerzitivfeldern. Insbesondere zeigten die ferroelektrischen Eigenschaften eines Materials eine starke Abhängigkeit von der Umgebungsfeuchtigkeit, während ein anderes eine starke Kopplung zwischen Hintergrundleitfähigkeit und ferroelektrischem Schalten aufwies. Von den verbleibenden zwei Verbindungen erwies sich eine als instabil bei Raumtemperatur, während die andere mehrere Polymorphe zeigte, was die Reproduzierbarkeit erschwert und ihr praktisches Potenzial einschränkt.

Aufgrund seiner einzigartigen Feuchtigkeitsabhängigkeit wurde das erste Material detailliert mit frequenz-, temperatur- und feuchtigkeitsabhängigen Messungen des ferroelektrischen Schaltens untersucht. Wir beobachteten eine ausgeprägte Abhängigkeit der ferroelektrischen Eigenschaften von der Schaltfrequenz, der Temperatur und, bemerkenswerterweise, der Umgebungsfeuchtigkeit. Interessanterweise scheint das ferroelektrische Verhalten an die komplexe elektrische Leitfähigkeit gekoppelt zu sein. Wir interpretieren unsere Ergebnisse im Sinne eines mehrstufigen Polarisationsumkehrungsmechanismus, der eine Kombination aus Protonentransfer und Molekülrotationen beinhaltet, wobei ersterer vermutlich auch für den beobachteten langreichweitigen Ladungstransport verantwortlich ist. Diese Eigenschaften könnten Anwendung in neuen Klassen von regelbaren oder auf die Umgebung reagierenden „Smart-Materials“ finden. Insgesamt stellt diese Arbeit nicht nur neue funktionale organische Materialien vor, sondern bestätigt auch, dass „Data-Mining“-Strategien ein mächtiges Paradigma zur Beschleunigung ihrer Entdeckung darstellen und bildet eine Basis für die Verbesserung dieser Analysen.

Table of Contents

Author's publications

Publications used in this thesis

The following publications form the basis of this thesis.

[1] M. Litterst, A. A. Butkevich, and M. Kemerink. "Inconclusive proof of ferroelectricity in peptide-VDF ribbons," *Nature*, vol. 644, no. 8075, pp. E1–E3, 2025. doi: 10.1038/s41586-025-09314-2.

- **Status:** Published (Aug 2025).
- **Author's contributions:** I performed all experiments and data evaluations. I wrote the initial manuscript draft, which was subsequently refined by all co-authors.

[2] M. Litterst, M. Balagopalan, R. Jannasch, E. D. Sødahl, S. Seyedraoufi, C. H. Gørbitz, K. Berland, O. Nilsen, and M. Kemerink. "Experimentally confirmed ferroelectricity in organic compounds identified by database mining."

- **Status:** Submitted to Physical Chemistry Chemical Physics (Aug 2025); currently under revision.
- **Author's contributions:** I wrote the majority of the manuscript, excluding the sections on material selection, synthesis, and XRD, which were written by M. Balagopalan. I conducted the device fabrication and electrical measurements (partially in collaboration with M. Balagopalan and R. Jannasch). I performed all electrical data evaluations.

[3] M. Litterst, R. Jannasch, M. Balagopalan, E. D. Sødahl, C. H. Gørbitz, O. Nilsen, K. Berland, and M. Kemerink. "Humidity-tunable organic ferroelectric with low coercive field."

- **Status:** In preparation; submission planned for early 2026.
- **Author's contributions:** I wrote the manuscript with the exception of the introduction, which was written by Prof. M. Kemerink. The experiments were conducted by R. Jannasch and myself under my supervision. I performed the final data evaluation for the publication.

Publications not used in this thesis

[4] H. Mager, M. Litterst, Sophia Klubertz, S.V. Haridas, O. Shyshov, M. von Delius, M. Kemerink., “A supramolecular ferroelectric with two sublattices and polarization dependent conductivity,” https://arxiv.org/abs/2507.11309v1

- **Status:** Submitted to Advanced Science (July 2025); currently under revision.
- **Author’s contributions:** I started the investigation of this material together with H. Mager. Following the initial proof of ferroelectricity, further investigation was completed by H. Mager to allow me to focus on the research presented in this thesis.

Conference and workshop contributions

1. "Transversal piezo-force-microscopy with the use of interdigitated electrodes." *Poster presentation*, DPG-Frühjahrstagung der Sektion Kondensierte Materie, Dresden, Germany (March 2023).
2. "BTA: The story of a prototypical ferroelectric liquid crystal." *Oral presentation*, Advancing Functional Molecular Matter Workshop, Oslo, Norway (January 2024).
3. "Systematic search for novel organic ferroelectric materials." *Oral presentation*, DPG-Frühjahrstagung der Sektion Kondensierte Materie, Berlin, Germany (March 2024).

I. Introduction

A. Organic electronics

Despite a current media focus on topics like international conflict and economic problems, different environmental problems such as extreme weather events, critical changes to Earth systems and biodiversity loss and ecosystem collapse are perceived as the biggest global risks over the next decade [5]. The root causes lie in the continued emissions of anthropogenic greenhouse gases like carbon dioxide and methane, the destruction of ecosystems and pollution of air, land and sea. Consequently, quick action is needed to reduce the use of fossil fuels for transport, heating, electricity generation and industrial processes. This requires electrifying these processes with renewable energies or finding other green alternatives where this is not possible, reducing land use in agriculture and resource generation, and reducing pollution through using less resources, efficient recycling and the use of less polluting materials. [6]

All of this can only be achieved by a myriad of different approaches, of which the widespread use of organic electronics might play a small part in. They offer cheap and flexible materials that can be produced with little energy [7], [8], do not require mined minerals and usually leave no toxic end-products. Additionally, they can enable new applications not possible with inorganic electronics.

The big breakthrough of organic electronics came with the wide adoption of organic light emitting diodes (OLEDs) which now dominate the display market [9] due to their energy efficiency and superior image quality. Additionally, they allow for flexible and curved displays [10].

Organic solar cells (OSCs) have the greatest potential for environmental impact due to their potential for widespread solar energy generation. They are cheap to produce as they are mostly produced from abundant materials[1] [11] via solution processing and do not require high manufacturing temperatures which also renders their production less energy-intensive [12]. Their current efficiency record is 19.2 % [13] which is close to the approximately 20 % that commercial silicon solar cells have. Consequently, the cost per power is potentially lower for organic solar cells, which means that if there is enough area available, it might be more economical to use organic solar cells. Unfortunately, commercial products have not achieved this potential yet and it remains to be seen whether the cost advantages can offset the costs for more space and additionally needed electronics. Perovskite solar cells, which have similar working principles as OSCs but use lead-based perovskite crystals as active material are now entering commercial use in tandem solar cells to increase the efficiency of the silicon-based solar cell [14]. Consequently, OSCs are currently limited to use-cases where their flexibility

[1] The indium for the transparent electrode (mostly indium tin oxide) is the major issues here, but materials like fluorine-doped tin oxide can help in solving this issue.

[15] or transparency [16] is needed, for example in wearable devices or for implementation in windows.

Organic electronics are also used for flexible conductors [17] and transistors [18] for electric circuits, wearables, small-scale thermoelectric energy generators [19] and a wide range of sensing applications [20], [21]. They also offer great potential to replace the currently widely used, mostly toxic, ferro- and piezoelectric materials with non-toxic alternatives which expand the area of use for example to energy generators for flexible wearable devices. This work focuses on finding new materials that could play such a role, as well as understanding their underlying processes to support their further development. This introduction will first provide a more detailed overview of the applications of inorganic and organic ferroelectrics, followed by a brief outline of the research conducted in this thesis.

B. Ferroelectrics

Ferroelectric materials can maintain an electric polarization without the application of an electric field. This polarization can be inverted via a sufficiently large electric field. Analogous to hard disk drives which use ferromagnetic materials, the two stable electric polarization states of a ferroelectric can be used to store information. They can offer a fast writing frequency in the MHz range with low power usage and very high reliability even after many writing cycles and elevated temperatures even in the event of a power loss [22], [23]. The high stability makes ferroelectric random access memories (FeRAMs) ideal for applications in many critical systems like event data recorders and data logging in automobiles and industrial systems [24] and the low power usage makes them ideal to store data in implants where battery power is scarce [25]. They have however two critical weaknesses: The readout of the saved data usually deletes the data, requiring its rewriting [26] and the current memory sizes are currently in the KB to MB range [27]. Even though implementing different device architectures like ferroelectric field effect transistors [26] or using materials with a polarization conductivity [4] can lead to a non-destructive read-out and further miniaturization is possible [26], FeRAMs will probably remain restricted to the use-cases where their above-mentioned advantages are crucial (which is still a hundred million dollar market [27]) and are unlikely to find widespread application in consumer electronics.

Ferroelectric materials are also pyro- and piezoelectric. This means that changes in temperature (pyroelectricity) and mechanical deformation (piezoelectricity) alter the material's polarization, generating charge and voltage at its surface. Conversely, applying a voltage leads to a deformation of the material (converse piezoelectric effect). As ferroelectric materials usually show the strongest pyro- and piezoelectric response, they are usually used for these applications.

Pyroelectricity can be used to generate electricity from waste heat [28], [29]. However, as only the temperature variation (which is less common than a temperature gradient) creates an output, the application is limited. Pyroelectric materials are however widely used for measurement of temperature [30] as well as infrared [31] and ultraviolet [32] radiation, for

example, in flame detectors [33], gas sensing [34] and industrial laser power measurements [35].

The most important applications of ferroelectric materials, however, are based on their piezoelectric properties as the coupling of deformation and electricity is exploited in actuators, sensors and energy generators. Piezoelectric actuators show high-frequency response, exceptional robustness, and high resolution at the expense of a small movement range [36], [37]. Consequently, they are the most efficient ultrasound generators [38], can build the fastest and most precise fuel injectors [39] and offer the (sub-) atomic movement precision for scanning microscopes [40]. Piezoelectric materials are also capable of converting small movements (like vibrations) to electricity [41] making them ideal for shock [42], force [43] and (ultra-)sound detectors [44]. The actuating and sensing properties of piezoelectric materials are also used together for example in quartz resonators[2] (for example in quartz watches) where the resonator is electrically excited and the voltage due to the vibration is used to measure the frequency. Piezoelectric materials are also efficient small-scale energy generators [45] which are used for self-powered sensors [41] or battery- and wireless switches [46] and igniters [47]. These applications can be expanded to recharge implants, reducing the need for surgical battery replacement [48] and fabrics to power wearable devices or recharge electronic devices [49]. Other concepts have also been explored, such as harvesting energy from pedestrian footfalls [50]. However, the power output remains minimal, making their widespread adoption unlikely.

Out of all the addressed applications, piezoelectrics are the by far the most commercially important with an estimated market of 31 billion $ [51] compared to 1.8 billion $ for pyroelectrics [52] and 450 million $ for ferroelectric RAMs [53]. All commercially relevant materials are based on inorganic materials, as they are well understood, efficient and reliable. However, they are also stiff, brittle and usually based on toxic heavy metals. This limits their application range and introduces health and environmental problems. Consequently, there is a critical need for new materials that are flexible and non-toxic—a challenge perfectly suited to the strengths of organic electronics.

C. Organic ferroelectrics

Organic ferroelectrics are organic polymers, liquid crystals, small molecules or co-crystals which exhibit ferroelectricity. Similar to inorganic ferroelectrics, they also show pyro- and piezoelectricity which means that they are at least in principle capable of performing all the tasks for which inorganic ferroelectrics are currently used. However, they might not only be capable of replacing the inorganic ferroelectrics where they are currently used but can also extending their range of application. As already introduced above, organic materials are usually flexible, easy to produce and require little to no mined minerals. Their piezoelectric coefficients are however often smaller, leading to weaker effects. Shifting to organic

[2] This is one of the few cases where the non-ferroelectric material quartz is used as it shows small losses and good stability [210].

ferroelectrics will in many cases lead to easier-to-produce devices with less heavy metal pollution. Unfortunately, for many applications this might not be enough to offset the often inferior performance of organic ferroelectrics. This is especially the case for actuators where stiffness is often essential [54], [55]. The importance of these factors will probably be more affected by public perception as well as environmental- and health policy than material science.

In contrast, for (ultra-) sound generators it is often better to have a more flexible active material. The reason is that sound waves are reflected when passing the interface of materials with different stiffness and density. This phenomenon also generates the echo when shouting at a cliff. Crucially, organic ferroelectric materials are mechanically much closer to water or tissue [56], where the sound wave is usually transmitted into, which results in a much better transmission of the wave [57]. The same phenomenon also makes them more efficient for the use in microphones [58]. Contrary to prior believe, the mechanical compliance also has only small effects on the efficiency of a piezoelectric energy harvester, making organic ferroelectrics a viable choice of material [45] and rotational freedom can boost their efficiency [59]. The usage of a flexible and non-toxic material is also strongly advantageous, if not necessary, when building an energy generator for use in implants or clothing.

For these materials, polyvinylidene fluoride (PVDF) is usually considered the most promising material due to its excellent piezoelectric properties combined with its mechanical and thermal stability [60]. This stability is however not only advantageous as it prevents degradation of the material and thus accumulation in humans and the environment. While PVDF is generally considered not to be a health-risk, the same is not true for many other Per- and polyfluoroalkyl substances (PFAS) and their precursors [61]. For this reason the European Union is planning to ban the use of some or all PFAS substances [62]. This legislation will likely leave room for the future use of PVDF. Furthermore, it seems questionable to ban a potentially harmful chemical while simultaneously allowing the continued use of toxic, heavy-metal-based materials. Nevertheless, this development indicates that PVDF might not be the ideal foundation upon which the future of (organic) ferroelectrics should be built.

While there are many other organic ferroelectrics, they often have problems with reliability and show inferior performance. As they are so far much less investigated than inorganic ferroelectrics and, meanwhile, show much more diverse behaviors, their potential is far from exhausted. An ideal organic ferroelectric should have a high remnant polarization and strong piezoelectric coefficient at ambient conditions for strong performance and be stable enough to maintain these properties for years. A transducer used, for example, in microscopes or valves requires rigidity, whereas an ultrasound generator or a wearable energy harvester benefits from softness. If the material is to be ferroelectrically switched, for example in a memory device, the voltage for switching should ideally be around 1-2 V [63]. Depending on the feature size, this can require materials across the entire range of coercive fields (100 V/µm corresponds to 10-20 nm, while 0.2 V/µm corresponds to 5-10 µm features). For the materials to improve on the drawbacks of inorganic ferroelectrics they should be biocompatible and

their production should require little energy, (almost) no critical resources to produce and not produce any toxic waste.

One of the overarching goals of this work was to establish a reliable and easily applicable method to identify new and interesting organic ferroelectrics. This challenge consists of two parts: The theoretical identification of candidate materials and the subsequent experimental examination of these materials.

While data-driven mining approaches have already lead to successful innovations for organic solar cell- [64] and battery materials[65], [66], such a method has not been widely adapted for ferroelectrics. This project builds upon the only two available database mining studies which predicted 54 globular [67] and 12 proton-transfer [68] ferroelectric candidate materials. Out of these materials, we selected four easily-accessible materials which were either commercially available or could be produced by recrystallization of two commercially available compounds.

My main contribution to this was the development and application of a robust and practical experimental procedure to examine these materials: After building devices of the material with interdigitated electrodes, the material is mainly investigated with dielectric spectroscopy, the double wave method (DWM) for ferroelectric hysteresis loops, and CV loops. Dielectric spectroscopy (possibly complemented by differential scanning calorimetry) is used to identify characteristic temperatures that might indicate phase transitions which, in turn, indicates where the relevant temperature ranges for further measurements might sit. The DWM measurement gives the most information about the materials' (ferro-)electric properties and CV measurements are a good way to validate the ferroelectric measurements as they produce the clearest results. These measurements are usually combined with other measurements like optical and atomic force microscopy and X-ray diffraction to control the quality of the material and devices.

These results were firstly used to determine whether these materials are indeed ferroelectric and to judge their usefulness for possible applications. Additionally, those experiments revealed new and interesting phenomena that were investigated in more detail to gain more insights into the switching process of proton-transfer ferroelectrics. Finally, these results help close the discovery loop between theoretical prediction and experimental reality. While the investigated sample set is small, it provides data that highlights critical blind spots in current computational screening methods.

The successful work and experience allowed me to write a Nature Matters Arising article [1] as well as two research papers [2], [3] (one currently under review, the other one close to submission).

II. Properties of ferroelectrics

When any material is exposed to an electric field $\vec{E}$, many phenomena can occur. The two most common phenomena are the appearance of a polarization $\vec{P} = \chi * \vec{E}$ where the proportionality constant χ is the material's susceptibility [69] as depicted in Fig. 1(a) and of an electric current with density $\vec{j}$ following Ohm's law $\vec{j} = \sigma\vec{E}$ and sigma being the conductivity. [70] Conductivity in organic materials is briefly discussed in chapter II.F. While the polarization scales linearly with electric field for dielectric materials (where the polarization occurs mainly on an atomic level), the same is not true for paraelectric materials. These are materials with free dipoles which become aligned by an electric field. Such a polarization is usually much stronger but saturates once the dipoles are oriented as shown in Fig. 1(a). If the dipoles of such a material have sufficiently strong dipole-dipole interactions, these interactions can stabilize the polarization, leading to ferroelectricity as shown in Fig. 1(a).

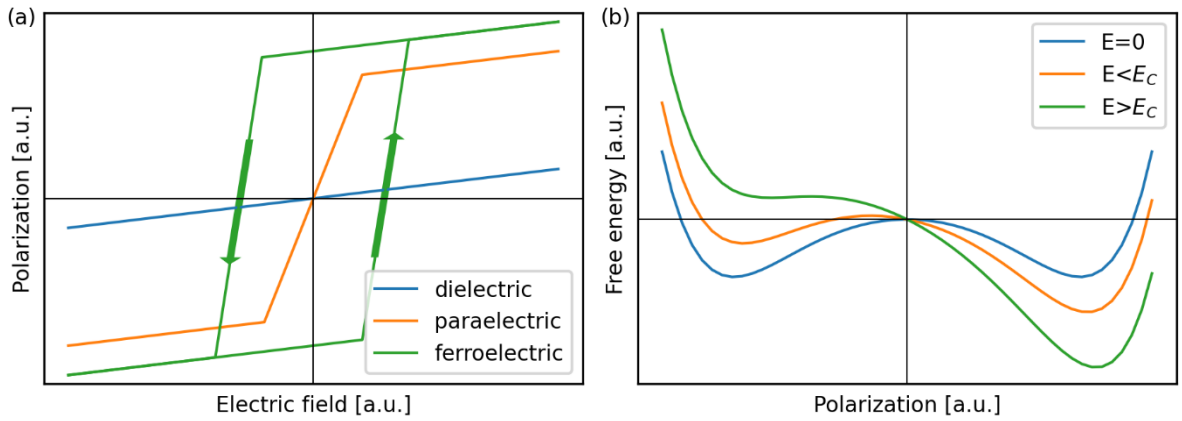

Fig. 1 (a) PE-curves of a dielectric (blue), paraelectric (orange) and ferroelectric (green) material, (b) Free energy from Landau-Devonshire-theory of the ferroelectric phase for $E = 0$ (blue), $E < E_C$ (orange) and $E > E_C$ (green)

A. Landau theory

A theoretical description of ferroelectricity has been provided by Devonshire [71] based on Landau's theory of phase transitions [72] and is therefore called Landau-Devonshire theory. The free energy can be described by the order parameter, the polarization P, and the electric field E. There are three material coefficients a, b, and c of which b and c are considered independent of temperature, while a depends on the temperature. Its value can be linearly approximated close to the critical temperature T_0[3]: $a = a_0(T - T_0)$ [73]. This results in an expression of the free energy:

$$F_P = \frac{1}{2}a_0(T - T_0)P^2 + \frac{1}{4}bP^4 + \frac{1}{6}cP^6 - EP \qquad \text{Eq. 1}$$

This results in the typical double-well potential of a ferroelectric as depicted in Fig. 1(b). If there is no electric field, the free energy is symmetric, leading to two stable polarization states of equal free energy. Their polarization is called the remnant polarization P_r. If there is a small electric field applied, the curve becomes asymmetric (orange in Fig. 1(b)) with one global

[3] The critical temperature T_0 lies close-to, but not at the Curie-temperature T_C

minimum and another metastable polarization state. Upon further increase of the electric field, the metastable state ceases to be an energy minimum (green curve), which leads to the global minimum being the only stable state. The field at which this occurs is called the coercive field E_C.

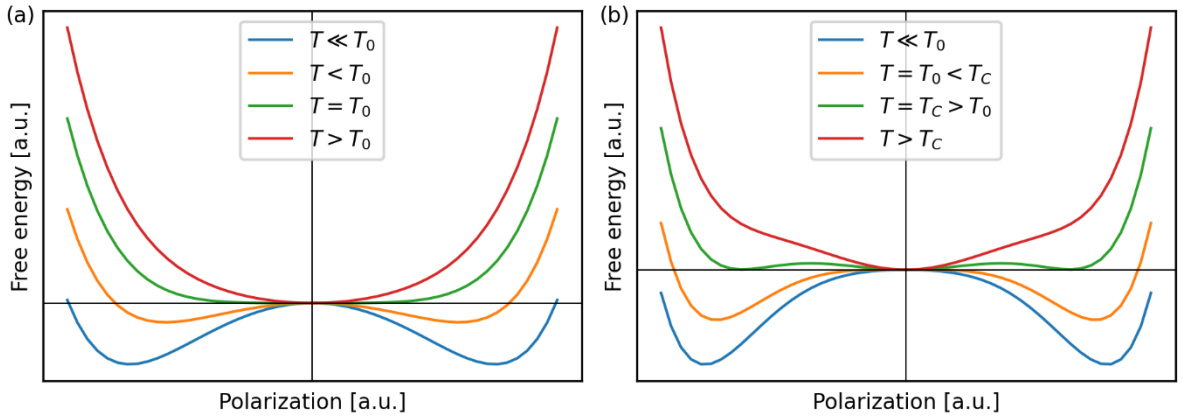

Fig. 2(a): Free energy for different temperatures with b>0, leading to a second order phase transition, (b): temperature dependent-free energy for b<0, leading to a first order phase transition

Increasing the temperature while remaining in the ferroelectric state (shift from blue to orange in Fig. 2a/b) decreases the remnant polarization as well as the barrier between the two minima, reducing the coercive field.

When further increasing the temperature, it becomes relevant whether b is smaller or greater than 0: If it is bigger, there is a second-order (also called continuous) phase transition, as depicted in Fig. 2(a). As the name suggests, it is characterized by the remnant polarization continuously decreasing to 0 at the critical temperature (plotted in [73]). If b<0, the remnant polarization (the minimum in Fig. 2(b)) slowly decreases until the Curie-temperature T_C is reached, at which the minimum position jumps from the ferroelectric polarization states ($P=P_r$) to P=0. This is called a first-order or discontinuous phase transition. It must, however, be noted, that the "ferroelectric" polarization states can be metastable even above T_C, which is called temperature hysteresis.

By minimizing the free energy with respect to polarization ($\frac{dF_P}{dP} = 0$), one can obtain the electric field as a function of polarization:

$$E = a_0(T - T_0)P + bP^3 + cP^5 \qquad \textit{Eq. 2}$$

In the paraelectric phase, the minimum is at P=0. Calculating the susceptibility χ yields:

$$\chi = \frac{dP(0)}{dE} = \frac{1}{a_0(T - T_0)} \qquad \textit{Eq. 3}$$

This is known as the Curie-Weiss law. For b>0 it is also possible to make the same calculation in the ferroelectric phase by only considering the first two terms of the expansion at E=0. With the remnant polarization of

$$P_r = \pm\sqrt{\frac{a_0}{b}(T_0 - T)} \qquad \text{Eq. 4}$$

It is possible to evaluate the derivative of Eq. 2 at P=P_r:

$$\chi = \frac{dP(P_r)}{dE} = \frac{1}{a_0(T - T_0) + 3a_0(T_0 - T)} = \frac{1}{2a_0(T_0 - T)} \qquad \text{Eq. 5}$$

This means that in the ferroelectric phase, the temperature dependent susceptibility has twice the slope as in the paraelectric phase. While the typical Curie-Weiß behavior (Eq. 3) is observed for many materials [74], [75], there are much fewer cases where double the slope in the ferroelectric phase is observed. One such example is found in some samples of BTA [76].

B. Ferroelectric hysteresis

All the above-mentioned observations lead us to the definition of a ferroelectric: *A ferroelectric is a material with two stable (electric) polarization states, between which can be switched by the application of a sufficiently large electric field.* The hysteresis is shown in the Polarization versus electric field (PE) curve. An idealized version was already displayed in Fig. 1(a), an experimentally measured curve is now shown in Fig. 3(a). The key characteristic of a true ferroelectric hysteresis curve is that it saturates once most, or all, dipoles have switched. An open PE-loop can also arise from a leaky dielectric and does not by itself prove ferroelectricity, which was even demonstrated with a banana [77]. A detailed analysis of how a ferroelectric can correctly identified is provided in chapter II.H. The PE curve of a ferroelectric shows the ferroelectric key parameters, which are also displayed in Fig. 3(a).

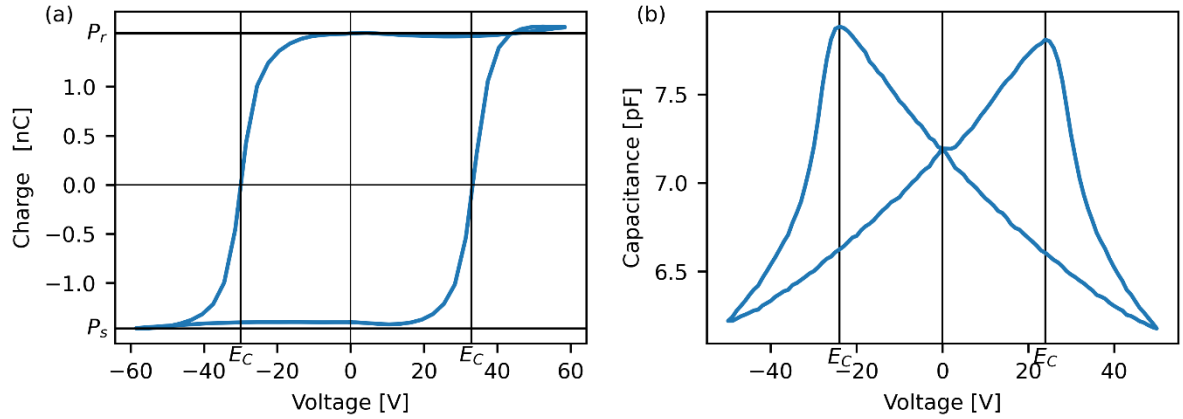

Fig. 3(a): Hysteresis curve of poly (vinylidene fluoride-trifluoroethylene) [P(VDF-TrFE)], (b): its CV-loop. As voltage, charge and capacitance are the measured values, they are displayed here. They can be converted to electric field, polarization and permittivity with conversion factors which depend on the sample geometry and is not always trivial. This is further addressed in chapter III.A.2

The coercive field E_C is the field, where the polarization is inverted. In a real sample, polarization inversion does not occur instantaneously at one specific voltage, but in a voltage region[4]. For this reason, the coercive field is defined as the field where half the dipoles have switched (P=0). The coercive field is not a fixed material parameter but depends on experimental conditions like the temperature (as demonstrated by Landau-Devonshire-theory above) and the measurement frequency, where higher temperatures and lower frequencies

[4] This region is characterized by the hysterons in the Preisach distribution [122], [123].

decrease the coercive field [78], [79]. Models, which describe these dependencies, are presented in chapter II.E.

The polarization at zero field is called the remnant polarization P_r. It describes the dipole density of the stable state and should therefore be determined by the crystal structure. Consequently, it decreases with increasing temperature (as seen from Landau-Devonshire-theory), but should not depend on other parameters like the measurement frequency [78], [79]. It is also possible to determine the saturation polarization P_s, which is the polarization at maximum field. It is however rarely used, since it also depends on the maximum voltage and also strongly on the evaluation method, as some methods (like the double wave method described in chapter III.C.1) compensate for non-ferroelectric contributions while others do not.

It is also possible to measure the permittivity (or capacitance) of a ferroelectric at different electric fields. This is a relevant measurement as the permittivity describes how many mobile dipoles are present in the material. One would expect that there should be more mobile dipoles at the coercive field, where they are less stabilized by the surrounding dipoles as some of them are already switched, resulting in a higher permittivity. This is also what is observed in the real measurement (Fig. 3(b)), which displays the typical butterfly-shape with peaks at the coercive field. As these measurements are usually slower, the observed coercive field is typically lower than for the PE-curve (Fig. 3(a)) [80].

A more detailed analysis shows that only a fraction of the dipoles is actually measured in a CV-measurement. The reason is that most dipoles remain in a stable position after being switched once and only a small portion can be switched back. This fraction is called the reversible polarization. For this reason, integrating the CV-loop does not yield the PE-loop but a much smaller and thinner curve. CV-loops are only rarely shown in literature. Possible explanations for this are that it contains less information than the PE-loop (absolute polarization values are missing) and that for some materials the reversible polarization can be very small. This can for example be seen for trialkylbenzene-1,3,5-tricarboxamide (BTA) [81], where the relative changes are much smaller than for P(VDF-TrFE) (Fig. 3(b)), but the general butterfly shape is still visible. It should also be noted that while there are countless examples of questionable claims of ferroelectricity based on open, but non-saturating PE-loops, there is no questionable claim based on a CV-loop known to the author. The reason for this is that a leaky dielectric can create an open, non-saturating PE-loop that might, at first glance, look like that of a ferroelectric. In contrast, the CV-loop of the same material would be completely flat, leaving no ambiguity. For this reason, the CV-loop should be used much more frequently to support claims of ferroelectricity.

C. Piezo- and pyroelectricity

As discussed in the previous two chapters, the remnant polarization of a ferroelectric is temperature-dependent. As having the remnant polarization is the thermodynamically preferred state, heating or cooling the sample will change the polarization, resulting in voltage generation due to a change in screening charges. This behavior is called pyroelectricity and occurs in all ferroelectrics, but also other materials that have a non-zero polarization, which is not always reversible, as electric breakdown can occur below the coercive field. For this reason, ferroelectric materials are a subclass of pyroelectrics. As all pyroelectrics require a net polarization, they cannot have a center of inversion symmetry and need a polar axis. This means that pyroelectrics can only have 10 out of the 32 point groups[82].

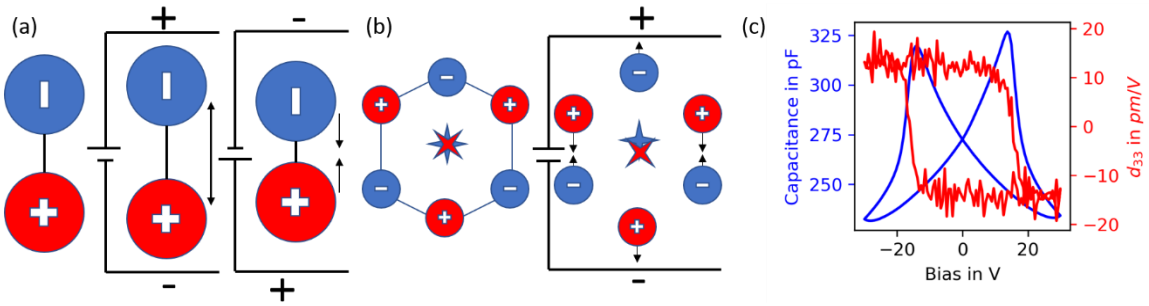

Fig. 4(a): Converse piezo effect of a dipole, standing for a ferroelectric material, (b): converse-piezo effect of a non-ferroelectric material with stars marking the center of pos. and neg. charge, (c) CV and piezo-measurement of P(VDF-TrFE)

When applying an electric field to a material with a permanent polarization (depicted by a dipole in Fig. 4 (a)), the material either expands or contracts, depending on the orientation of the field with respect to the polarization, as shown in Fig. 4 (a). This is the converse piezoelectric effect, which is depicted here for ease of illustration. It is complementary to the piezoelectric effect, which describes that compression or expansion of a piezoelectric material generates a voltage and was first discovered by the Curie brothers in 1880 [83]. Interestingly, some organic materials (like PVDF and BTA) show a negative piezoelectric coefficient [81], [84]. This means that, for these materials, compression of the material increases the polarization. There are several models to explain this behavior, most of them involving the interplay between crystalline and amorphous regions [85].

A material does not need a permanent polarization to exhibit piezoelectricity. It only requires a crystal structure where compression/expansion separates the centers of charge, or conversely, where separating the centers of charge induces contraction/expansion [86]. One such example is shown in Fig. 4 (b), and the most prominent example of piezoelectric (but not pyro- or ferroelectric) material is quartz. While these materials do not have the same restriction regarding their point groups, they are still not allowed to have a center of inversion symmetry as stress induces a polarization in one direction, which would not be possible with inversion symmetry. Out of the 21 point groups without inversion symmetry, 20 can be piezoelectric [86]. Interestingly, all piezoelectric materials exhibit a version of secondary pyroelectricity: When heating (cooling) the material, it expands (contracts) due to thermal expansion. This creates stress which, due to piezoelectricity, induces a voltage. For this reason,

materials that, according to the definition here, are not pyroelectric are occasionally called pyroelectric, even though the underlying physical effect is piezoelectricity [87].

The piezoelectric coefficient of non-ferroelectric materials is usually constant at a given temperature[5]. For ferroelectrics it however depends on their polarization state, which can be inverted with an electric field. This is shown in Fig. 4(c) where the capacitance and piezoelectric coefficient are measured as a function of applied bias. As discussed before, the capacitance peaks at the coercive field, which is also where the piezoelectric coefficient is inverted.

D. Classification of ferroelectric materials

There are several ways to classify ferroelectric materials, depending on the distinctions being made. Here, a distinction has already been made between organic and inorganic ferroelectrics, because it is a good indicator of how they are synthesized and their thermal stability. There is, however, a much more common classification according to how ferroelectric switching occurs and what happens at the ferro-to-paraelectric phase transition. There are displacive ferroelectrics, order-disorder ferroelectrics, which are named according to their phase transition and involving permanent dipole reorientation as a switching mechanism and proton-transfer ferroelectrics [88]. This classification is very useful as the different classes have different ranges of coercive field and remnant polarization, which are the key parameters of ferroelectrics. Parts of this classification are based on the introduction to my paper which provides an overview over several materials [2].

1. Displacive ferroelectrics

Most inorganic ferroelectrics have an ordered lattice in which the change in polarization arises from a shift in the position of an ion or a charged molecule [89]. Organic or hybrid ferroelectrics can have similar switching mechanisms with the displacement of an ion [90], [91] or a charged molecule in a mixed stack, known as charge-transfer ferroelectrics [92]. The paraelectric phase of such a material is shown in Fig. 5(a), with equal spacing between the ionic molecules. The ferroelectric state (Fig. 5(b)) is characterized by a pairing of two molecules, leading to a breaking of symmetry and a change of polarization. This behavior is similar to the Peierls distortion, in 1D metals [93], but with a different (here: electrostatic) attractive force. Both rely on the nesting effect which only appears in systems governed by 1D interactions at low temperatures [94]. The paraelectric state is labeled ΔP=0 as, for periodic systems, only changes in polarization are clearly defined [95]. This is, however, not a problem, as it is also only possible to measure changes in polarization. For all practical purposes it is therefore sufficient to define the paraelectric state as P=0 and the remnant polarization as $\pm P_r$.

The most important displacive ferroelectrics are of perovskite type. They have an $A^{2+}B^{4+}O_3^{2-}$ structure with two positive and three negative (mostly O^{2-}) charged ions. Their symmetric and

[5] It is strongly direction-dependent, which is defined by the piezoelectric coefficient tensor. [163]

paraelectric arrangement is shown in Fig. 5(c). When cooling below the Curie-temperature, the positive ions shift in one direction and the negative in the other, thus losing the cubic shape and introducing a polarization. The commercially most relevant ferroelectrics (Barium titanate, lead zirconate titanate and lead titanate [96]) all belong to this class.

Such displacive ferroelectrics tend to have comparatively high remnant polarization values and relatively low coercive fields, e.g. P_r ≈ 15 µC/cm^2 and E_c≈ 2 V/µm for PZT [89], which makes them suitable for many applications as the high remnant polarization also leads to strong piezoelectric coefficients close to 500 pm/V [97].

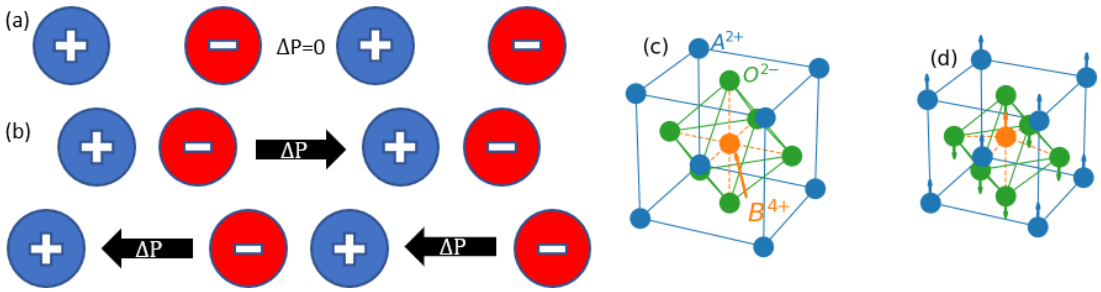

Fig. 5: (a) Symmetric (paraelectric) phase of a mixed stack charge transfer ferroelectric; (b) its two ferroelectric polarization states; (c) paraelectric perovskite phase; (d) The distorted, ferroelectric phase of a perovskite [215].

2. Order-disorder ferroelectrics

Order-disorder ferroelectrics are mostly organic materials which have permanent dipoles. These dipoles are disordered above the Curie temperature and ordered in the low-temperature ferroelectric phase. The most prominent order-disorder ferroelectric is the polymer polyvinylidene fluoride (PVDF) [98]. Its ferroelectric β-phase is shown in Fig. 6(a)[6]. However, it usually crystallizes in the non-ferroelectric α-phase and extensive processing, usually including combinations of high temperatures, high biases and stretching [99], [100], is required to achieve the desired phase. By introducing fractions of trifluoroethylene (TrFE), heating the material for 2 hours above the Curie temperature is sufficient to achieve the desired phase transformation (this procedure was also applied to the sample shown in Fig. 3). This, however, comes at the expense of a lower polarization. The polarization can then be inverted by an electric field, which rotates the whole polymer chain [101]. Even though PVDF is the most studied organic ferroelectric, the details of switching [101], [102], the reason for its negative piezoelectric coefficient[85], its structural evolution under poling [103] and the role of (un)intentional structural defects [104], [105] are still being investigated.

Another prominent example is the supramolecular polymeric liquid crystal trialkylbenzene-1,3,5-tricarboxamide (BTA). One molecule consists of a central benzene core (orange in Fig. 6(b)) which enables π-π stacking of the molecules, three amide groups (green) which provide the dipole and form hydrogen bonds with the neighboring molecules and long unipolar side-chains which improve solubility in organic solvents. These molecules form a supramolecular polymer as depicted in Fig. 6(c). Crucially, in this column the dipoles form a triple helix, which

[6] The β-phase is the most relevant but not the only ferroelectric phase. There is also promising work on the δ-phase [211] and γ-phase [212].

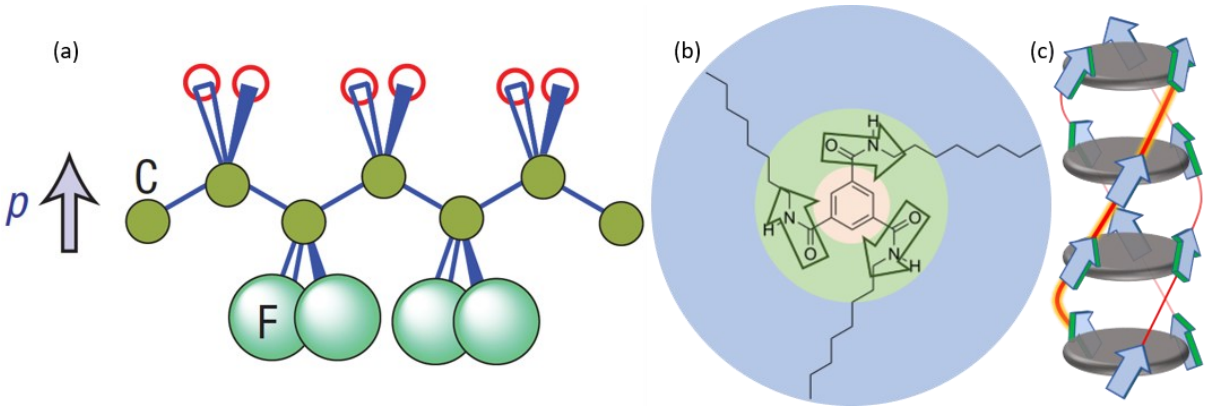

Fig. 6 (a): β-phase of P(VDF), reproduced with permission from [88]*; (b): molecular structure of BTA; (c) Supramolecular column of BTA, with grey discs symbolizing the benzene core and the arrows the dipole of the amide group.*

leads to a macrodipole along the column. Application of an electric field leads to an inversion of the dipole moment and therefore ferroelectricity [76]. While the molecule depicted here is the basis, it is possible to change the side chains [106], [107], the amide group [108] or the core [109], [110] to alter its key properties. Other order-disorder ferroelectrics include globular molecules, where switching arises from the rotation of the entire molecule [111].

This class of ferroelectric materials generally has lower remnant polarizations, limited by the dipole moment of the molecule, and higher coercive fields. For example, P(VDF) has a remnant polarization of P_r≈6µC/cm² and a coercive field of E_c≈100 V/µm [112], with a piezoelectric coefficient of d_{33}≈-40 pm/V [84]. Depending on the side chain, BTA exhibits a remnant polarization of P_r≈2-6 µC/cm², coercive fields of 25-40 V/µm [106] and d_{33}≈20 pm/V [81].

3. Proton transfer ferroelectrics

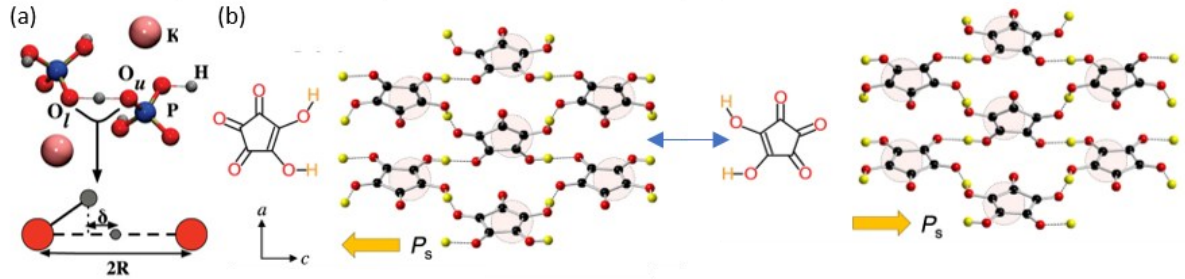

Fig. 7 (a): Molecular structure and depiction of the proton asymmetry of potassium dihydrogen phosphate (KDP), image reproduced with permission from[213]*; (b)molecular and crystal structure of croconic acid in both polarization states, reproduced from* [216]

The third class of ferroelectrics are proton transfer ferroelectrics (also called KDP-type [88]). In these materials, there is at least one proton in a hydrogen bond which can switch positions within the hydrogen bond (tautomerization). The most prominent example, after which the type is also named, is potassium dihydrogen phosphate (KDP) [113], which is depicted in **Fehler! Verweisquelle konnte nicht gefunden werden.**(a). As indicated, the proton is closer to one of the oxygen atoms. Application of an electric field can break the covalent bond with the oxygen atom and create a new one with the other oxygen atom, to which there was only a hydrogen bond before. This behavior is shown in Fig. 7(b) for the currently most investigated proton-transfer ferroelectric croconic acid. Proton-transfer ferroelectrics show characteristics

of displacive and order-disorder ferroelectrics, with switching due to displacement of a charged ion, but usually a phase transition to a disordered state [88][7].

These materials can exhibit very high remnant polarizations and small coercive fields. KDP has a moderate saturation polarization of P_s ≈5 µC/cm^2 and a very low coercive field of E_c ≈ 0.016 V/µm[114]. This state is, however, only stable up to 120 K, making it unusable for most applications. Croconic acid shows an impressive remnant polarization of P_r ≈ 30 µC/cm^2 and a very low coercive field of E_c ≈ 2 V/µm [115], which exceeds the values for PZT. As "proton"-transfer-rates depend on the mass of the hydrogen atom, deuterating the material (replacing the proton with deuterium) has effects on all parameters, with greatest influence on the coercive field [114], [116].

E. Switching and coercive field models

The coercive field is the field at which ferroelectric switching occurs. As previously discussed, this field is not one fixed value for a material but depends on many parameters, most importantly temperature and measurement frequency, but as shown in this work, other parameters like ambient humidity can be equally influential. This section will introduce the most commonly used models for ferroelectric switching and their predictions for the coercive field.

1. Intrinsic switching

From simple models (like Landau theory which is discussed in II.A) one would expect that there is one critical field, where the entire ferroelectric switches from one polarization state to the other, as sketched in Fig. 8(a). This is called intrinsic switching and the coercive field from Landau theory (of second order type) is $E_C = \frac{1}{3\sqrt{3}}\frac{P_S}{\epsilon_f \epsilon_0}$, while energetic considerations yield

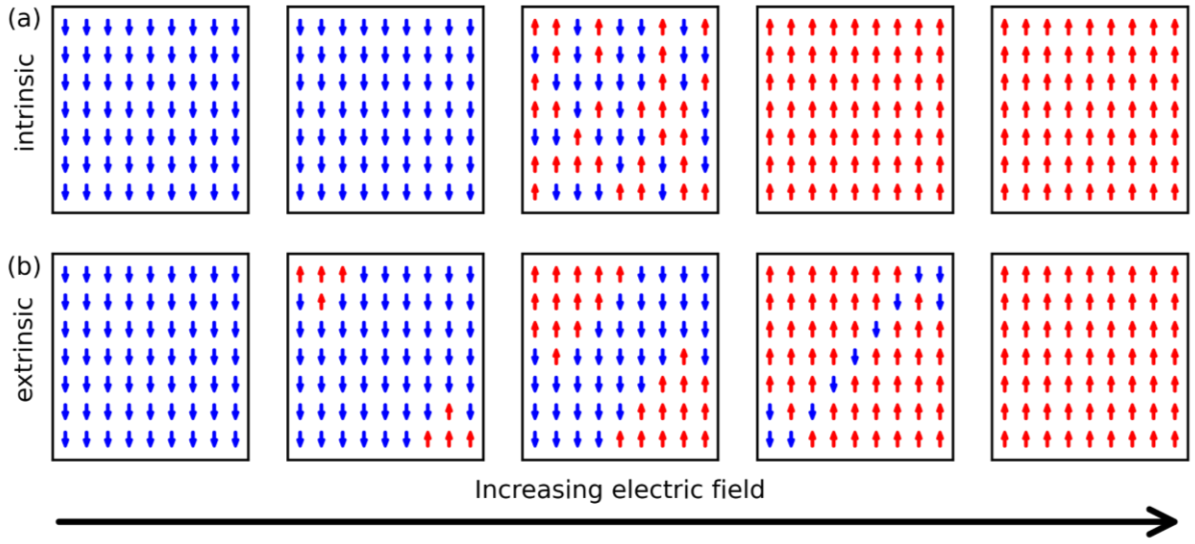

Fig. 8 (a) Sketch of intrinsic switching, happening almost instantaneously at the coercive field; (b) sketch of extrinsic switching, which occurs through nucleation and growth of domains

[7] There are indications that this is not the case for all materials, e.g. deuterated KDP[213]

$E_C = \frac{1}{2}\frac{P_s}{\epsilon_f \epsilon_0}$ [117]. P_s describes the saturation polarization, ϵ_0 is the vacuum permittivity and ϵ_f is the ferroelectric contribution to the materials permittivity. While intrinsic switching has been experimentally observed in systems carefully designed for this purpose, for example in Langmuir-Blodgett films of P(VDF-TrFE) [118], this type is not relevant for normal ferroelectrics. It is not only difficult to achieve, but the coercive fields are also much higher. For the homopolymer PVDF, intrinsic switching is achieved around 900V/µm, while extrinsic switching occurs below 100V/µm [119], [120]. For this reason, intrinsic switching is not further discussed.

All practical ferroelectrics rely on extrinsic switching instead. This means that switching starts with small nucleation sites, which are often introduced by defects [121], that subsequently grow until the entire material has switched. This is depicted in Fig. 8(b). The Preisach distribution [122] uses hysterons to describe the widening of the hysteresis curve, which can be related to the ferroelectric domains [123]. In this work, however, we only focused on the coercive field value, for which several models exist. The main difference between the models is how nucleation is modelled and whether the initial nucleation or the domain growth is considered the rate-limiting step.

2. Ishibashi-Orihara model

The first model for the coercive field relies on the classical Kolmogorov–Avrami–Ishibashi (KAI) theory [124], [125] which assumes that nucleation only happens at predetermined positions and consequently only the domain wall growth rate determines ferroelectric switching. In consequence, the coercive field only depends on the measurement frequency f, the dimensionality of growth d [8] and a factor α which depends on the waveform (α=5.7 for sinusoidal and triangular waveforms) [126]:

$$E_c \propto f^{d/\alpha} \qquad \textit{Eq. 6}$$

While this model describes many single-crystalline, inorganic ferroelectrics well, it usually fails to describe polycrystalline, disordered systems (which is often the case for organic ferroelectrics). [76], [127]

3. Du-Chen model

Du and Chen formulated a different model, where domain growth is fast compared to nucleation times, resulting in nucleation being the limiting factor for ferroelectric switching. First, the critical nucleus energy, which is the energy of the nucleus at the point where further domain growth of the nucleus is energetically favorable, is calculated. This energy depends on the electric field and needs to be supplied by thermal energy. When the resulting formation rate is combined with the threshold frequency f_0, at which nucleation is no longer rate-limiting, one obtains an expression for the coercive field [128]:

[8] "d=1 for planar walls parallel to each other, d=2 for cylindrical domains and d=3 for spherical domains" [126]

$$E_c \propto 1/\sqrt{k_B T ln(f_0/f)} \quad \text{Eq. 7}$$

k_B is the Boltzmann constant, T is the temperature and f is the measurement frequency. This dependence of the coercive field is more fitting for some polycrystalline films [76], [129]

4. Thermally assisted-nucleation limited switching

M. Vopsaroiu *et al.* introduced another model, which is usually called thermally assisted-nucleation limited switching (TA-NLS) even though this description would also apply to the Du-Chen model. However, this TA-NLS model is based on concepts from Tagantsev *et al.*[127] and Viehland and Chen [130] and starts from the intrinsic coercive field provided by the Landau theory and calculates the deviations due to nucleation[131]. Contrary to the Du-Chen model where nucleation happens intrinsically, it considers extrinsic nucleation centers like defects and grain boundaries to dominate the nucleation behavior. These centers significantly lower the energy barrier for nucleation compared to the ideal bulk lattice. Consequently, the switching kinetics are controlled by the probability of thermally activating a critical nucleus at these specific sites. The resulting frequency- and temperature-dependent coercive field is given by:

$$E_c \propto \frac{w_b}{P_s} - \frac{k_B T ln(\nu_0/(\ln(2)\, f))}{V^* P_s} \quad \text{Eq. 8}$$

In this equation, w_b is the switching energy barrier per volume, P_s is the saturation polarization, ν_0 is the attempt frequency (assumed to be the phonon frequency of the material), and V^* is the critical volume, above which the nucleus growth is energetically favorable.

It needs to be noted that even though both Du-Chen and TA-NLS are models for thermally activated nucleation limited switching, both models predict different behavior of the temperature- and frequency-dependent coercive field. The TA-NLS model predicts a linear dependence of E_c on temperature and a logarithmic dependence on the measurement frequency and is often considered to match the experimental results of organic and other polycrystalline ferroelectrics best [132], [133], which was also observed in this work.

F. Charge transport

The usually taught model for charge transport is based on electron bands in periodic crystal structures which are filled up to the Fermi level. If the Fermi energy lies within a band, it is partially filled and the material is a metal. Its conductivity is mainly influenced by the shape of the Fermi surface and scattering characteristics. If the Fermi energy lies between two bands, there are no free charge carriers at 0 K. If the energy of the filled (valence) and empty (conduction) bands are close enough together, thermal energy and doping atoms can create free charge carriers and the material becomes a semiconductor, where the electronic properties are mainly influenced by doping and temperature. If the band gap is too large for thermal excitation of charge carriers, the material is an insulator. [134] While this model works well for most metals and inorganic semiconductors like silicon, it fails to describe charge

transport in organics, where the mechanism is usually described by tunneling (hopping) between different localized sites.

1. Charge transport in organics

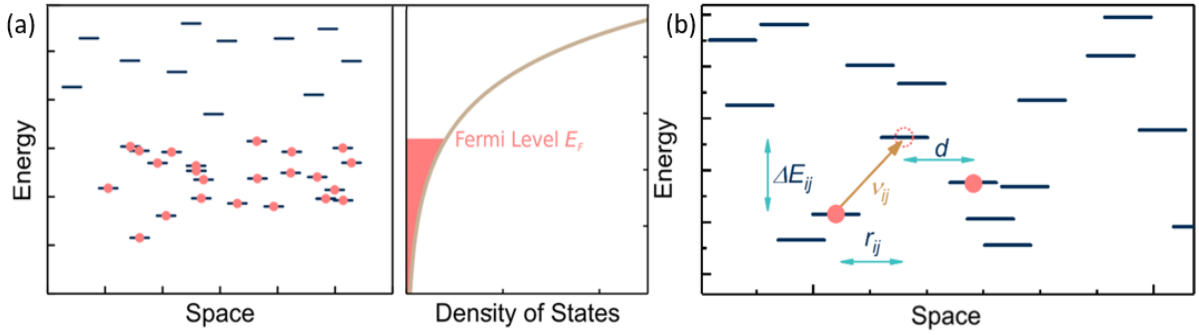

Fig. 9 (a) Depiction of sites in real- and energy space in a gaussian DOS along with the depiction and filling of the DOS; (b)sketch of a single hop. Image reproduced from [139]

Charge transport in organics is a vast topic, which is still extensively researched. In this chapter, the main concepts will be sketched, a thorough and complete overview is beyond the scope of this work and can be found in (review) articles [135]–[137], text book chapters [138] or PhD theses [139], on which this chapter is also based.

Organic electronics covers a wide variety of materials including (supramolecular) polymers, charge transfer crystals and small molecules. They all have in common that charge conduction is dominated by hops between different sites. A site can be anything between a single molecule and a conglomerate of molecules or a polymer chain where the charges can travel easily. These sites are spatially and energetically separated so that the wavefunctions on different sites do not significantly overlap. The sites have different energy levels due to different chain conformations, size and orientation. This energy distribution is typically modelled by a density of states (DOS), where Gaussian and exponential shapes are most commonly used. At 0 K, the sites are filled up to the Fermi level. A depiction of the (filled) sites in a Gaussian DOS can be seen in Fig. 9(a). At higher energies, there might also be a delocalized mobility edge, which is not shown for simplicity. Charge transport usually occurs through hopping (thermally activated tunneling) between different sites. Miller and Abrahams formulated a model [140] which neglects polaron effects (the effect of the charge on the surrounding lattice), in which case the transition rate (from i to j)ν_{ij} is given by:

$$\nu_{ij} = \nu_0 * \exp(-2\alpha r_{ij}) * \exp(-\Delta E_{ij}/k_B T) \quad \text{if} \quad E_j > E_i$$
$$\nu_{ij} = \nu_0 * \exp(-2\alpha r_{ij}) \text{ if } E_j \leq E_i \qquad \text{Eq. 9}$$

Where ν_0 is the attempt (typical phonon) frequency, α is the inverse localization length, r_{ij} is the spatial distance between the sites and ΔE_{ij} is their energy difference. A single hop, along with the important parameters is sketched in Fig. 9(b).

In case of strong charge-phonon coupling, the transfer rate will follow the Marcus model [141] which assumes that every site can be modelled by a parabolic potential as depicted in Fig. 10(a), with its minimum being distributed according to the DOS. The energy barrier which needs to be overcome for a hop from one to another site is given by the energy at the intersection of their two parabolas E_a which is shown in Fig. 10(a). The full transition rate ν_{ij} is [137]:

$$\nu_{ij} = \frac{|J_{ij}|^2}{\hbar}\sqrt{\frac{\pi}{\lambda k_B T}} * \exp\left(-\frac{E_a^2}{4\lambda k_B T}\right) \qquad \text{Eq. 10}$$

Where J_{ij} is the transfer integral between the two wave functions (which scales with $\exp(-2\alpha r_{ij})$ like in the Miller-Abrahams-rate), $\hbar$ is the reduced Planck constant and λ is the Polaron activation energy (which equals four times the barrier of two identical parabolas). The main qualitative difference to Miller-Abrahams hopping is that hopping to a lower energy state becomes more probable until $E_a = 0$ which corresponds to $\Delta E_{ij} = -\lambda$, after which the transition rate decreases again. An electric field shifts the energy of the site, as sketched in Fig. 10(b), making jumps opposite the electric field (lower electron energy) more probable.

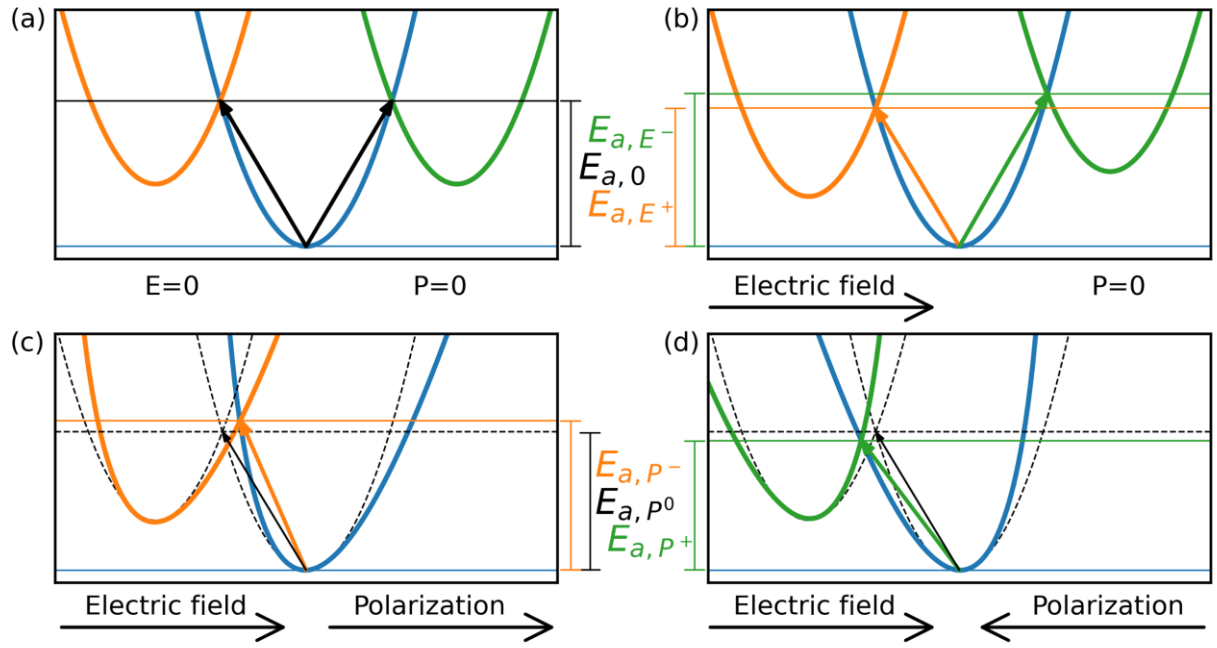

Fig. 10: Parabolic Marcus potentials together with the potential barrier; (a): without polarization and electric field, (b) With an electric field, which lowers the barrier along the electric field; (c) Comparison with (solid line) and without (dashed) polarization in line with the electric field, which increases the barrier; (d) like (c), but with the electric field in opposite direction, lowering the barrier, figure inspired by [151]

When considering the entire path of an electron, most hops have comparably high transition rates, while only one (or a few) are critical hops that limit the charge transport, which is described in the so-called percolation theory. Consequently, investigating the critical hop(s) is usually sufficient to understand all effects on the final conductivity. Finally, the current is also influenced by the injection barrier at the material-electrode interfaces. Simple models based

on inorganics consider mainly the Fermi-levels of the electrode and the HOMO (LUMO for hole-transport materials) as well as image charges and the applied electric field [142], while more sophisticated models also consider the disorder in organic systems [143], where it is important that the charge finds an appropriate site of low enough energy to avoid recombination with the image charge inside the electrode. A detailed explanation of these models is beyond the scope of this thesis, the important information is that a low injection barrier, *i.e.*, the Fermi energy of the electrode and the HOMO (LUMO) of the organic material being close together, improves conductivity which leads to bulk-limited conductivity, while a high injection barrier leads to an injection-limited current.

2. Charge transport in organic ferroelectrics

Traditionally, ferroelectrics are considered insulators, with interesting conduction properties at the domain walls [144], [145]. In the field of organic ferroelectrics, however, there is a growing number of materials, which are either designed to be (semi-)conducting [109], [146] or where a surprising conductivity was discovered [147]. The interesting observation was that for these materials, the conductivity depends on the polarization state [4], [109], [146], which was also seen in density functional theory (DFT) simulations [110]. As explained in the previous section, the current can either be bulk- or injection limited and both effects can be influenced by the polarization state.

The modulation of the injection barrier has been observed in many different systems, either in devices with a semiconductor and a ferroelectric sandwiched between metallic contacts [148] or directly by measuring the current through the ferroelectric [149]. In all cases, it was observed that the ferroelectric polarization decreases the injection barrier when polarization and field align and increases the barrier when they are oriented oppositely to each other. This was first attributed to the ferroelectric's counter charges, but more recent work indicates that stray fields in blends can cause the same effect. [150]

The effects on the bulk-conductivity were only discovered more recently and are explained by the Marcus model, modified to account for the effect of the aligned dipoles on the moving charge carriers [146], [151]. This leads to an asymmetric and anharmonic potential as shown in Fig. 10(c,d). When electric field and polarization align, the interactions lead to an increased energy barrier (Fig. 10(c)), while for opposing field and polarization, the energy barrier is decreased. This effect is present in all hops, but most importantly also in the critical hops, which limit the bulk conductivity. For this reason, the bulk conductivity is increased when the electric field is opposite to the polarization[4], [109], which leads to the opposite of the injection barrier modulation.

G. Effects of humidity on organics

The models for ferroelectricity and conductivity in organics, introduced previously, are limited in that they mostly only consider material parameters and temperature to predict electric

behavior. There are however many more external parameters that can influence electric characteristics, with humidity being the relevant one for this work.

Christie *et al*. observed that many hygroscopic organic materials show the same water content-conductivity dependence [152]: At very low water content (<1-5%) the conductivity is constant, then there is a strong increase of the conductivity. With increasing water content, the conductivity increases up to ten orders of magnitude. The constant conductivity is explained by other, proton-unrelated sources of conductivity. The water-dependent conductivity can be explained by protons hopping among unsaturated hydrogen bonds [153], which can result from the material itself or from absorbed water molecules. In this model, water is only assumed to change the mobility, but not the amount of (protonic) charge carriers.

This is confirmed by nuclear magnetic resonance (NMR) measurements of DNA. NMR uses a strong static magnetic field to split the nuclear-spin energy levels of spin-containing nuclei (like protons). A weak oscillating magnetic field to measure the resulting energy difference via the resonance frequency (Larmor frequency). This splitting depends on the local magnetic field, which is different from the large-scale magnetic field due to screening of the surrounding electrons. For this reason, NMR is useful for measuring the local electronic environment of protons. [154] The Larmor frequency usually has a certain width as the molecules have a slightly different environment. However, if the measured protons diffuse more rapidly than their spin-spin relaxation time, they will each see different environments and as the measured Larmor frequency will be the average of these environments, higher proton mobility leads to a narrower peak (motional narrowing). [155] This is exactly what was measured in DNA: Here, higher ambient humidity not only increased the conductivity but also decreased the NMR linewidth, indicating that the increased conductivity is caused by higher proton mobility. [156]

While the effect of humidity on conductivity in organics is reasonably well understood, the effects on ferroelectric behavior are only rarely investigated. While there are some investigations of how water can screen the polarization [157], [158], there are very few publications explaining how humidity changes the key characteristics of a ferroelectric. Huang *et al*. reported how humidity not only increases electrical and heat conductivity in the molecular ionic crystal of imidazolium perchlorate ($ImClO_4$), but also increases the remnant polarization [159]. The corresponding hysteresis curves shown in the supplementary information however show that a significant portion of this increase happens when the electric field is decreased from the maximal value back to zero. This behavior is not characteristic of ferroelectric polarization but is instead indicative of ionic migration. Additionally, the switching mechanism does not include water or protons. A similar behavior was observed for another ferroelectric proton conductor, where the ferroelectric state was observed to influence proton transfer, which was also claimed to increase the polarization [160]. Notably, both of these increases of polarization do not arise from an increase of classic ferroelectric polarization (the charges are shifted by a higher distance or more charges are switched), and for this reason it is unclear if an increased polarization has the same effects

(for example stronger piezoelectric coefficients) as a change in classic ferroelectric polarization.

Another observation on different cocrystals of anilic acids and 2,3-di(2-pyridinyl)pyrazine showed that a proton transfer which can be induced by pressure was needed to allow for ferroelectricity. Humidity was observed to show a similar proton transfer in a related material; however, it was not investigated whether this also induced ferroelectricity. [161]

In summary, it is well-investigated that humidity strongly improves protonic conduction in many materials. There are also several reports of how humidity influences certain parameters of some ferroelectric materials, there are, however, no systematic observations that show clear trends.

H. Proving ferroelectricity

After having introduced the basic properties of ferroelectrics, there still remains the question of how to experimentally identify a ferroelectric material, a challenge that forms the main focus of the first half of this work. In this chapter, I will first present the different methods by which ferroelectricity can be directly or indirectly measured and then analyze how this was applied for BTA and peptide-VDF ribbons.

Regarding the latter material, we do not believe that the presented data is sufficient to conclude beyond a reasonable doubt that the material is ferroelectric, which is why we published a response in the "Matters arising" format [1]. The review of the methods and discussion of the second material in this chapter is an extended and adapted version of this response.

The most direct approach to proving ferroelectricity of a material is to measure the $P(E)$-hysteresis curve by applying a triangular voltage signal and integrating the response current. Traditionally this is done by applying a single triangular voltage (hereafter labelled single wave (SW)) to the device, as depicted in Fig. 11(a) in red. A ferroelectric (experimental data for BTA, shown in Fig. 11 (a), purple) shows a strong current peak around its coercive field after which the current decreases with further increasing field. Other materials include a perfectly resistive material (blue, $I = V/R$, R=1GΩ), a perfect dielectric (orange, $I = C * dV/dt$, C =100 pF) and a leaky dielectric, modelled by resistor and capacitor in parallel (green, $I = V/R + C * dV/dt$). None of these exhibit the ferroelectric switching peak, facilitating the distinction between a ferroelectric and a non-ferroelectric.

To obtain the hysteresis curve, the previously shown currents are integrated and usually the mean is subtracted to obtain a hysteresis curve that is symmetric around P=0. The resulting charge can then be divided by the surface area (which is not always obvious as discussed in chapter In-plane-devicesIII.A.2) to obtain the polarization; however, working directly with the charge (often colloquially referred to as polarization in this context), as done here, yields the same qualitative behavior. This is plotted as solid lines in Fig. 11 (b). The ferroelectric (purple) depicts the typical hysteresis curve. When increasing the voltage from 0 V, the polarization is

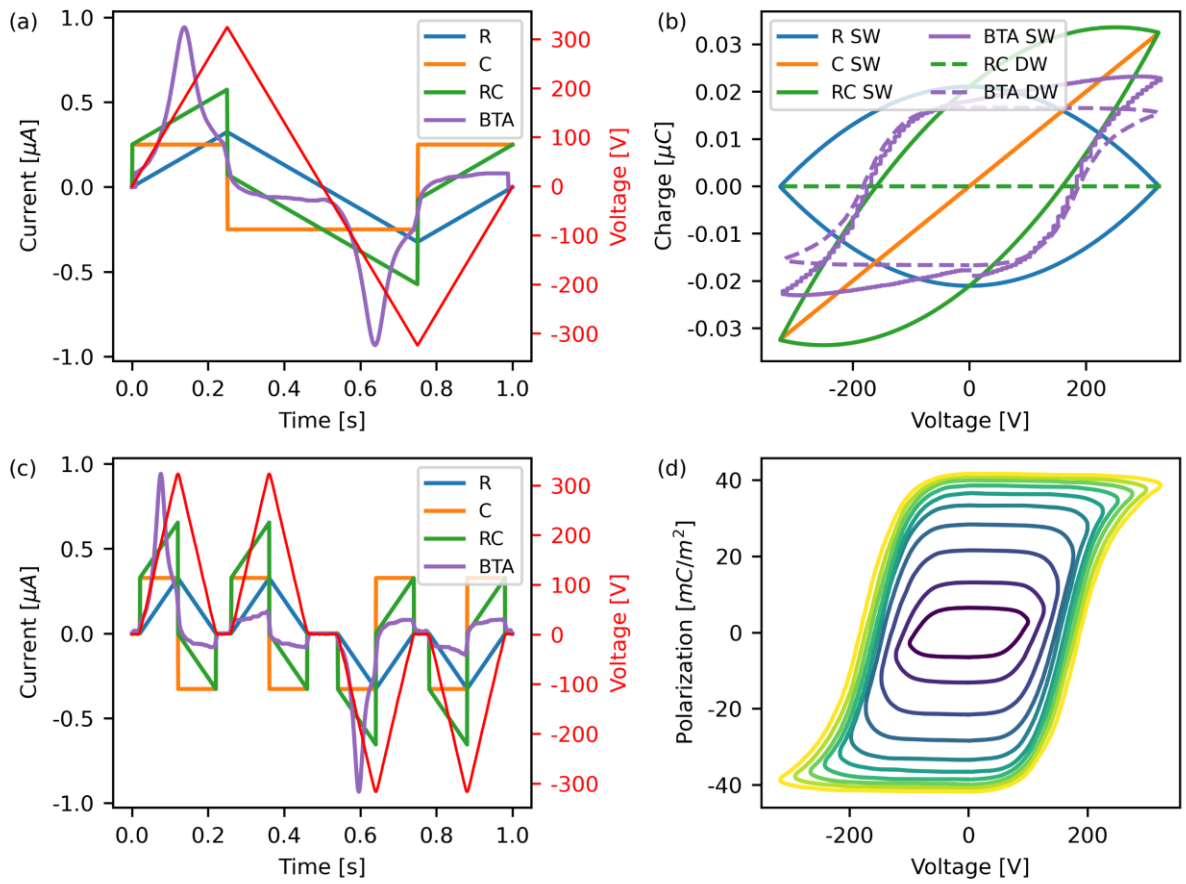

Fig. 11 (a) Current and Voltage (red) of triangular/single wave (SW) signal; (b) resulting hysteresis curves from (a) and (c); Current and Voltage (red) of double wave (DW) signal; (d) hysteresis curve of BTA for increasing maximum voltage; R=1GΩ, C=100 pF

initially almost constant but changes quickly when approaching the coercive field. Above the coercive field, when all the dipoles have switched, the polarization becomes nearly flat (it saturates). It is however not completely flat due to non-ferroelectric contributions (for example leakage and displacive currents). This flattening is the key characteristic of a ferroelectric hysteresis curve, as other materials (such as leaky dielectrics) can also lead to an open, but not-flattening, loop. While the dielectric (orange) does not show an open loop, the resistor shows an open loop with zero charge at maximum voltage. When considering the leaky dielectric, an open loop appears which at first glance resembles that of a ferroelectric. The polarization, however, does not saturate with increasing field, which shows that it is not the signal of a ferroelectric. Such “hysteresis curves” can be produced by any leaky dielectric, even with a banana. Unfortunately, there are many cases where open loops, which do not saturate are used as (often incorrect) proofs for ferroelectricity. [77] While a trained observer should be able to spot the difference between the curve of a ferroelectric and a leaky dielectric, there is a much more elegant solution, which also addresses the previously mentioned problem that the hysteresis curve of the ferroelectric has non-ferroelectric contributions.

This can be achieved by using a waveform such as the double-wave (DW) method[9], where two consecutive triangular voltage pulses are applied in each direction as depicted in Fig. 11 (c) in red [162]. The first voltage wave switches the ferroelectric and measures all other current contributions. The second wave measures only non-hysteretic current contributions. The associated currents for the different devices are plotted in Fig. 11 (c). It becomes clearly visible that the peak of the ferroelectric (purple) only appears in the first voltage wave, while all other currents stay the same in both waves. By subtracting the current in the second from the current in the first wave, one obtains only hysteretic contributions, which can then be integrated to obtain the hysteresis curve as shown in the dashed line in Fig. 11 (b). More details of the double wave measurement and other minor corrections are explained in chapter III.C.1. By using the DW-method, the hysteresis curve of the ferroelectric BTA (purple, dashed) becomes flat once all dipoles have switched, indicating that the hysteresis curve is purged from non-hysteretic contributions. The "hysteresis curve" of the leaky dielectric (green, dashed) becomes flat, indicating that there are no hysteretic contributions. However, it needs to be noted that ferroelectricity is not the only source of hysteretic contributions, with ionic hysteresis being the most prominent alternative. This is discussed in more detail in chapter IV.A, but ionic hysteresis still does not saturate with increasing field, which means that a saturating hysteresis curve is still a clear indication of a ferroelectric.

Furthermore, for a ferroelectric, certain trends should be observed:

- With increasing maximum voltage, the coercive field, remnant and saturation polarization should converge to one stable value, as can be seen in Fig. 11 (d).
- Increasing temperature should decrease the coercive field and, to a lesser extent, also the remnant and saturation polarization.
- Higher measurement frequencies should increase the coercive field and not affect the polarization (if the maximum voltage is sufficient to switch all dipoles given the higher coercive field). The two latter points were already explained in chapter II.B and are experimentally shown in chapter II.H.1 and V.

For ferroelectrics with conductivity modulation (as explained in chapter II.F.2), the hysteretic ohmic current is practically impossible to disentangle from the intrinsic polarization switching Consequently, even with the DW method, their polarization appears to increase with lower frequency as there is more time to integrate the current.

While the hysteresis curve is the most common electric measurement, the evidence can be supported by measuring the (differential) capacitance-voltage (CV) loop. It should show a

[9] This waveform is sometimes also called PUND (positive up, negative down)[160], while others only call two rectangular waveforms PUND [214]

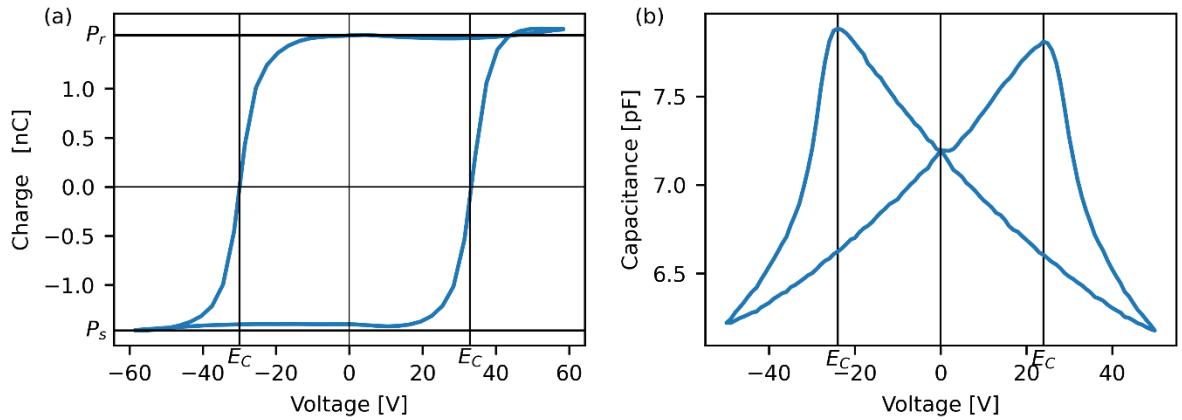

Fig. 12(a): hysteresis curve of poly(vinylidene fluoride-trifluoroethylene) [P(VDF-TrFE)], (b): its CV-loop. This figure is the same as Fig. 3.

characteristic butterfly shape with an increase of capacitance (permittivity) when switching occurs, but not when decreasing the voltage [163] after switching, as shown in Fig. 12(b). The capacitance peak occurs at the coercive field, which should be comparable (though usually somewhat lower due to the slower measurement) to that of the PE-loop, as can be seen in Fig. 12. While this measures only the reversible fractions of the polarization [164], the characteristic butterfly shape cannot easily be confused with another phenomenon, making this measurement less prone to misinterpretation. Consequently, to the author's knowledge, no disputed claim of ferroelectricity contains a CV-loop. Unfortunately, CV-measurements are still rarely used, possibly because some materials show only small fractions of reversible switching, thus not showing a strong butterfly shape.

Piezoelectricity can be measured with different measurement methods, the easiest of which is piezoresponse force microscopy (PFM) with the use of an atomic force microscope (AFM). It is performed by applying a sinusoidal voltage to the cantilever in contact mode[10] and measuring the amplitude and phase of the movement of the cantilever at this frequency with a lock-in amplifier. When looking at the PFM signal over the AFM scanning area, there will usually be a constant, electrostatic background signal. Additionally, topographic crosstalk can occur, which means that changes in sample height lead to an oscillation of the cantilever that appears in the PFM signal [165].

[10] There are new modes where cantilever oscillates in the kHz range and the piezo-measurement is performed in the period where tip and sample are in contact, reducing the friction between sample and tip.

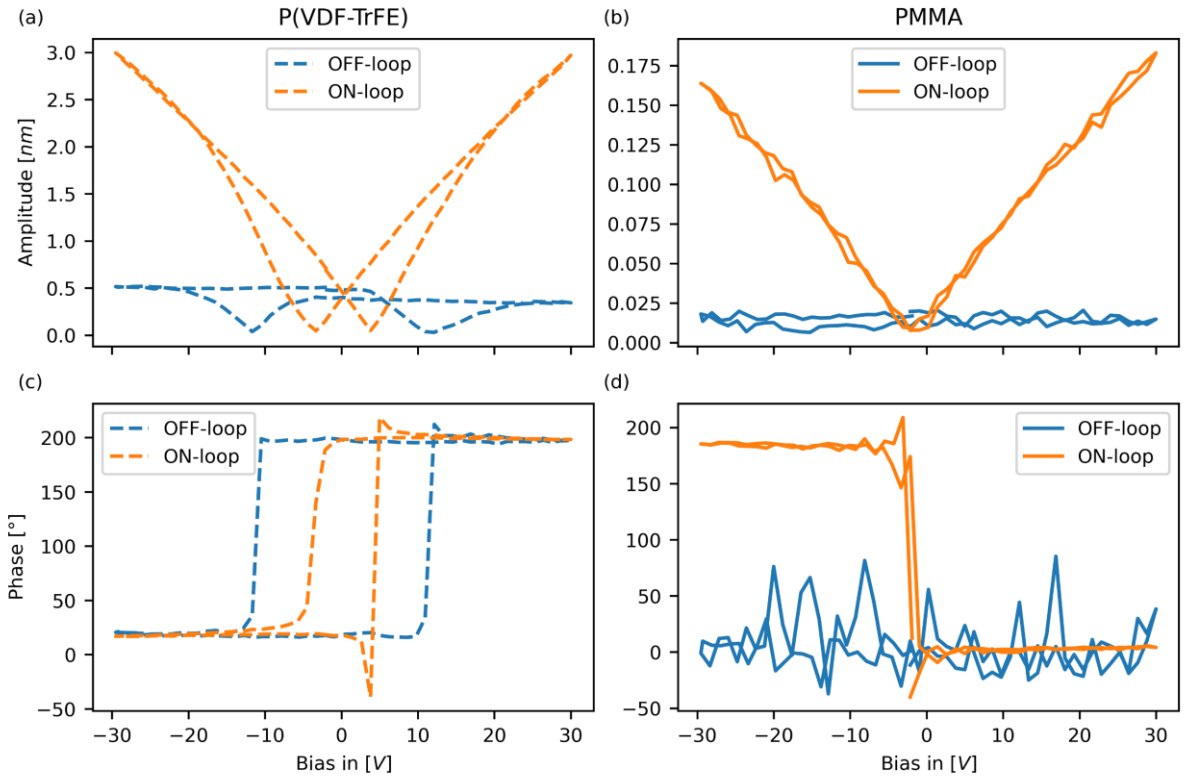

Fig. 13 PFM of (a,c) ferroelectric poly(vinylidene fluoride-co-trifluoroethylene) (P(VDF-TrFE)) and (b,d) non-ferroelectric poly(methylmethacrylate) (PMMA, right). (a,b): amplitude and (c,d): phase

Similar to polarization, the change of piezoelectricity in a ferroelectric material can be measured via PFM. In this "switching spectroscopy" mode, the tip stays at one point in contact and in addition to the small alternating voltage there is a bias which is swept slowly to switch the material. The interpretation of PFM signals is, unfortunately, complicated by the fact that many other effects can appear similar to piezoelectricity [166] most notably the electrostatic interaction between the cantilever and its surroundings. While the amplitude of a true piezoelectric signal only depends on the small signal amplitude, the amplitude of the electrostatic signal also depends linearly on the DC-bias corrected for the contact potential difference [167], the latter potentially being altered by charge injection [168]. The effect of the bias can be avoided via the use of "on"– and "off"–loops[11] [169]. This can be seen in Fig. 13, where the on-loop of the ferroelectric material is dominated by electrostatics and only the off-loop produces the expected stable amplitude. The on-loop of a non-ferroelectric PMMA looks qualitatively similar to that of P(VDF-TrFE) and only the off-loop shows that the signal is purely electrostatic. Interferometer-based setups, either implemented in the atomic force microscope or stand-alone (as used for Fig. 4 (c)) can help to distinguish electrostatic from piezoelectric effects [170].

[11] Charge injection can create PFM off-loops which resemble that of a ferroelectric. Similar to wrong polarization hysteresis curves, they do not saturate with increasing voltage. Open-loop contact kelvin probe force microscopy can help distinguishing the two phenomena. [168]

An indirect way to prove ferroelectricity is the detection of the ferro– to paraelectric phase transition, which is the upper temperature limit for ferroelectricity as already discussed in chapter II.A. It is marked by a divergence of the susceptibility around the Curie temperature, with Curie-Weiß behavior ($\frac{1}{\chi(\mathrm{T})} = \alpha_0(T - T_c)$) in the paraelectric phase [73], as discussed in chapter II.A. Ferroelectricity should be observable below, but not above this temperature. The observation of Curie-Weiß behavior does, however, not directly prove ferroelectricity, for example pyroelectric materials which have a polarization which cannot be switched by an electric field show the same characteristic. The observation of Curie-Weiß behavior can, however, not be considered necessary to prove ferroelectricity as some materials, most notably PVDF, degrade or melt before reaching the hypothetical Curie-temperature [98].

Two other indirect methods to show the lack of inversion symmetry, which is necessary for ferroelectricity, are second harmonic generation (SHG) [171] and X-ray diffraction (XRD). SHG is however experimentally challenging and requires specialized setups as well as well-behaved crystals, so it is not commonly employed and will therefore not be further discussed here. In contrast, XRD is probably the most commonly employed structural characterization method and can, in many cases, reveal the lack of inversion symmetry. It can, however, not detect protons, so it cannot reveal how their positions break inversion symmetry.

There is no clear consensus on what experiments are needed to prove ferroelectricity. In principle, a well-behaved polarization hysteresis loop, CV curve or piezoelectric switching measurement should be sufficient to prove ferroelectricity. However, as one single measurement result is often not definitive, a combination of multiple measurements is usually a better proof. In the personal opinion of the author, sufficiently strong evidence could for example be achieved by the following combination of measurements:

- A set of saturating hysteresis loops where coercive field and polarization show the correct dependence on temperature and frequency (optionally also maximum voltage).
- A saturating hysteresis loop paired with a butterfly-shaped CV loop, both showing a similar coercive field.
- A saturating hysteresis loop and piezoresponse switching measurements that are not dominated by electrostatic signal.

These results can be supported by indirect measurements (Curie-Weiß, SHG and XRD), they are, however, not sufficient to prove ferroelectricity by themselves. An additional, optional feature to make the result more plausible is an explanation on how the polarization can be inverted on the atomic/molecular level.

In the following, it will be discussed how the experimental proof was established for BTA and why we believe that the data for Peptide-VDF oligomers is not sufficient for the same conclusion.

1. Case study BTA

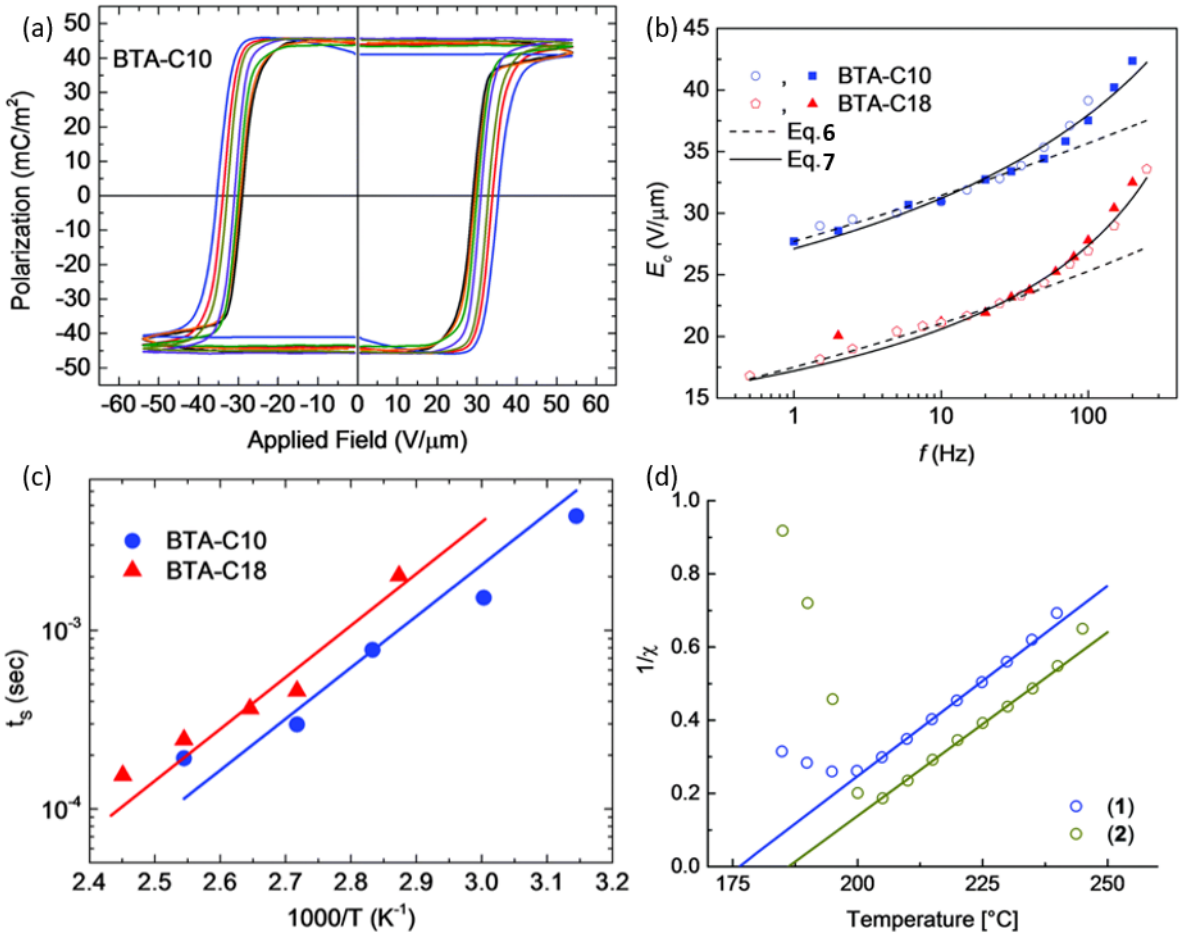

Fig. 14 Ferroelectric measurements of BTA; (a) hysteresis curve of BTA-C10 for different frequencies; (b) resulting Coercive field vs. frequency plot with fits to the Ishibashi–Orihara (Eq. 6) and Du–Chen (Eq. 7) model for BTA-C18 and BTA-C10 (difference is in the length of the alkyl side-chain); (c) Switching time vs. temperature measurements for BTA-C18 and BTA-C10; (d) Curie-Weiß behavior of BTA-C18 for a badly (blue) and well aligned (green) sample, all subfigures reproduced from [76]

BTA is a supramolecular, liquid crystalline polymer which was already introduced in chapter II.D.2. Its ferroelectricity was first proven by Gorbunov *et al.* [76]. The hysteresis curve for frequencies between 1 and 100 Hz is depicted in Fig. 14 (a). At low frequency (e.g., the black curve), the hysteresis curve shows the typical flattening above the coercive field, indicating ferroelectricity. Increasing the frequency leads to a higher coercive field but does not change the polarization values. The changing coercive field is explicitly plotted in Fig. 14 (b) and fits the Du-Chen model well. While there are no temperature dependent hysteresis curves shown, the temperature dependent switching time was measured with the help of rectangular voltage pulses. The results are shown in Fig. 14 (c) and match the expectations for a ferroelectric. The temperature-dependent permittivity, plotted in Fig. 14 (d), follows the Curie-Weiss law. Interestingly, only the well-aligned sample (green) follows the Landau theory prediction, that the permittivity in the ferroelectric phase should have a Curie-Weiß-like behavior with twice the slope (Eq. 5).

In total, these measurements show that BTA exhibits a hysteretic behavior that saturates across the coercive field and has the right temperature- and frequency-dependent behavior.

Additionally, there is an indication of a ferro- to-paraelectric phase transition which should be considered sufficient to prove ferroelectricity. Later measurements [81] also showed the butterfly-like CV-loop and the piezoelectric switching, further supporting the already strong evidence for ferroelectricity.

2. Case study Peptide-PVDF

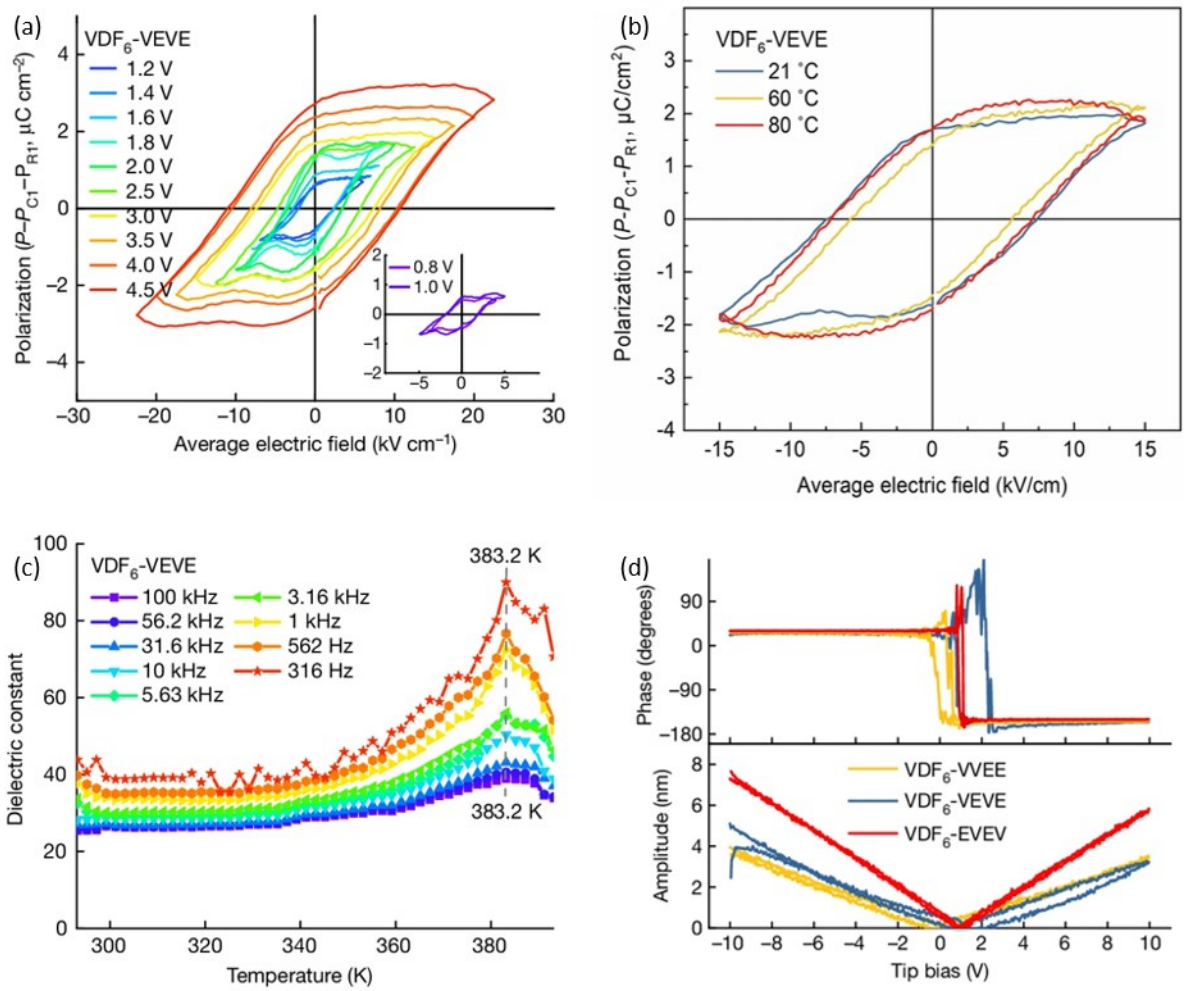

Fig. 15: Different measurements of VDF_6-VEVE: (a) hysteresis curve for different maximal voltages; (b) the hysteresis curve for different temperatures; (c) measurements of the temperature-dependent permittivity; (d) piezo-switching-spectroscopy with different peptides, all subfigures are reproduced with permission from [172]

Recently, Yang et al. reported on their findings of VDF-oligomers paired with tetrapeptides, claiming ferroelectricity with coercive fields much lower than PVDF [172], an effect attributed to supramolecular dynamics. Here we argue that the presented data, including non-saturating hysteresis loops, are insufficient to prove ferroelectricity beyond a reasonable doubt. As these are the basis for the main conclusions of the publication by Yang et al., their inconclusiveness necessitates further experiments. To explain our concerns, the data for VDF_6-VEVE is reproduced in Fig. 15; the data for many other VDF oligomer-peptide combinations can be found in the original publication [172]. All references to Supplementary figures in this section refer to the supplementary information of this publication. Our two main points of concern are:

1. As mentioned in the previous section, the hysteresis curves should saturate above the coercive field and consecutive loops with higher driving voltages should not yield much higher polarization values. None of the shown P-E loops for the in-plane setup, including those for VDF_6-VEVE (Fig. 15(a)) and the PVDF and P(VDF-TrFE)[12] reference samples (SI Fig. 19) show reliable saturation. While some inner loops (e.g. inset of Fig. 15(a)) seem to level off, the outer loops, where saturation actually should occur (cf. Fig. 11 (d)), continue to grow monotonically with increasing driving voltage. The dominant problem in these measurements appears to be the suboptimal device architecture (in SI Fig. 11), in which the response is dominated by the capacitance between the electrode and the silicon substrate, resulting in the device behaving close to a perfect capacitor and the material contributing less than 5% of the signal (SI Fig. 18). While this is theoretically compensated for, small deviations in the compensation will lead to major changes in the signal attributed to the material. Additionally, the temperature-dependent hysteresis curves (e.g. Fig. 15(b)) do not show a systematic decrease of the x-axis intersection with increasing temperature, as would be expected for the coercive field of a ferroelectric.

2. The PFM spectra (Fig. 15(d)) show an inversion of the phase at ~1 V., which the authors attribute to ferroelectric switching. However, the PFM amplitude scales linearly with the bias voltage. This behavior is inconsistent with true piezoelectricity, where the amplitude should depend on the AC drive voltage rather than the DC bias. Instead, a bias-dependent amplitude is characteristic of electrostatic artifacts, as demonstrated in Fig. 13.

In summary, we do not think that the data provided by Yang et al. allow to establish, with sufficient certainty, ferroelectricity in the investigated supramolecular assemblies and that new and/or improved measurements are needed to convincingly prove ferroelectricity. Although the crystallographic data (Fig. 2 of Yang et al.) indicate that the material is in the polar β-phase, this does not prove that the polarity can be switched at the suggested low electric fields. For example in as-cast P(VDF-TrFE), poling is still needed to obtain ferroelectric behavior, despite the being in the polar phase already [103].

[12] This agrees with my general experience that P(VDF-TrFE) does not show well-behaved polarization curves for in-plane setups as the polymer chains lie in plane and the polarization can only be perpendicular to the chain. In contrast, out-of-plane setups (electric field perpendicular to the substrate) show well-behaved hysteresis curves, which was also observed by them in SI Fig. 20.

III. Methods and sample preparation and evaluation

After having discussed the properties of ferroelectrics and which measurement results are sufficient to prove ferroelectricity, we now turn to the experimental methods used to obtain these results. After discussing how to prepare the material and produce devices, there will be a short introduction of the different measurement setups and then an explanation on how certain measurement protocols are evaluated.

A. Sample preparation and geometry

There are many different ways to measure electric properties of a material. The simplest approach would be to connect a multimeter to the material with probe needles. While this is easy to perform, it does not allow for good reproducibility and will not yield any quantitative results. In practice, the use of an "out-of-plane" device has proven to be the setup that produces the best quantitative results and allows for high electric fields. For the materials in this work, it was however not known how to produce the films needed for these devices, so pre-fabricated interdigitated electrodes (IDEs) were used instead. While IDEs simplify device fabrication, they often yield only qualitative trends, making the extraction of absolute material parameters difficult. The difference between the two devices as well as the challenges of evaluating data measured with IDEs will be discussed in the following.

1. Out-of-plane devices

Out-of-plane devices are devices where the electric field is out of the device-plane. One such setup as well as a photo of the actual device is shown in Fig. 16 (a&b). The general idea is that the material is sandwiched between two metal electrodes, forming a plate capacitor. Practically, the first metal film is deposited (usually with a thermal evaporator) on a cleaned glass substrate. It often has a keyhole-shape as seen in Fig. 16 (a). The long strip is useful as shifting the structure does not change the overlap area with the other electrode and the round area is useful for easy connection to the measurement device. A narrow strip is usually desirable as a wider strip increases the probability of the final device short-circuiting.

The material is meanwhile dissolved in an appropriate solvent and then spin coated[13] on the substrate. Spin-coating is a commonly used method for thin-film formation and works by rotating the substrate with a solution of the material on top. Centrifugal forces result in only a small film of the solution staying on the substrate and the solvent quickly evaporates. The film thickness can be influenced by the concentration of the solution and the spinning speed. Typical thicknesses are between 50 nm and several micrometers. [173] Finally, the second electrode is evaporated on top of the material film.

The final device is a parallel-plate capacitor with the area being the square of the strip width and the spacing being the film thickness, therefore the basic equations like as $C = \epsilon_0 \epsilon_R \frac{A}{d}$ or $E = V/d$ apply. This makes it easy to convert the measured results to material parameters like conductivity, permittivity or polarization. As the top-contact is deposited on the material

[13] Other deposition techniques like thermal evaporation are also possible, but only rarely used.

film, a single hole in the overlap area will lead to the two contacts touching each other, short-circuiting the device. For this reason, only materials with well-established film fabrication protocols are suitable for this kind of device. Unfortunately, the materials used in this work are not well-investigated and a good spin-coating procedure could not be established. For this reason, it was not possible to use out-of-plane devices and IDEs were used instead.

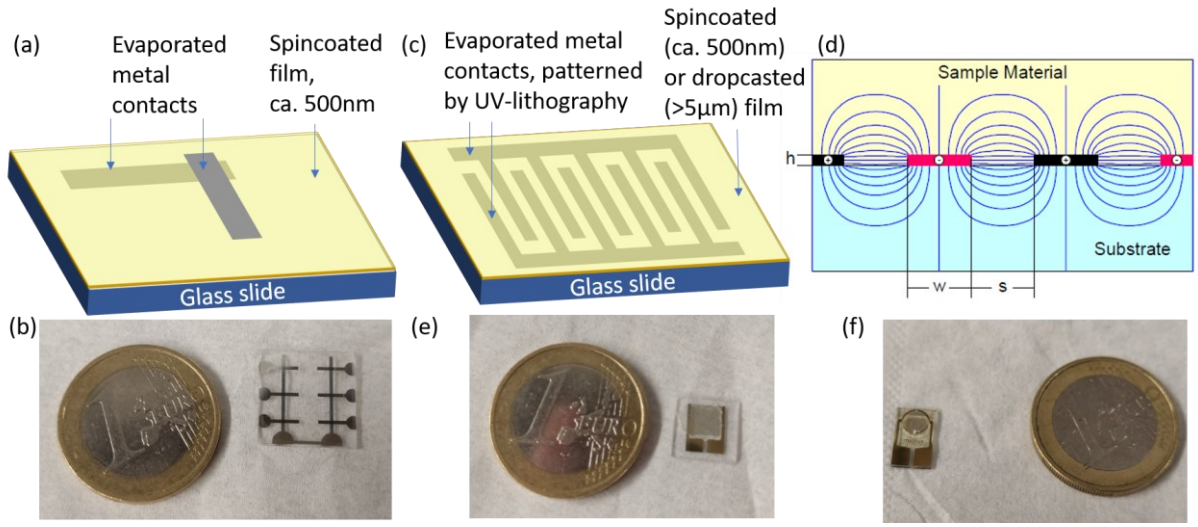

Fig. 16 (a) Sketch of an out-of-plane device; (b) photo of the actual device; (c) sketch of an interdigitated electrode; (d) Sketch of the electric field in an IDE, subfigure reproduced from [217] *(e) photo of a homemade and (f) of a commercial (Micrux) IDE);. In the photos, the 1€-coin serves as a size-reference.*

2. In-plane-devices and Interdigitated electrodes

In-plane devices are a class of devices where the electric field lies in the plane of the device. This can be achieved by two metallic layers with a gap in-between them. However, a single channel will only lead to a very small capacitance (<<1 pF), so it is better to use many channels. This is achieved by Interdigitated Electrodes (IDEs), where many channels are connected in parallel as sketched in Fig. 16 (c) and its cross-section in Fig. 16 (d).

The device is generally characterized by the spacing S, the electrode width W and the total electrode length l (number of pairs multiplied by the length of the single electrode). Practical devices generally have a spacing between 1 and 20 µm, a length in the range of millimeters and 50-1000 parallel channels connected to contacting pads. In this work, two different substrates were used: The homemade IDEs (photo in Fig. 16 (e)) have a 5 µm gap, a squared electrode area of 4.5×4.5 mm^2 and 225 electrode pairs. The total electrode length is 2.013 m. There were also homemade IDEs with 1 and 2 µm gaps available (their electrode lengths are 5.031 m and 10.067 m) which can yield higher electric fields. As this was not necessary for the materials in this work, they were not used here. The other IDE used was the commercial IDE3-Au by Micrux [174] with a 5 µm gap and a circular area with 3.5 mm diameter and 180 electrode pairs. The total electrode length is 0.80 m. A photo of this IDE is provided in Fig. 16 (f).

While the IDEs simplify device fabrication and reduce reliance on perfect film quality, they have the big disadvantage that they produce an inhomogeneous electric field (shown in Fig.

16 (d)), which makes the physics of the device more complicated, This will be discussed in more detail in the following two sections. Consequently, $E = V/S$ only applies in the small region between the electrodes, while other regions have a lower field [175]. For practicality, this formula is still used to give an upper limit of the electric field. While it is possible to calculate the capacitance analytically [176] there is a simple, empirical formula giving acceptable results for half[14] the capacitance of the electrode in vacuum (ignoring permittivity) C_0/l (in pF/m) [177]:

$$C_0/l = 6.5 * \left(\frac{W}{L}\right)^2 + 1.08 * \left(\frac{W}{L}\right) + 2.37 \qquad \text{Eq. 11}$$

With $L = W + S$. The capacitance of the real device with material (with thickness t) is:

$$C = C_0 * \epsilon_{sub} + C_0 * [\epsilon_{mat} * F\left(\frac{t}{L}\right) + \epsilon_{air} * \left(1 - F\left(\frac{t}{L}\right)\right)] \qquad \text{Eq. 12}$$

with ϵ_{sub}, ϵ_{mat}, ϵ_{air} being the dielectric constant of the substrate, the material and air and $F\left(\frac{t}{L}\right)$ being a function that accounts for a limited layer thickness which goes to unity when t approaches L [178].

a) Comsol simulations

To confirm these results, a micrux IDE was already simulated in the author's master's thesis [179] with the finite-elements method simulation software Comsol Multiphysics [180]. The main result was that $C_0 \approx$ 5.1 pF and, as $C_{empty} \approx$25-30 pF, $\epsilon_{sub} \approx$ 4.5. The value of C_0 is considerably higher, than what Eq. 11 yields (3.6 pF). Possible explanations include edge effects of the electrodes as well as numerical artifacts. This difference was not further investigated, as the absolute value of C_0 was not important in this work and the values are still within the same order of magnitude, ruling out fundamental conceptual errors.

To gain further insight into the effects of film thickness and surface roughness, the system was simulated for a two-dimensional IDE with one repeat unit and periodic boundary conditions (pbc) and the resulting capacitance was calculated. The electrodes are on the substrate (ϵ_{sub}=4.5) and then there is a material layer with varying thickness t and permittivity ε and a layer of air (ϵ_{air}=1) on top. The general shape and the electric potential after applying 1 V to the outside electrodes are shown in Fig. 17 (a) for the example case t=2 µm, ε=64. The white area on the sides marks the region outside the PBC-box. The total height of the system is 50 µm.

To see the effects of the surface, the electric field at the surface is plotted in Fig. 17 (b). This clearly shows that the surface roughness has strong effects on the electric field distribution and consequently influences the device capacitance.

[14] Half the capacitance is useful as top and bottom usually consist of two materials on top and bottom, as can be seen in Eq. 12

The general trends for different permittivity and layer thickness can be seen in Fig. 17 (c). As expected, a higher material thickness leads to a linear increase in capacitance, which saturates around between 5 and 10 µm ($t \approx L = 2S$). Interestingly, comparing the capacitance between rough and smooth surfaces (Fig. 17 (d)) shows that the rough surface appears to lower the capacitance at low material thicknesses while increasing it at high thickness. This trend becomes stronger as the permittivity increases.

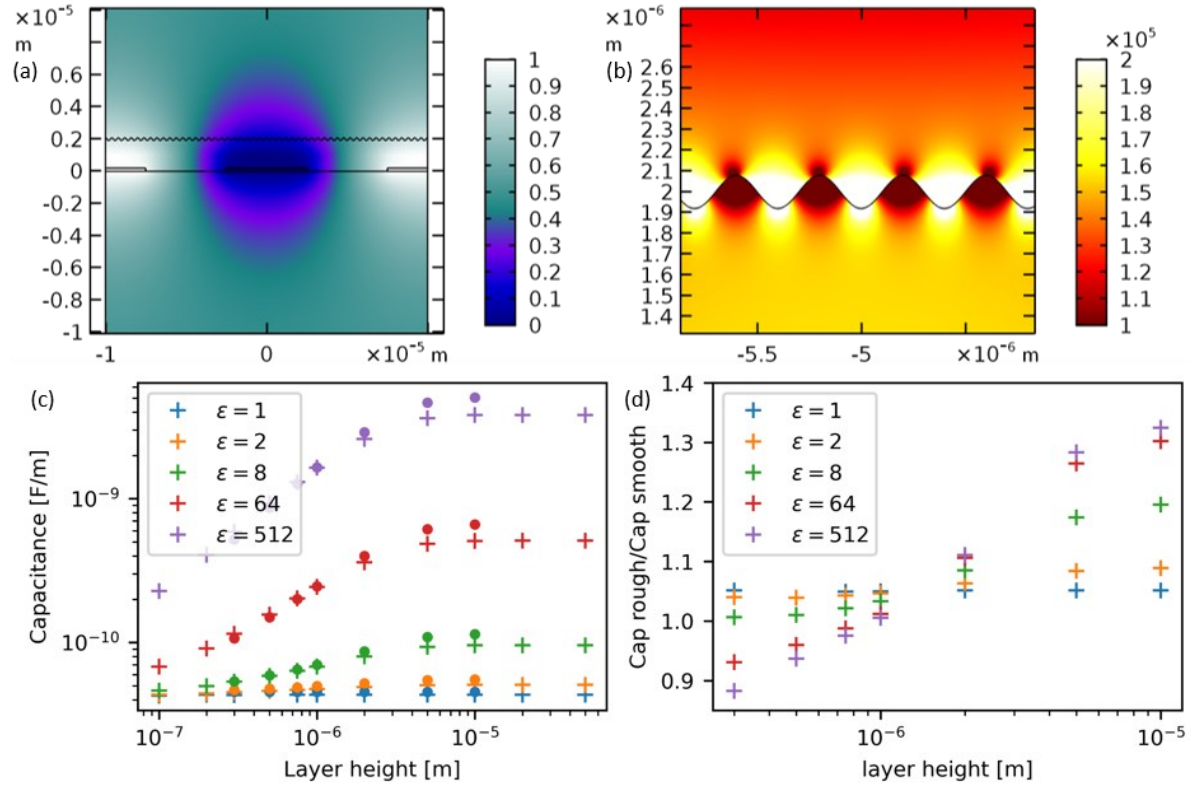

Fig. 17 (a) General overview of the simulation with rough surface, the color codes the potential in V; b) zoom into the rough surface with color showing the absolute electric field; t=2 µm, ε=64 for (a) and (b); (c) Height-dependent capacitance for different permittivity with smooth (+) and rough (dots) surface; (d) relative changes through rough surface.

Additionally, a rough surface apparently increases the capacitance for ε=1. This is implausible as this surface is the transition area between material and air, which are both the same (ε=ϵ_{air}=1). Thus, there is no real interface which can change the capacitance. The observed deviation likely stems from mesh generation artifacts as the mesh is significantly denser near the complex rough interface than between the electrodes, even though the inter-electrode gap is the most critical region. Additionally, the results already showed that the region far away (> 5 µm) from the electrodes should not be relevant. Consequently, the capacitance at high layer thicknesses should not be significantly altered by the surface roughness. These seemingly implausible results are likely attributed to the difficulty of modeling the rough surface with the triangular and rectangular shapes used in the mesh, resulting in a very fine mesh around the interface which also changes the measured capacitance. The observation that the capacitance decreases at low thicknesses seems plausible, but can hardly be relied upon given the presence of these numerical artifacts. Therefore, no further simulations were performed.

b) Polarization IDE

Measuring the capacitance of these devices is only the starting point of understanding IDEs. Crucially, we must determine how to convert the charge, obtained by integrating the current from Double Wave (DW) measurements, into intrinsic material polarization. In our case, this is rendered more difficult as the material layer is usually not smooth and the permittivity of a ferroelectric depends on the electric field and the polarization state (hysteresis).

Starting from the simple case, where the surface is smooth and the electric field is strong enough to switch the polarization of the entire material, the relevant surface area is obtained by the total electrode length l, multiplied by the material thickness t and the polarization is thus [175]:

$$P = \frac{C}{t * l} \qquad \text{Eq. 13}$$

This formula however only holds if the entire material is switched. It is known and also observed in the COMSOL simulations, that the electric field is "sucked" into regions of high permittivity. When increasing the electric field from zero, the material between the electrodes, where the field is strongest, switches first. This leads to an increase in permittivity (as discussed in chapter II.B) that can shield the further away regions from the electric field, thus preventing them from switching. This is however only very difficult to calculate as $\epsilon(E)$ generally is unknown (CV-loops only measure an average over the entire sample and cannot account for these local variations. Even if this function were known, the entire system, including the typically undefined surface topography, would require iterative solving for increasing field steps. As this is complex, even if all parameters were known, this was not performed here.

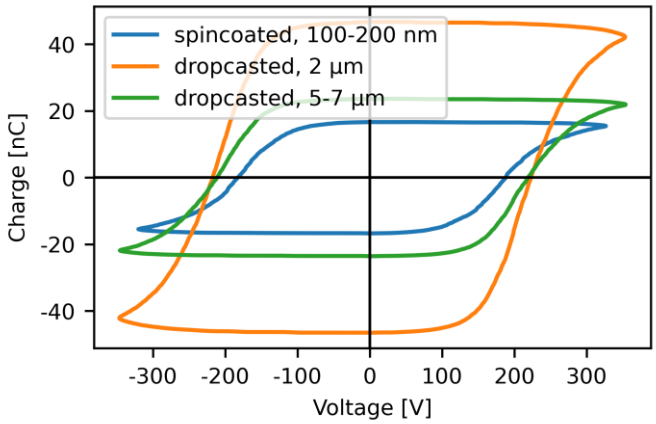

Fig. 18: Hysteresis curve of different BTA films on a homemade IDE

Instead, the charge of a known ferroelectric (BTA-C10) was measured and the effective thickness t_{eff} was calculated using the known polarization, which was measured with out-of-plane devices [106]. There was a spin coated film and two drop-casted films with thicknesses of 100-200 nm of 2 µm and 5-7 µm thickness respectively (Appendix 3). Their hysteresis curves

are plotted in Fig. 18. The spin coated film has a remnant charge of 17 nC, the drop-casted films show 23.5 nC (5-7 µm film) and 47 nC (2 µm film). For the spin coated film, this charge is consistent with Eq. 13[15], indicating that the entire film thickness is switched. For the thicker films, the total film thickness seems to be irrelevant as the thicker film has only half the charge.

Instead, other factors like film quality seem to be more relevant and only the lower 300-600 nm appear to be switched.

Given the large uncertainty and the unclear transferability to other materials, this value should be treated as a rough estimate of the effective switching depth and used with caution.

c) Film formation

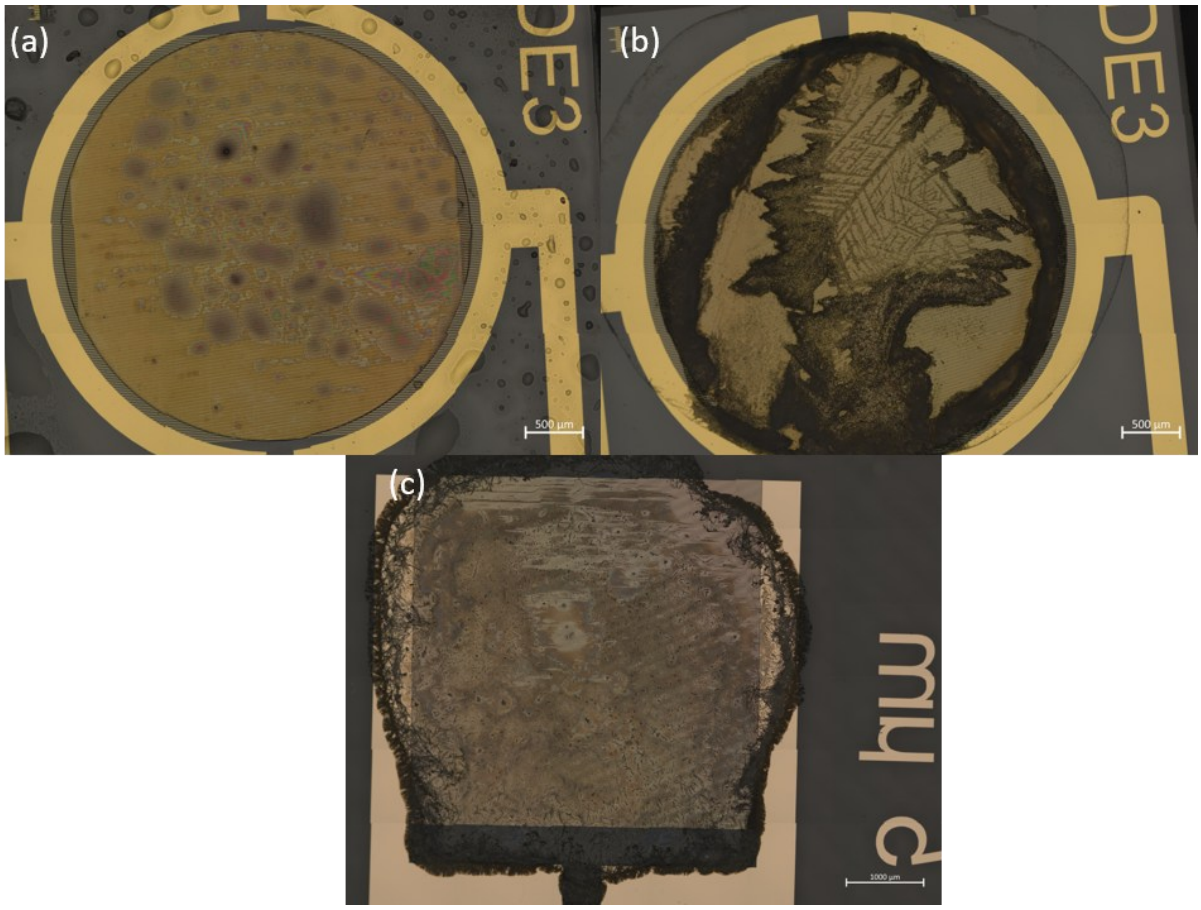

*Fig. 19: Microscope images of the used samples for the overview section: (a) **material 1**; (b) **material 2**; (c) **material 4**; All samples were already aged when the image was taken, which is why only residues of **material 1** can be seen.*

After having cleaned the IDEs in an ultrasonic bath with soapy water, deionized water, acetone and isopropanol, a 5µl drop of the material solution (10 mg/ml in ethanol for **material 1** and **3** of the screening study in chapter IV and 10 mg/ml in water for **material 2** and **4)** was drop-casted on the IDE. This resulted in rough, polycrystalline, 1-10 µm thick films which covered approximately half the electrode area. Images of the samples can be seen in Fig. 19. For this reason, the effective area is only approximately half the electrode area, which needs to be

[15] Calculated using $P_r = \frac{C_r}{l*t} = \frac{1.7*10^{-8}C}{2.013m*(100-200)nm} = 84 - 42mC/m^2$, literature value: 45 mC/m² [106].

considered when calculating the polarization from the charge. Consequently, the formula that is used to calculate the polarization is:

$$P = \frac{C}{l * t_{eff}/2} \qquad \text{Eq. 14}$$

With l = 0.80 m for micrux (**material 1-3**) and l=2.013 m for homemade (**material 4**) IDEs and t_{eff}=300-600 nm.

The estimated polarization is only the switchable polarization along the axis of the electric field. For a set of randomly oriented, immoblie dipoles in three dimensions, this is half[16] of the total polarization. This value can however vary if the polarization is not randomly oriented (e.g. in flat lying polymers), the dipole axis can be reoriented by the electric field (like in BTA), or if the crystals structure allows for more than one "ferroelectric direction" (like in perovskites).

B. Setups

After having introduced the geometry and production of samples, we now briefly describe the measurement protocols. A measurement setup usually consists of a probe station which is used to contact the device and control environmental parameters. This probe station is then connected to an electric measurement device which typically generates the voltage and measures the current.

1. Probe stations

The simplest probe station employed was the "air probe station". In this setup the sample is stationed in ambient conditions and can be heated up to about 150 °C. A photo of this probe station is provided in Fig. 20 (a).

The second probe station was the so-called "vacuum probe station", a cryostat which allows sample connection in a vacuum. The temperature can be varied between 78 K and about 400 K. A photo is shown in Fig. 20 (b).

The last and most commonly used probe stations were two different versions of the LINKAM HFS600E-PB4 stage [181]. They allow measurements between -195 °C and 600 °C in nitrogen and between room temperature and 600 °C in air (otherwise water condensation would lead to problems). The two different versions only differ in size. Both are shown in Fig. 20 (c) and (d). While the bigger one is often more practical, it occupies more space. This is particularly important when putting the stage into the electro-tech-systems M 5504-7621 humidity control box [182] as it was frequently done to make measurements varying ambient humidity. This humidity control station is shown in Fig. 20 (e).

[16] $\int_0^\pi \sin(\theta)\, abs(\cos(\theta)) d\theta / \int_0^\pi \sin(\theta)\, d\theta = 1/2$ as there is no ρ-dependence when choosing the appropriate spherical representation.

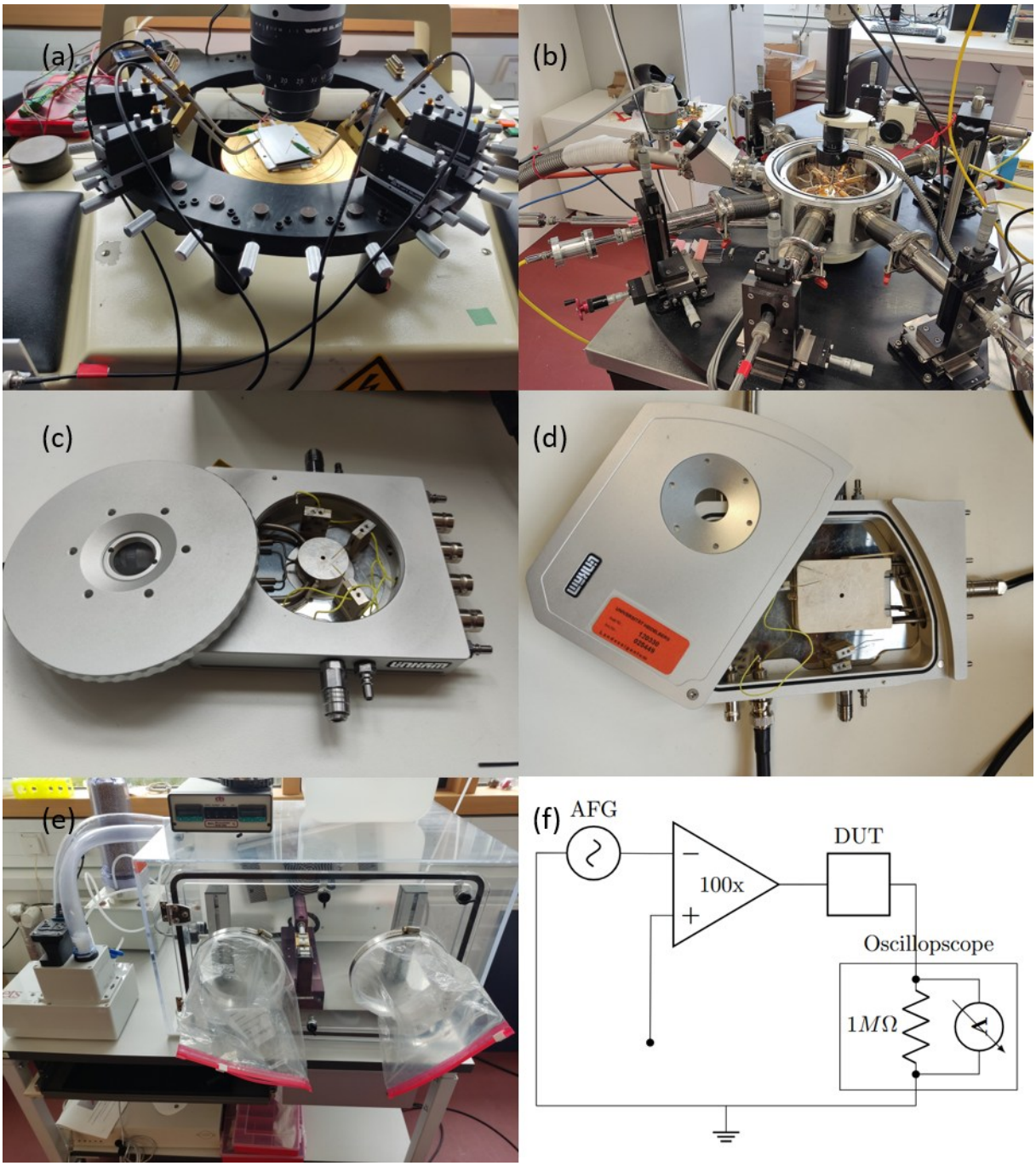

Fig. 20: Photos of different setups: (a): Air probe station; (b) vacuum probe station; (c) small Linkam stage; (d) big Linkam stage; (e) humidity control box; (f) sketch of self-constructed measurement setup

2. Measurement devices

Various devices were used to measure the samples after contacting them in the probe stations. The first setup, which was typically combined with the air probe station was a custom-built setup consisting of an input signal supplied by a Tektronix AFG3052C Dual Channel Arbitrary/Function Generator, amplified by a TReK PZD350A high voltage amplifier and measured by a Tektrinox TBS 1102B-EDU oscilloscope. How the different devices are connected together is sketched in Fig. 20 (f). It was used to apply a waveform (usually the DW-waveform) with up to 330 V to the sample and measure the response current across the 1 MΩ input resistor of the oscilloscope.

The second device was a Zurich instruments multifunctional impedance analyzer (MFIA) [183] employed to measure the complex impedance of the device as a function of bias (max 10 V) and frequency. Together with the vacuum probe station, the Linkam stage and the humidity control box it was also possible to perform temperature and humidity sweeps in air and vacuum, providing a versatile measurement platform.

The last electrical measurement device was the Aixacct TF Analyzer 2000E [184], which was part of the research line double DBLI [185]. It allows the application of arbitrary waveforms to the sample and the measurement of current response and bias-dependent impedance with voltages up to 400 V. It was usually used in combination with one of the Linkam stages.

3. Piezoelectric characterization

Piezoelectric measurements were performed by piezoresponse force microscopy (PFM) with a Bruker multimode atomic force microscope (AFM). For this, a sinusoidal voltage was applied to the cantilever and its oscillation at that frequency was detected by the built-in lock-in amplifier and then split into the amplitude of the signal and the phase with respect to the applied curve. The available DBLI also allows to make switching spectroscopy measurements (as shown in Fig. 3(b)). It works by reflecting the laser off the top and bottom electrode of an out-of-plane device and measuring the variation in the spacing between the two by an interferometer. However, as this technique requires out-of-plane devices, which could not be successfully fabricated for these materials, it was not employed further.

4. XRD

Powder X-ray diffraction (PXRD) measurements were carried out on a Bruker D2 Phaser diffractometer with a Copper source with Cu K_α (λ = 1.541 Å) and a molybdenum source with Mo K_α (λ = 0.702 Å) radiation in Bragg-Brentano configuration by Manjunath Balagopalan at the University of Oslo.

C. Evaluation

This section provides a detailed overview of how the measured signal was evaluated.

When measuring the materials presented in this thesis, it was noticed that the DW and CV measurements contained signals which cannot be attributed to ferroelectricity. To isolate the intrinsic ferroelectric response, these non-ferroelectric contributions were compensated for. Since the results for these materials is presented in the two primary publications [2], [3] and this compensation method was used there for the first time, this section is also based on its supplementary information.

1. DWM

The idea of the double wave method (DWM) is that the first triangular voltage wave switches the material while the second one functions as a background measurement, capturing all non-hysteretic effects (leakage current, displacement current, etc.). Consequently, the current

measured during the first pulse contains both switching and non-switching contributions, whereas the second pulse contains only the latter. The waveform can be seen in Fig. 21(a). The difference in current is then assumed to be the switching current which is integrated to obtain one half of the hysteresis curve. This is displayed in Fig. 21(c). This process is then repeated for the opposite direction to obtain the other half of the loop.

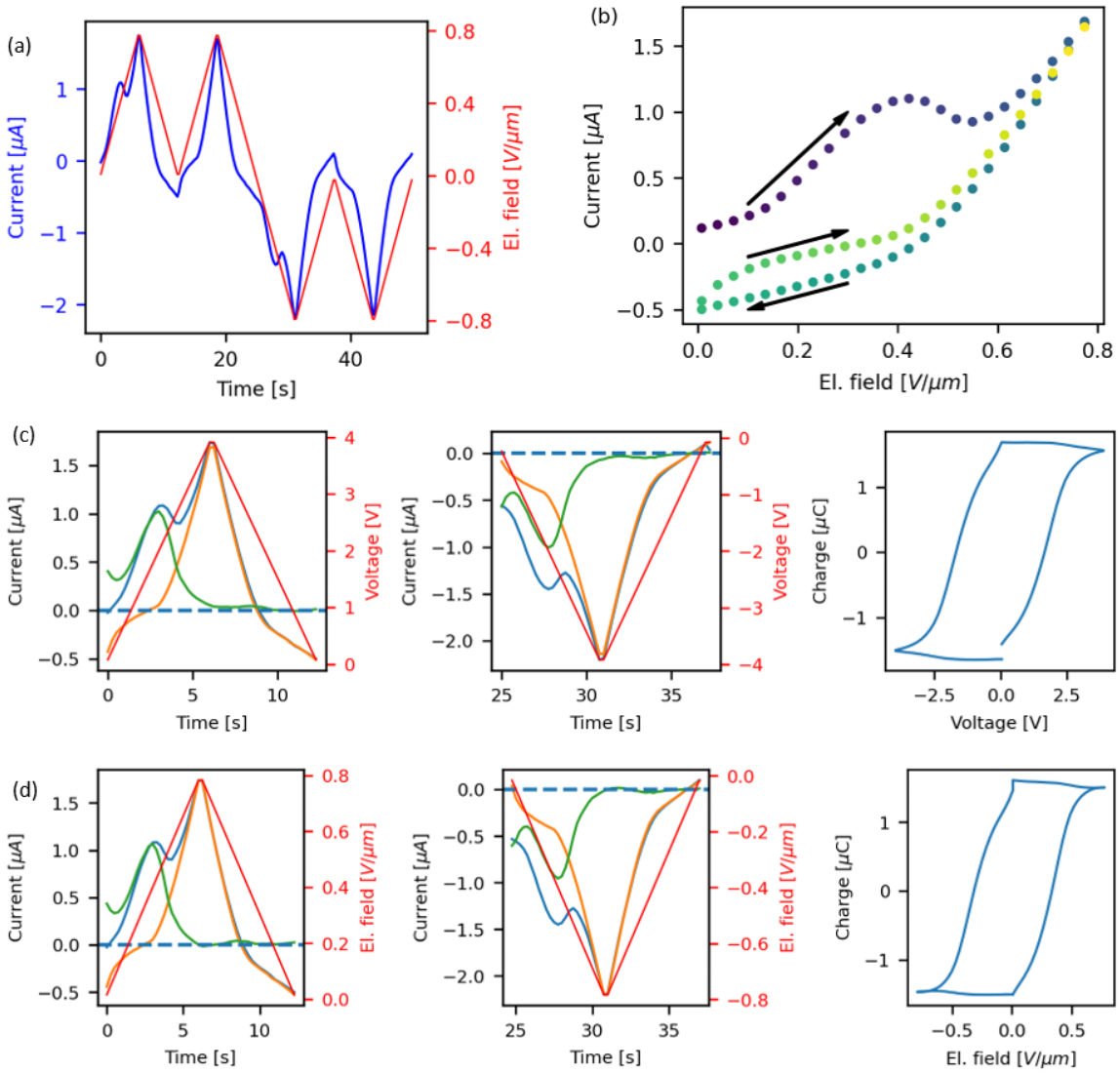

*Fig. 21: DW measurement of **material 1** (a) original measurement; (b) Current as a function of voltage, (c) DW evaluation with raw data, d) DW evaluation with rescaled values. As (c) shows the raw data, the voltage is shown, while for (d), the voltage is converted to the electric field (chapter III.A.2); the blue curve shows the current in the first voltage pulse, the orange the current in the second voltage pulse and green the difference between the two. Red shows the applied voltage.*

The assumption that the difference between the first and second wave is purely ferroelectric hysteresis is, however, not necessarily true as there can also be other hysteretic contributions, like for example known from migration of ions [186]. Ionic hysteresis, however, does not saturate with voltage like ferroelectric hysteresis does. When looking at the signals in Fig. 21(a) one observes that there is one current peak around 1.5 V in the first wave that is not present in the second. This is not consistent with ionic hysteresis and therefore attributed to ferroelectric switching. However, the current at maximal voltage in the first wave is also

slightly higher than in the second. This is assumed to be the non-ferroelectric contribution (probably ionic) that should not be included in the ferroelectric hysteresis curve. To avoid including this charge for the ferroelectric charge, the current of the second wave is rescaled so that its matches the maximal current of the first wave.

The integrated curves often showed a minor asymmetry leading to open hysteresis curves. This is probably due to some asymmetry of the device, changes of the material over time, or due to the presence of trapped charges and not due to an intrinsic asymmetry in the underlying material. To achieve closed hysteresis loops with one remnant polarization, both sides of the hysteresis curves are rescaled to the mean of the remnant polarizations.

The rescaling of the currents and its effects on the hysteresis curves can be seen in Fig. 21(c)/(d). Unfortunately, the currents of the first and second curve do not align well for low voltages as shown in Fig. 21 (b). This results in the sharp edges of the hysteresis curve and is explained in more detail in Appendix E.

The hysteresis curves of **material 4** were measured with a different (the custom-built) setup featuring a current detector with lower resolution. For this reason, the current was smoothed before applying the previously described steps. The raw and final data can be seen in Fig. 22.

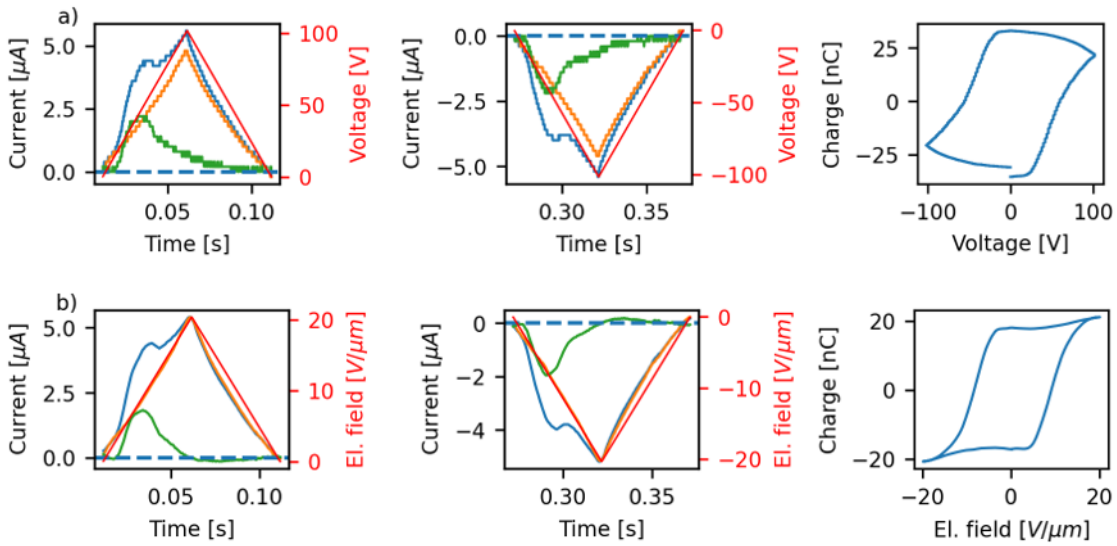

*Fig. 22: (a) Raw data for **material 4**, measured at 2 Hz,(b) data rescaled and smoothed, same color coding as Fig. 21 (c)/(d)*

2. CV rescaling

It was observed that the capacitance in most measured CV-loops decreases slightly over the course of the measurement. As there is no physical reason for any intrinsic asymmetry within the material and the decrease always happens over the measurement time, the consistent decrease implies a gradual evolution of the sample state, such as field-induced reordering, lowering the fraction of reversible switching or material degradation.

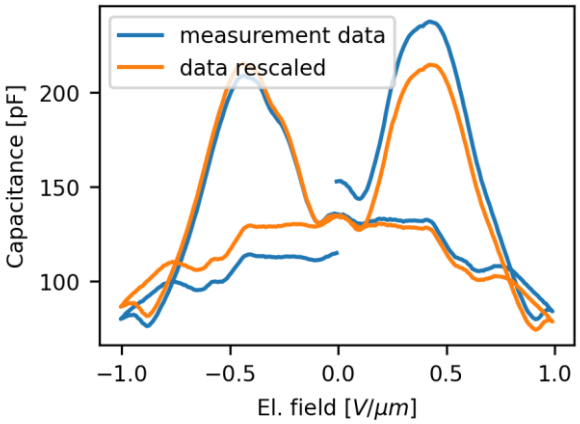

*Fig. 23 CV measurement for **material 1**, raw data in orange, blue shows the rescaled data*

To compensate for this, the curves are rescaled according to the following procedure: The first, last and middle data points all correspond to a voltage of 0 V. The capacitance at these points is averaged (mean 0 V). Each datapoint is then rescaled by a factor that linearly changes from the factor that rescales the first datapoint, to the one rescaling the middle datapoint, to rescaling the last datapoint. The effect can be seen in Fig. 23.

3. Negative control

As a negative control, the co-crystal of 2,3,5,6-tetrafluorobenzene-1,4-diol and pyrazine [187] was measured. It crystallizes in the triclinic, centrosymmetric $P\bar{1}$ spacegroup (CSD refcode QUWZEO) and can therefore not be ferroelectric. It was chosen as a negative control which gets processed and measured like all the other used compounds to ensure that the setup does not accidentally produce false positive results.

As expected, the DW measurement (Fig. 24(a)) does not show a second peak in the current and the CV-loop (Fig. 24(b)) is flat. This shows that the setup or any production steps does not produce ferroelectric-like results with non-ferroelectric materials.

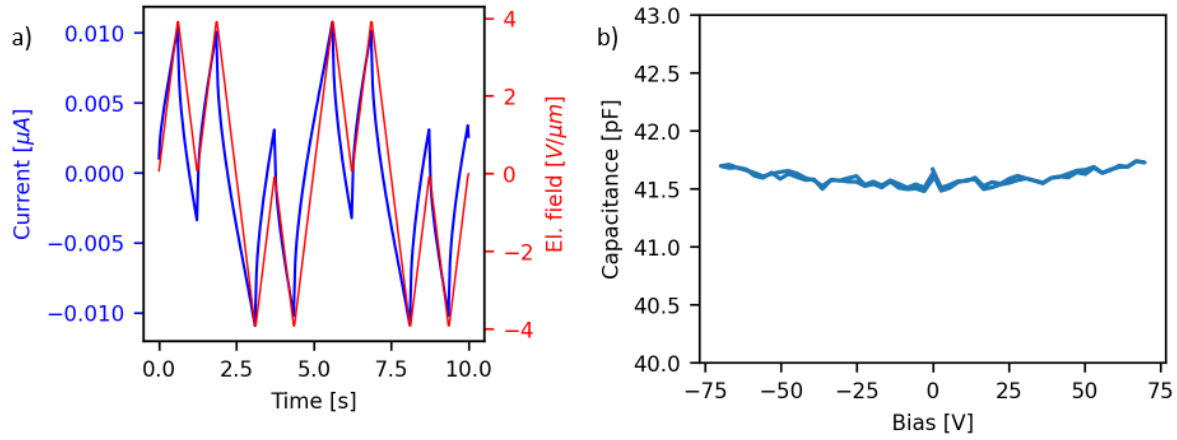

Fig. 24: a) DW and b) CV measurement of QUWZEO at RT

IV. Results Database mining study

This chapter is based on the author's database screening study [2] and is extended by additional measurements, especially PFM images, conducted for this thesis.

As detailed in the introduction of this thesis, ferroelectric materials are used in a wide array of applications, with their piezoelectricity being the most important property. While conventional ferroelectrics are mostly inorganic, organic ferroelectrics offer the prospect of non-toxicity, easy processability and high tunablity, which can enable a broader range of applications. To make best use of their tunability, good structure-property relations are needed. While the switching mechanisms and kinetics of inorganic ferroelectrics are generally well understood, the same cannot be said for organic ferroelectrics. A way forward in gaining a better understanding of the variety of mechanisms underlying the ferroelectric properties of organic ferroelectrics is to expand the catalogue of known organic ferroelectrics. Not only is this important to establish structure-property relationships, which are currently largely lacking for organic ferroelectrics, but also for identifying their performance limits.

To achieve this, the Cambridge Structural Database (CSD) is a useful resource was already demonstrated over 30 years ago in a study of 186 materials [188]. With the use of today's computing power, it is possible to screen large portions of the 1.2 million entries according to different criteria depending on the class of ferroelectric being searched for. This approach led to the identification of 54 globular [67] and 12 proton-transfer [68] candidate materials. Here, we assess the validity and relevance of this data mining approach by experimentally investigating whether (a subset of) these materials are indeed ferroelectric with the goal to also find new ferroelectric materials which have properties that are suitable for applications or yield new insights in previously unknown ferroelectric phenomena and produce experimental results upon which a refinement of the screening process can be built upon.

From the various ferroelectric candidate materials predicted in Refs. [67] and [68], four compounds were selected for this work: hexamethylenetetramine hydrogen DL-malate (CSD refcode TOZTAF, from here on called **material 1**), hexamethylenetetramine ammonium tetrafluoroborate (HMTAAB, **material 2**), trimethylamine-borane (ZZZVPE02, **material 3**) and 6-hydroxy-4(3H)-pyrimidone (UHUMEP01, **material 4**) mainly because of their high predicted polarization values (>10 µC/cm^2 for **material 1-3**), ease of synthesis (**material 3** and **4** are commercially available), availability of the precursors, and their low-toxicity. All molecule structures are depicted in Fig. 25.

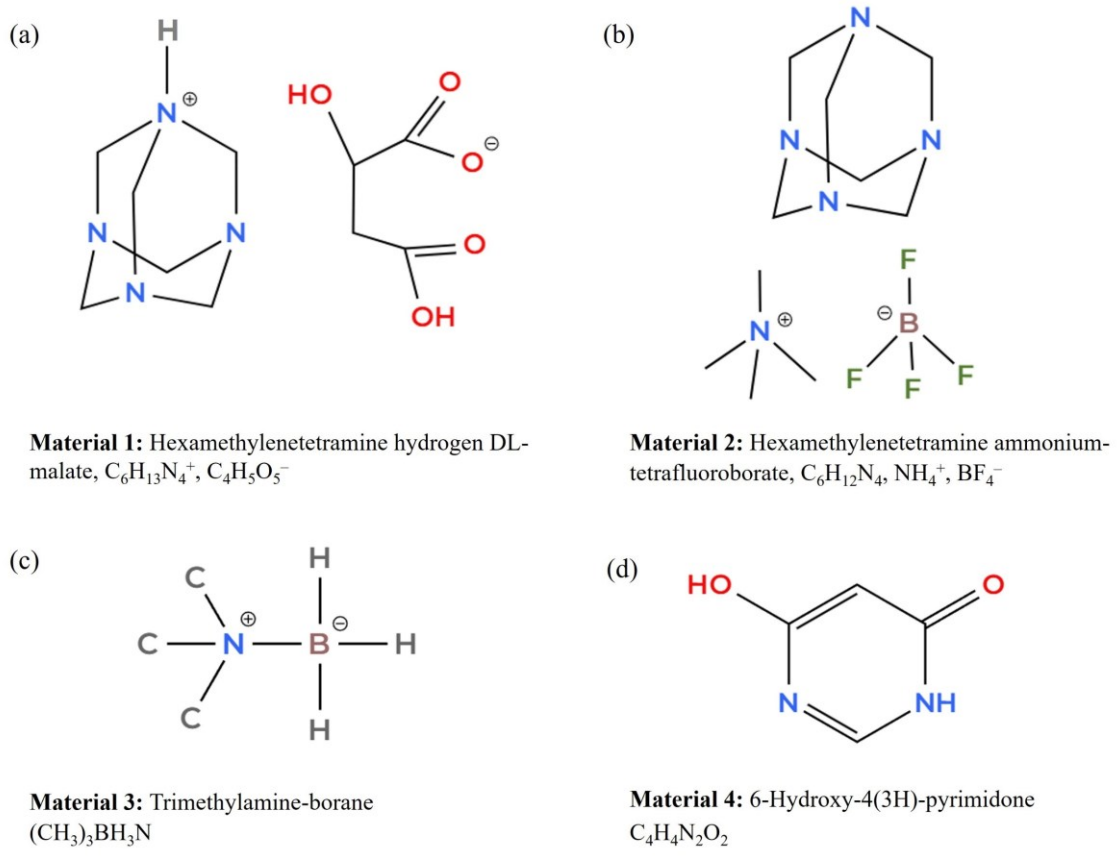

Material 1: Hexamethylenetetramine hydrogen DL-malate, $C_6H_{13}N_4^+$, $C_4H_5O_5^-$

Material 2: Hexamethylenetetramine ammonium-tetrafluoroborate, $C_6H_{12}N_4$, NH_4^+, BF_4^-

Material 3: Trimethylamine-borane $(CH_3)_3BH_3N$

Material 4: 6-Hydroxy-4(3H)-pyrimidone $C_4H_4N_2O_2$

*Fig. 25 Molecular structures of **material 1-4** along with their molecular formulas.*

Co-crystals of hexamethylene tetramine and DL-malic acid, **material 1**, were synthesized by mixing equimolar mixtures of the precursors (99.0% assay, Sigma Aldrich) as described by Chandrasekhar et al.[189]. The resulting complex was recrystallized in ethanol and used for various characterizations.

Hexamethylenetetramine ammonium tetrafluoroborate, **material 2**, was synthesized by mixing equimolar ratios of hexamethylene tetramine (99.0% assay, Sigma Aldrich) and NH_4BF_4 (99.0% assay, Sigma Aldrich) in water as a solvent. The minimum amount of solvent was used to dissolve the compounds, after which the solution was allowed to evaporate slowly. This synthesis method is reported here for the first time. The compound was recrystallized using ethanol as solvent.

Trimethylamineborane, **material 3**, (97% assay) and 6-hydroxy-4(3H)-pyrimidone, **material 4**, (98% assay) were directly purchased from Sigma Aldrich and recrystallized from ethanol and water, respectively. For **material 4**, recrystallisation was done under dark conditions, as the compound forms a dimer when recrystallized under sunlight [190]. Fig. 25 summarizes the four compounds studied in this work, along with their CSD reference codes and Corresponding molecular formulas.

To put the results in context, we start with a brief overview of the structural properties of the four mainly investigated compounds:

Material 1 and **2** crystals have ionic molecular structures and belong to the group of hexamine-based compounds. **Material 1** has a monoclinic *Cc* crystal structure at room temperature. Its constituent molecules have several intermolecular hydrogen bonds stabilizing the crystal lattice. The protonated nitrogen makes hydrogen bonds with the carboxylate group of DL maleate. Additionally, the different hydrogen bond lengths for donor and acceptor molecules indicate a possible proton transfer in this system [189]. The calculated polarization is 17.3 μC/cm^2 [67].

Material 2 has a polar hexagonal *P*6$_3$*mc* space group with a perovskite-like structure [191] and no hydrogen bonds. Its polarization is predicted at 11.6 μC/cm^2 [67] and can be inverted with the displacement of the positive with respect to the negative ionic molecules. The only other reported hexamethylene-based supposedly ferroelectric system is the hexamethylenetetramine-bisnopinic acid co-crystal. XRD and SHG on this compound indicate a polar space group, the $P(E)$ curve, however, does not saturate and shows a very small polarization of P_r ≈ 0.22 μC/cm^2, indicating that it either results from incomplete switching or does not reflect ferroelectric behavior at all [192].

Material 3 has a rhombohedral polar *R*3*m* space group [193], [194] at room temperature. In the database study [67], only the low temperature phase of this compound (CSD ref code ZZZVPE02, structure reported at 150 K) has been identified as a potential ferroelectric. However, since the reported polar *R3m* phase is retained even at room temperature (CSD ref.code ZZZVPE, no atomic coordinates published, thus omitted from the data mining study), we have investigated this compound under ambient conditions. (Trimethylamine)-borane has been reported in the literature as a plastic crystal with rotational disorder contributing to its metal-like high ductility, malleability and 3D plasticity [195]. These properties of **material 3** can potentially be utilized in flexible and/or wearable ferroelectric devices. It has also showed SHG, piezoelectricity and pyroelectricity, but there is no clear proof of ferroelectric switching as the $P(E)$ loops did not saturate and the PFM spectra do not conclusively rule out an interpretation in terms of (non-ferroelectric) electrostatics [196]. However, the limited thermal stability of **material 3**, see below, seems to be an issue for both characterization and practical applications. Its polarization is predicted at 17.2 μC/cm^2 and the structure can be inverted with the rotation of the molecule.

The compound 6-Hydroxy-4(3H)-pyrimidone, **material 4**, an analogue of the RNA nucleobase uracil (2,4-dihydroxypyrimidine), has two monoclinic polymorphs at room temperature: a *Cc* α-form (CSD refcode UHUMEP01) and a *P*2$_1$ β-form (CSD refcode UHUMEP) [197]. Only the former has been predicted to show ferroelectricity based on a proton transfer mechanism [68]. The fact that it can show different polymorphs, of which only UHUMEP01 exhibits the neutral lactam-lactim tautomerization that enables an interconnected proton transfer path [197], makes it potentially difficult to reach the desired proton-transfer configuration. Its polarization is predicted at 4.41 μC/cm2.

Material 5, Triethylenediamine dihydrochloride ($Pna2_1$ space group [198]; refcode VAGVAA), was initially also supposed to be part of this study. Unfortunately, we were unable to synthesize it properly and a different material emerged, which is currently under investigation by Manjunath Balagopalan. While initial ferroelectric measurements were promising, it is not entirely clear to which structure they correspond, which is why the results are only briefly reported in Appendix I.

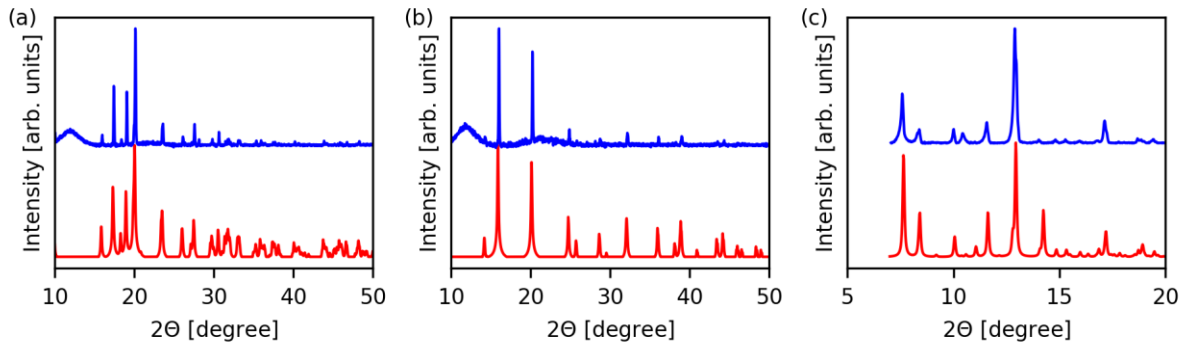

*Fig. 26: Measured (blue) powder X-ray diffraction patterns of (a) **material 1**, (b) **material 2** and (c) **material 4 samples** along with their simulated patterns (red) obtained from the CSD data base. The hump around 2Θ = 12° in a) and b) arises from the glass sample holder.*

Fig. 26 shows the experimental PXRD patterns of **material 1, 2** and **4** along with their simulated patterns calculated from the cif files from their CSD entries. The recrystallized borane complex **material 3** was found to be volatile at room temperature, preventing structural characterization. For the other three compounds, the diffraction peak positions and relative intensities in the simulated patterns agree well with the experimental data. No additional peaks were observed, confirming successful phase formation and absence of any secondary phases. The phase purity in **material 2** supports the reliability of the newly developed synthesis method. Slight discrepancies in relative peak heights for **material 4** are attributed to a preferred orientation of the material, no new peaks were observed in this case either.

After having confirmed their structure with PXRD, the materials were firstly investigated with dielectric spectroscopy to detect phase transitions and, consequently, relevant temperature ranges. As none of the measurements (shown and briefly discussed in Appendix C) showed any signs of Curie-Weiß behavior or other relevant phase transition[17], all measurements were performed at room temperature. The materials were investigated with the double wave measurement method to obtain a background corrected hysteresis loop and capacitance-voltage loops. The data was evaluated as described in chapter III.C. The raw data for all measurements can be found in Appendix 5-Appendix 14.

[17] **Material 1** showed variations depending on the atmosphere, which turned out to be very relevant for the understanding of this material.

A. Material 1 (TOZTAF)

The first tested compound is the co-crystalline **material 1**. When applying the double wave form (Fig. 27 (a)) to the material, there is a double current peak in response to the first voltage wave, whereas only a single peak (coinciding with the voltage peak) is present in the second wave. For a ferroelectric material, the first double peak includes, apart from any background currents, the charge that is needed to compensate for the change of polarization. When applying the second pulse, the polarization is already switched, so there is no polarization reversal contribution, hence the first peak disappears. Taking the difference between the responses to the first and second waves and integrating gives the polarization (represented by the charge) hysteresis curves that are shown for different frequencies in (Fig. 27(b)). For the faster measurements (as well as the curve later shown for **material 2**), there is an edge at 0 V. This is an artifact of the waveform and is explained in more detail in Appendix E. The charge saturates for each loop, which is necessary for a ferroelectric [77], and the coercive field sits around 0.35-0.45 V/µm.

The charge associated with ferroelectric switching is determined by crystal geometry and should therefore, contrary to the present data, not depend on the measurement frequency. For this, there might be several reasons. It is well known that the coercive field is frequency-dependent [199], thus at higher frequency not all dipoles might be switched. The data however shows a distinct first peak and a saturating hysteresis curve, ruling out this possibility.

Alternatively, in many materials there exists a finite ionic conductivity that can give rise to hysteresis [186]. It should predominantly be present in the first pulse of the double wave and should not saturate with increasing field. Hence, ionic currents do give rise to open $P(E)$ loops with increasing 'remnant polarization', but not to any current peaks, as observed here. Hence, ionic contributions to the hysteresis might be present, but can be ruled out as the main source of it. In the evaluation, as detailed in chapter III.C.1, the current of the second peak is rescaled to match the first peak, ideally compensating for ionic hysteresis in the absolute polarization values. Nevertheless, signs of ionic hysteresis can still be seen in the 250 mHz hysteresis curve (Appendix 7), where the accumulated charge in the hysteresis curve still increases on the decreasing side of the electric field sweep.

On top of (minor) ionic contributions, the material also shows significant background conductivity. The ohmic conductivity in (Fig. 27(a)) can clearly be attributed to the material, as the empty IDE has negligible leakage (see Appendix 2). The evaluation method compensates for the first order background conductivity with the assumption that the background conductivity only depends on the bias [162]. In ferroelectrics, the background conductivity depends on the injection barrier and the bulk conductivity that both may depend on polarization [200]. Specifically, the injection barrier can be altered by a change in surface charge density due to polarization switching [146], [200] which can lead to a switch from an injection-limited to a space charge limited regime [200]. The bulk conductivity can also directly depend on the polarization state due to a nonlinear coupling between scattering and polarization [109], [110]. In all these cases, the background conductivity below the coercive field cannot properly be compensated for by the DWM. This results in the current peak having contributions from polarization reversal, ionic hysteresis and background conductivity. For lower frequencies, the background conductivity gets integrated over the longer measurement time, leading to higher measured charges.

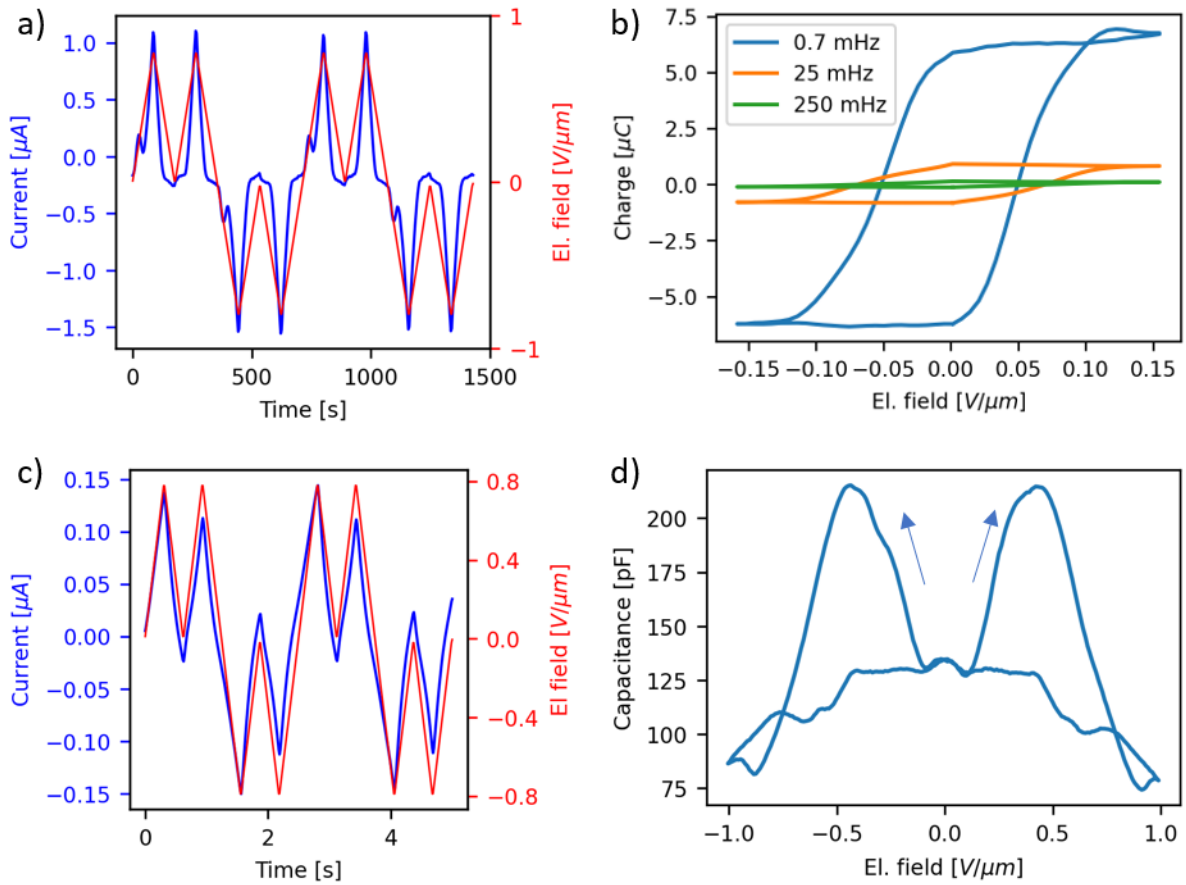

*Fig. 27: (a) Double wave signal of **material 1** at ambient conditions with 42%rh; (b) Calculated hysteresis curve for different frequencies; (c) Double wave signal of **material 1** at ambient conditions with 19%rh; (d) Capacitance-voltage curve of **material 1** with 39%rh*

Consequently, the fastest feasible measurements at 0.25 Hz is the best estimate for an upper limit of the polarization. The measurement results in a charge of 0.11 ± 0.01 µC, which can be converted into an upper limit for the polarization of 54 ± 20 µC/cm^2 (compare with chapter

III.A.2, III.C.1 and Appendix 7 for details). This finding is consistent with the predicted remnant polarization of 17.3 µC/cm^2 [67]. Measurements of the CV-loop (Fig. 27(d)) show the butterfly shape that is typical for ferroelectrics [201]. There is a broad peak around 0.3 - 0.5 V/µm showing good agreement with the coercive field from the hysteresis curve.

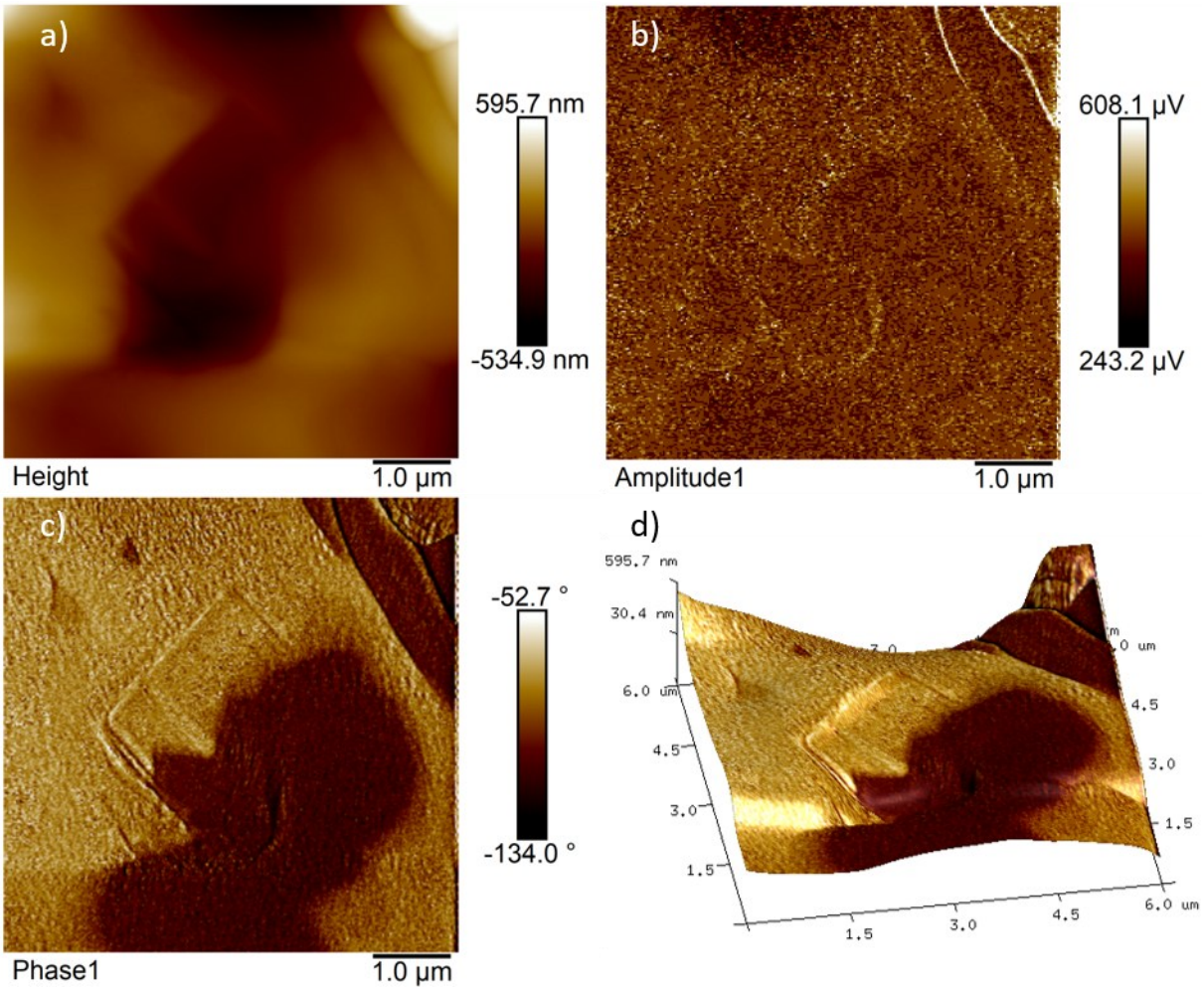

Fig. 28: PFM measurements of material 1; (a) height; (b) PFM amplitude and (c) PFM phase channel; (d) Height-3d image with PFM phase color coding (data from (a) and (c))

Piezoelectric characterization of **material 1** was attempted using PFM (method described in chapter II.H). Unfortunately, it was not possible to pole the material with the available voltage of ± 10 V (resulting 20 V between sample and cantilever in total). The reason is that it was only possible to produce thin (≈1-2 µm) films or thick (≈80-100 µm) crystals. The thin films need switching voltages below 1 V which is lower than the small signal used for measurement and the thick crystals need voltages between 30 and 50 V.

However, the piezoelectric signal of the unpoled, thick crystal was successfully measured (Fig. 28). The surface (Fig. 28 (a)) is rough with height differences up to one micron. There is also a rectangle rotated by 45° visible, corresponding to a prior poling attempt. The amplitude (Fig. 28 (b)) is somewhat noisy and does not yield much information. In contrast, the phase (Fig. 28 (c)) shows regions with two different, constant phases. This is consistent with two different ferroelectric domains. Their phase does not change by 180° as there is a constant background

added onto the piezoelectric signal. As shown in the overlay of height and phase (Fig. 28(d)), the phase change in the central region does not correlate with any topographic change or the poling region. In the top right corner, the phase change occurs at the grain boundary, which is often seen for ferroelectric domains [202]. While this measurement does not prove ferroelectricity itself, it shows strong evidence for piezoelectricity in the material further supporting the evidence for ferroelectricity.

Material 1 is quite stable, with samples working for several months, and well-reproducible under the same conditions. There is, however, a strong dependency on the ambient humidity. At low humidity conditions (as can be encountered in winter) all signs of ferroelectric switching disappear (Fig. 27(c)) and also the background conductivity currents become much smaller, suggesting an interconnectedness.

In summary, **material 1** shows conclusive evidence for ferroelectricity under ambient conditions. The low frequencies that are needed to enable full polarization reversal hint at a more complex mechanism for inversion of the unit cell than mere proton or ion motion, as was anticipated on basis of the complex unit cell. The strong dependence of the ferroelectric and electronic behavior on humidity inspire further investigation of, e.g., the detailed switching mechanism and the role of proton transfer therein and is topic of ongoing investigation.

B. Material 2 (HMTAAB)

The second compound tested was **material 2**. The double wave measurement (Fig. 29(a)) shows a current peak that is only present in the first wave, which is a good sign of ferroelectricity, as well as significant background conductivity. Consequently, the hysteresis curve (Fig. 29(b)) saturates, which is a prerequisite for ferroelectricity. The integrated charge at the maximum voltage accumulates to 2.4 µC, which would correspond to an unreasonable saturation polarization of 1200 ± 400 µC/cm^2 (the predicted polarization is 11.6 µC/cm^2 [67]). As for **material 1**, this can be explained by a dependence of the conductivity on polarization, and specifically by the conductivity before switching being increased. For this reason, the integrated charge is the sum of the true polarization charge and the integrated difference in background conductivity current.

After the maximum field, the charge slightly increases to 2.8 µC at zero field. This can be explained by incomplete background conductivity compensation, as the current of the first peak is always slightly above the current from the second peak (Appendix 10) in combination with a minor contribution from ionic hysteresis. The coercive field is ≈ 0.4 V/µm. The CV-loop (Fig. 29(c)) shows the characteristic butterfly shape with a peak at ≈ 0.4 - 0.5 V/µm, indicating good agreement between the two measurements for the coercive fields and confirming the ferroelectric nature of the compound.

When drop-casting the material from aqueous solution, the ferroelectric measurements can reliably be reproduced. Unfortunately, the samples degrade rather quickly and the signal becomes worse with every consecutive measurement. When drop-casting the material from

ethanol solution, all signs of ferroelectricity disappear, and the background conductivity current also decreases by three orders of magnitude (Fig. 29(d)), suggesting a direct or indirect coupling between the ferroelectricity and background conductivity. It could however not be determined whether structural changes arising from different crystallization kinetics are the cause, which is why this observation should not be overinterpreted.

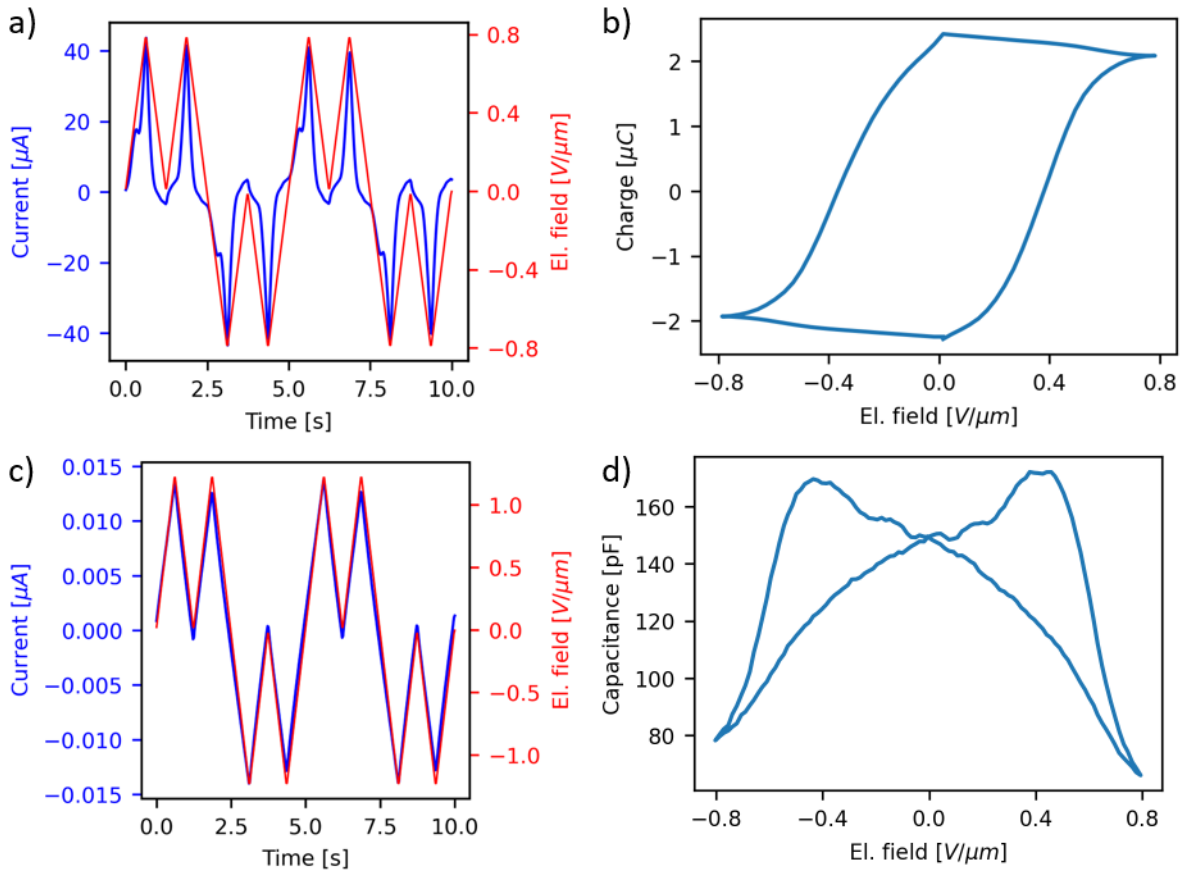

Fig. 29: (a) Double wave signal of material 2, fabricated with water as solvent; (b) Hysteresis curve calculated from (a), detailed evaluation in Appendix 10; (c) Double wave signal of material 2, fabricated with EtOH as solvent; (d) Capacitance-voltage curve of material 2 (from water).

In summary, there is conclusive evidence that **material 2** is ferroelectric. While the ferroelectric properties are not remarkable, the potential coupling to background conductivity are yet to be understood and general topic of ongoing investigation [4], [109], [146]. Due to its fast degradation, the material does not seem very promising for applications.

C. Material 3 (ZZZVPE)

Measurements using the known piezo- and pyroelectric **material 3** proved more challenging than those with the previously mentioned materials. These difficulties arise from the material's tendency to sublimate quickly at ambient conditions. For this reason, all experiments had to be performed immediately after device fabrication. The double wave measurements of one device (Fig. 30(a)) depict very sharp current peaks that are only present in the first wave. The presence in the first wave and the absence in the second is usually good evidence for ferroelectricity. In this case, the peaks are, however, unusually narrow and have

varying heights; they nonetheless consistently appear at a well-defined (possible) coercive field of 13.3 ± 0.5 V/µm. Combined, this leads to the irregular shape of the hysteresis curve in Fig. 30(b), where the apparent change of polarization is different for both directions and the change in polarization is very steep. In principle, the sharpness might be indicative of fast switching in a low-disorder, i.e. close to intrinsic, sample. However, due to the problematic (in)stability of the material, discussed further below, it was not possible to investigate this further.

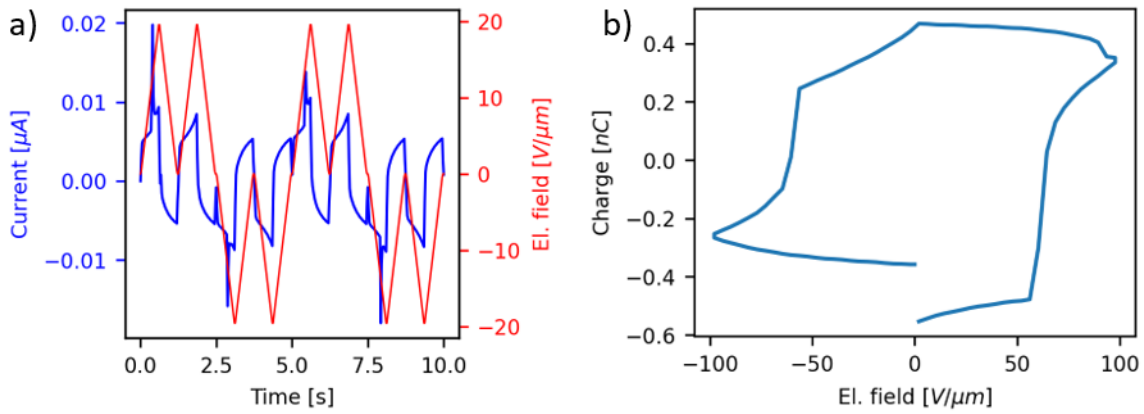

*Fig. 30: (a) Double wave signal of **material 3** at ambient conditions; (b) The calculated hysteresis curve from (a). The current peaks after each 2nd wave are due to the short plateau in the driving voltage signal and do not reflect any form of switching or shorting.*

One further noteworthy feature of the DWM signals in Fig. 30(a) is the fact that the conductivity after the polarization reversal event in the first wave is increased. This is opposite to what occurs in **material 2** and, to a lesser degree, in **material 1**. In principle, such behavior could result from the modulation of a charge injection barrier by the orientation of the interfacial dipoles, giving rise to easier charge injection when polarization and field are parallel[109], [146]. The increased current is not compensated for by the evaluation method [162], leading to the linear increase of charge in the $P(E)$-loop above the (possible) coercive field.

What speaks against this interpretation is that the low voltage conductivity is at the same level in both waves. In an injection barrier modulation scenario, the interfacial dipoles should, when still aligned, continue to allow enhanced injection. In absence of secondary peaks indicating full polarization loss between the two waves, one might tentatively attribute the odd conductivity behavior to the interfacial, but not the bulk polarization being quickly lost.

The charge at maximum voltage is $3.5*10^{-4}$ µC. As the material sublimates very quickly, it is difficult to determine the exact film structure. The, in this case unreasonable, assumption of a thick (> 500 nm), continuous film would result in a very low polarization (0.09 µC/cm^2 compared to the predicted 17.2 µC/cm^2 [67]). CV-measurements of the same sample (Appendix 13(a)) did not show the typical butterfly shape. Measurements of other samples occasionally showed peaks in the first wave (Appendix 13 (b)), but any reliable appearance could not be achieved. This poor reproducibility can be attributed to the quick sublimation of the material, which makes every experiment difficult.

In summary, the results presented here are by themselves inconclusive. While the appearance of peaks in the DWM generally suggests ferroelectricity, the unusual peak shape and the absence of butterfly like CV-loop casts doubt on this interpretation. Nevertheless, as the material has already been shown to exhibit SHG, piezoelectricity and pyroelectricity [196], we believe that the here shown measurements are sufficient to at least suggest ferroelectricity in the material. Given the challenges associated with handling this material, future efforts should focus on identifying more suitable conditions for working with it.

D. Material 4 (UHUMEP)

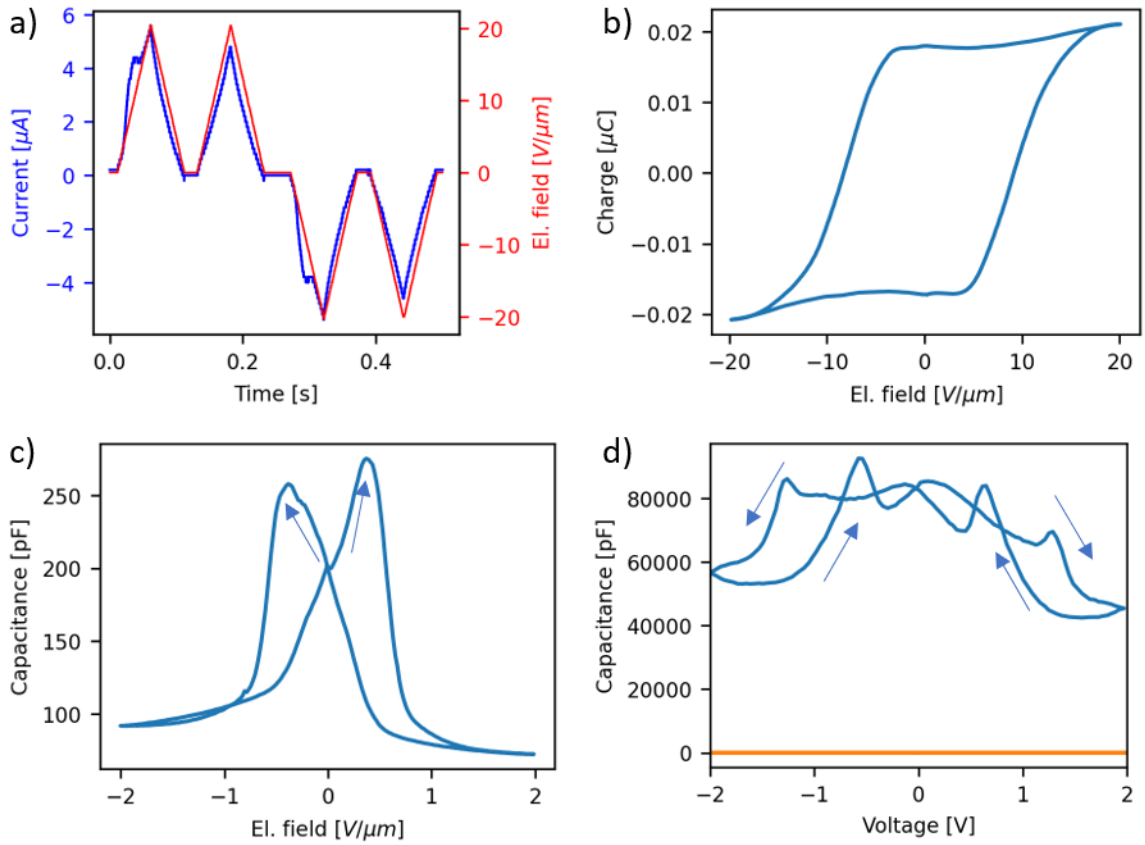

*Fig. 31: (a) Double wave signal of **material 4** at ambient conditions, (b) The calculated hysteresis curve from (a); (c) Representative capacitance-voltage curve of material 4 at ambient conditions (d) Capacitance-voltage curves of two different selected samples from the same batch as (c)*

The last substance investigated was the proton-transfer **material 4**. The double wave measurement (Fig. 31(a)) reproducibly shows additional current shoulders in the first voltage wave that do not show up in the second. This results in a saturating hysteresis curve (Fig. 31(b)) with a coercive field of 8 V/µm and a remnant charge of $2.1*10^{-2}$ µC resulting in a remnant polarization of 4.2 ± 1.4 µC/cm^2 for a DWM cycle frequency of 2 Hz. A possible effect of conductivity switching is suppressed by the comparably high measurement speed. On the basis of the calculated energy barrier for proton transfer, the coercive field for a 5 Hz (equivalent to 2.5 Hz in DWM) measurement was estimated to be around 1.3 V/µm [68]. It is worth underlining that predictions of proton-transfer barrier are highly method dependent

[203]. This means that the measured coercive field is similar to but higher than expected. The estimated remnant polarization from the hysteresis loop is surprisingly close to the predicted value of 4.41µC/cm^2 [68], given that many of the used parameters are only rough estimates.

The CV-loop (Fig. 31(c)) shows the typical butterfly-shape with a peak at 0.6 V/µm. The difference between the different coercive fields can be explained by the measurement frequency, which is 2 Hz for the double wave measurement and 0.004 Hz for the CV-measurement.

While the above-presented behavior was seen for many different samples, some samples behaved differently, as can be expected for a material with multiple polymorphs and tautomers [190], [197], of which only one polymorph was predicted to be ferroelectric. The dimeric form is easily identifiable as it forms long needles[190]. An optical microscopy image of this sample (Fig. 32(a)) as well as another sample with similar electric characteristics (Fig. 32(b)) shows (almost) no needles, indicating that the dimeric form is only present in small amounts.

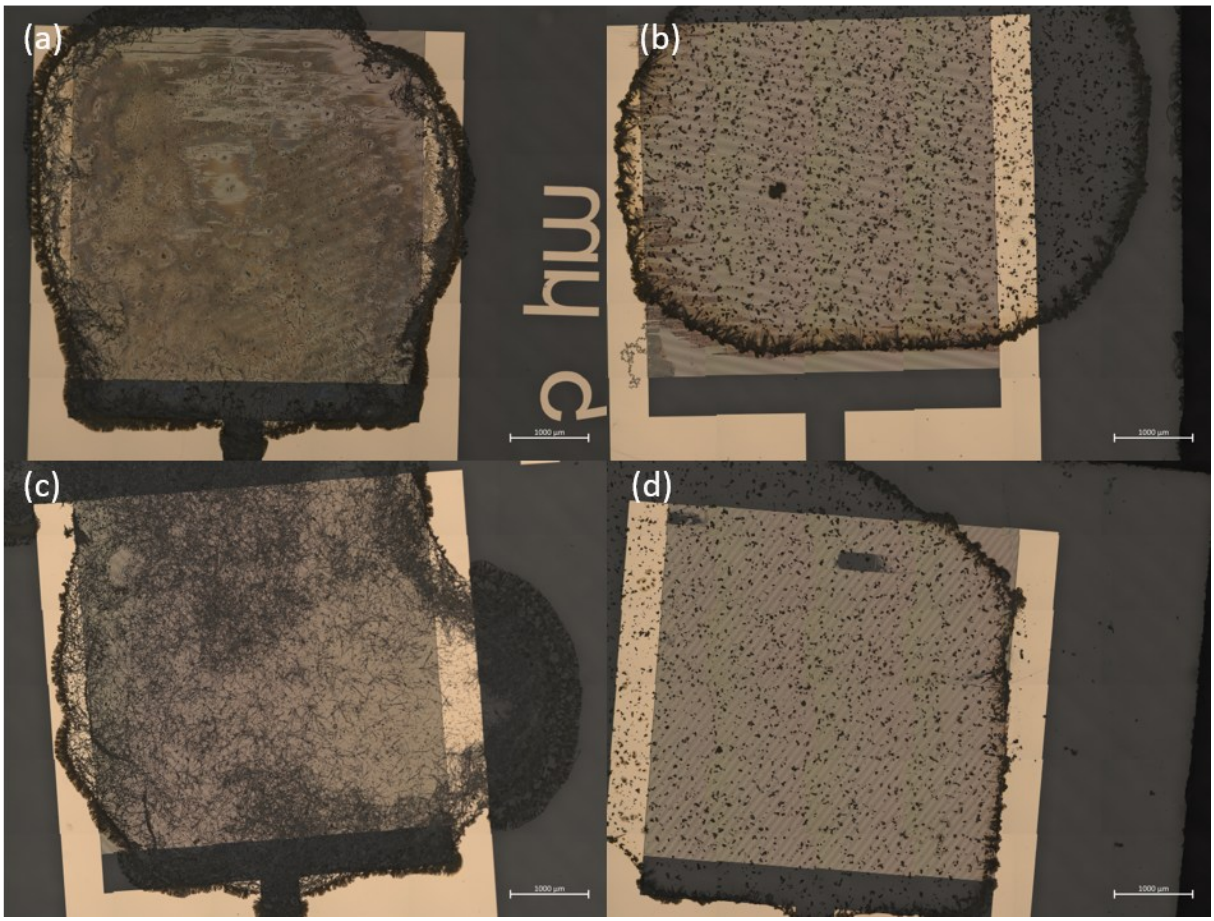

*Fig. 32: Opt. Microscope images of samples of **material 4**: (a) the working sample used in Fig. 31(a-c); (b) another working sample not shown in this work, (c)sample with flat capacitance in Fig. 31(d); (d) sample with interesting capacitance in Fig. 31(d)*

This polymorphism was, amongst others, reflected in some samples being completely inactive, as indicated by the orange curve in Fig. 31(d). Here, the material only consisted of needles

(Fig. 32(c)), indicating that the dimeric form is electrically inactive. In stark contrast, another sample showed a very high permittivity and a capacitance peak at ~0.3 V/µm when increasing the electric field and another peak at a lower field of ~0.1 V/µm when decreasing the field, as shown by the blue line in Fig. 31(d). This behavior resembles the CV-loop of an anti-ferroelectric [204]. The corresponding double wave measurement (Appendix 14(a)), however, never showed the currents that are associated with an antiferroelectric [162], so the nature of this phenomenon remains somewhat unclear. Optical microscopy (Fig. 32(d)) showed that the dimeric form is not present in this sample. As X-ray diffraction is not able to resolve hydrogen-atoms, it was not possible to determine the tautomeric state of the deviating samples.

In summary, we are convinced that at least one of the polymorphs of **material 4** is a well-behaved ferroelectric, while potentially one or more of the other polymorphs might also show interesting or at least different behavior. At the same time, the limited reproducibility associated with the existence of different polymorphs makes systematic work on this material challenging. To properly understand its ferroelectric properties, it is first necessary to establish reliable methods for achieving the desired state. However, this lies beyond the scope of the present exploratory study.

E. Summary and outlook

We experimentally investigated four materials that were predicted to be ferroelectric in a database mining approach. The dual aim was to assess the effectiveness of this method for discovering new organic ferroelectric compounds with interesting properties and to improve our understanding of structure-property-relationships in such systems.

Three out of four materials (**1,2** and **4**) showed strong evidence for ferroelectricity: Double wave measurements performed on them revealed clear polarization switching currents resulting in saturated hysteresis loops. The corresponding capacitance-voltage-curves exhibited the characteristic butterfly shape with coercive fields matching those of the hysteresis curve. The double wave measurement of **material 3** showed a strong, unusually sharp current peak in the first pulse, which could indicate ferroelectricity switching. However, this result could not be reproduced, and the CV-loop lacks the expected butterfly-shape, rendering the findings inconclusive.

Based on this success rate, it can be inferred that there are likely several dozen yet unconfirmed ferroelectric materials among the candidates proposed by the database mining, thereby validating the effectiveness of this approach.

Material 1 showed strong ferroelectric behavior and is expected to be stiffer than many other organics due to its crystalline structure. While this makes it in general attractive for use in actuators, its high background conductivity leads to considerable ohmic losses and the effect of humidity makes it potentially unreliable. While proper encapsulation could probably stabilize its properties, the high conductivity appears to be linked to the proton transfer that is associated with ferroelectric switching and can therefore most likely not be circumvented. Application as a humidity-sensitive or -tunable material, for example in sensors, seem to be more promising. For this, the material seems to be sufficiently stable. As for all materials, there were no tests on toxicity or biocompatibility conducted, but there are no reasons to expect that this should be a major hurdle.

Material 2 was shown to be ferroelectric, but its quick degradation and high background conductivity pose major challenges for applications of this material. Like **material 1**, **material 2** showed strong conductivity-ferroelectricity coupling. Its properties did however not depend on the ambient humidity, suggesting a different underlying mechanism than the protonic effects in **material 1** which will be described in the next chapter.

Material 3 had inconclusive results which, coupled with the material's volatility, substantially hinders its potential usefulness.

Material 4 showed promising properties, when successfully stabilized in the proper configuration. There was, however, also an electrically inactive dimer and it was very challenging to reliably achieve the ferroelectric configuration. Consequently, the potential of **material 4** cannot be fully assessed until further work on film fabrication and structural control is successfully conducted.

While there is only one possible switching mechanism for **material 2, 3** and **4**, the mechanism for **material 1** remains unclear due to the presence of multiple potentially possible pathways. Further investigation, particularly through humidity-dependent studies, will be shown in the next chapter to clarify the switching behavior and contribute to a deeper understanding of switching phenomena in more complex ferroelectric co-crystals.

Having shown that both of these hexamine-based materials (**material 1** and **2**) are ferroelectric and show additional, previously unknown coupling between ferroelectricity and humidity or background conductivity, a logical follow up would be to investigate comparable materials. The screening study suggested two other hexamine-based candidate materials. While 1,3,5-Triaza-9-phospha-adamantane (TAZPAD) is a single-compound material with small predicted polarization and therefore not really comparable to **material 1** and **2**, it also tends to sublimate at room temperature, which drastically reduces its usability. On the other hand, 1,3,5,7-Tetra-aza-adamantan-1-ium bromide (BOHNUH01) is also an ionic co-crystal with comparable predicted polarization and therefore promising to investigate for ferroelectricity and coupling between ferroelectricity, humidity and conductivity.

V. Detailed analysis TOZTAF

This chapter is an extended version of my paper reporting the details of **material 1** (TOZTAF) [3], which is soon to be submitted.

As seen in the previously discussed database study, **material 1**, hereafter labeled by its CSD refcode TOZTAF, has shown remarkable results. Even in non-optimized polycrystalline thin films, deposited by simple drop casting, we find well-developed ferroelectric behavior up to elevated temperatures exceeding 80 °C, with an estimated remnant polarization of $P_r \approx 15$ µC/cm^2. We find exceptionally low coercive fields, down to $E_c \approx 0.2$ V/µm, depending on measurement conditions. This would make this compound compatible with low-cost printed electronics, in which in-plane feature sizes of tens of µm would still yield coercive voltages of a few V. Parallel to the ferroelectric properties, we find ohmic and capacitive electronic conduction that strongly resemble those commonly found for proton conductors. Both the coercive field and the complex conductivity are tunable by temperature and, more strikingly, ambient humidity, which not only suggests a common mechanism but also potential application in functional, responsive, or tunable materials. Although the experimental results do not allow us to conclusively identify the exact switching mechanism, we propose a two-step mechanism, in which proton transfer and molecular rotations contribute to the inversion of the unit cell.

A. Ferroelectric characterization

The ferroelectricity of a compound can be proven by hysteresis loops and capacitance-voltage (CV)-curves as demonstrated in chapter IV. Fig. 33(a) shows the hysteresis curves measured at various frequencies under ambient conditions. Each curve exhibits the expected saturation of integrated charge above the coercive field, characteristic of ferroelectrics. Additionally, a, for ferroelectric compounds atypical, dependence of the remnant polarization on the measurement frequency can be observed. This scales approximately linearly with the measurement frequency (inset Fig. 33(a)) and is therefore attributed to a polarization-dependent modulation of conductivity, as reported for other ferroelectric materials [4], [109], [110], [146].

Additionally, the CV loop (Fig. 33(b)) exhibits the characteristic butterfly shape with peaks near the coercive field of approximately 0.35 V/µm. The dependence of the coercive field on frequency and temperature is shown in Fig. 33(c&d) and compared to the Ishibashi–Orihara model [126], the Du–Chen model [128], and the thermally activated nucleation-limited switching (TA-NLS) [131] model (Appendix J). The best agreement was found with the TA-NLS model, as plotted in Fig. 33(c&d). The minor discontinuity at ~60 °C might be indicative of a transition in the switching mechanism and is discussed in more detail further below. The critical switching volume extracted from the TA-NLS fit was ~1.1×10^3 nm³ for $T < 60$ °C and ~2.5×10^3 nm³ for $T > 60$ °C, and the corresponding energy barriers were estimated at ~0.6

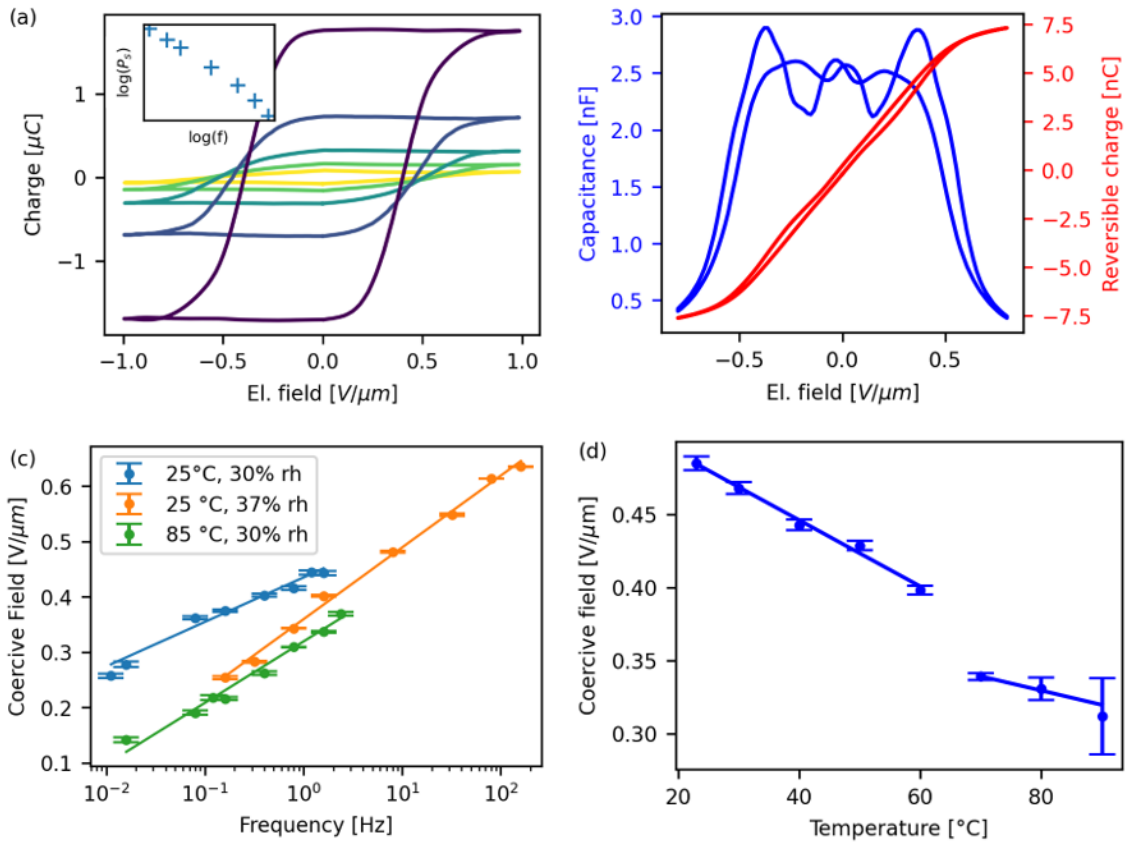

Fig. 33: (a) Polarization-hysteresis loops for double-wave frequencies between 100 mHz (yellow) and 10 Hz (dark purple), measured at 37% rh and RT; Inset: corresponding remnant charge vs. frequency; (b) CV-loop (blue) and its integration (red), measured at 35% rh and 30 °C; (c) Coercive field vs. frequency (1/risetime) at $T = 25$ °C (blue) and 85 °C (green), measured at 30% rh and at $T = 25$ °C , 37% rh (orange); (d) coercive field vs temperature measured at $f = 0.1$ Hz (1.6 Hz rise frequency) and 29% rh. Lines in (c) and (d) are fits with the TA-NLS-model, fit parameters and fits with other models are shown in the *Appendix J*. Error bars result from gaussian fits to the switching peak and therefore underestimate the total error.

eV and ~1.1 eV (see Appendix J). These values are comparable to those reported for PZT [23]. Notably, the switching volume is much larger than that of the ferroelectric liquid crystal BTA, while the energy barrier is of similar magnitude [24], consistent with the crystalline nature of the present compound. The integrated CV loop (Fig. 33(b), red curve) shows the reversible (small signal) polarization. This curve is nearly linear with only a small opening, indicating that it is dominated by the linear dielectric response. The x-axis intersections show the reversible, remnant charge to be around 0.16 nC, which is more than two orders of magnitude smaller than the total remnant charge obtained from the fit of the PE-loop (27.6 ± 9.7 nC, Fig. 33(a)). Together with the observation that the TA-NLS model describes the switching dynamics best, this strongly suggests that switching is nucleation-limited, followed by mostly irreversible domain wall motion.

Overall, the results confirm that TOZTAF behaves as a typical ferroelectric, albeit one that has an atypical polarization-dependent conductivity; the latter is discussed in greater detail below. Importantly, the combined features observed in both measurements are consistent with ferroelectric behavior and cannot be explained by other mechanisms. Together, these results

indicate a ferroelectric material that combines relatively high remnant polarization with a remarkably low coercive field.

B. Temperature and humidity dependence of conductivity and capacitance

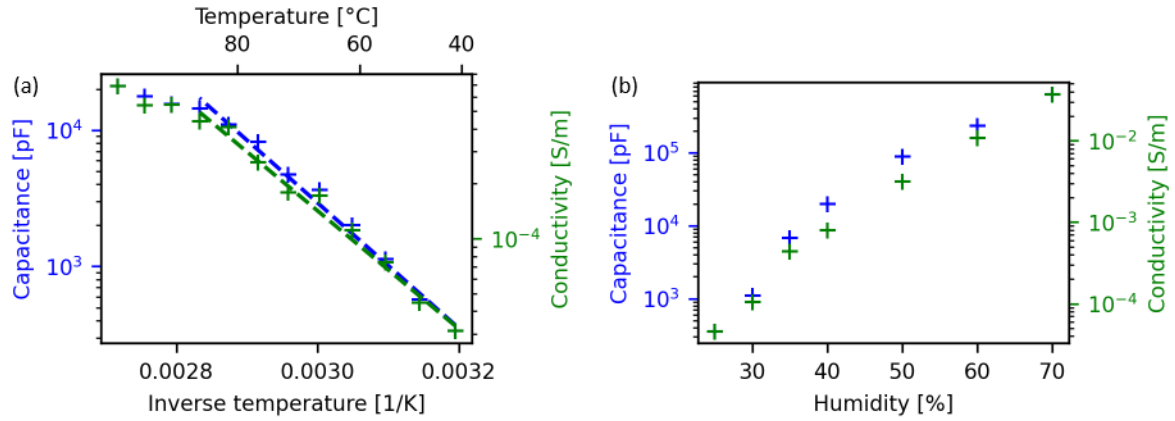

Fig. 34: Temperature (a, measured at 32% rh) and humidity (b, measured at RT) dependence of conductivity (green, right y-axis) and capacitance (blue, left y-axis); in a), the points above 85°C appear to be affected by material degradation.

The temperature-dependent capacitance and conductivity measured on nominally identical devices as used for the ferroelectric characterization above are shown in Fig. 34(a). Both show Arrhenius-like behavior with comparable activation energies of ~0.64 eV and ~0.91 eV, respectively. We tentatively attribute the lower value for the capacitance to the fact that the low-frequency conductivity requires charge carriers to percolate through the entire system, and hence they are forced to pass potentially higher barriers than charge carriers that are involved in the capacitive response. For the latter, charges may simply pile up near barriers, including the contacts, rather than having to overcome them. We also note that there are no apparent discontinuities around 60 °C.

Fig. 34(b) depicts the humidity-dependent capacitance and conductivity. Similar to their temperature dependency, both show a close-to-exponential correlation with humidity; the absolute changes upon increasing the humidity from 25 to 70% are approximately twice as large as when heating from 40 to 80°C (fit region). Such behavior is typical for hygroscopic materials [152] and can be explained by a changing proton mobility [156]. This indicates that protonic effects are the main source of resistive and capacitive charge transport with its main parameter, the proton mobility, being affected by temperature and humidity. Long term DC current measurements (Appendix K) show that the current stays constant over long periods, irrespective of the applied voltage. However, for voltages above ~2 V, the current significantly increases, which we interpret as an indication that the main conductivity channel involves a redox-reaction, most likely the electrolysis of water, happening at the electrodes.

This interpretation is confirmed by IV-measurements (Fig. 35) that show two regimes below and above ~2 V (0.4 V/µm). As expected for a redox reaction, this voltage does not depend on

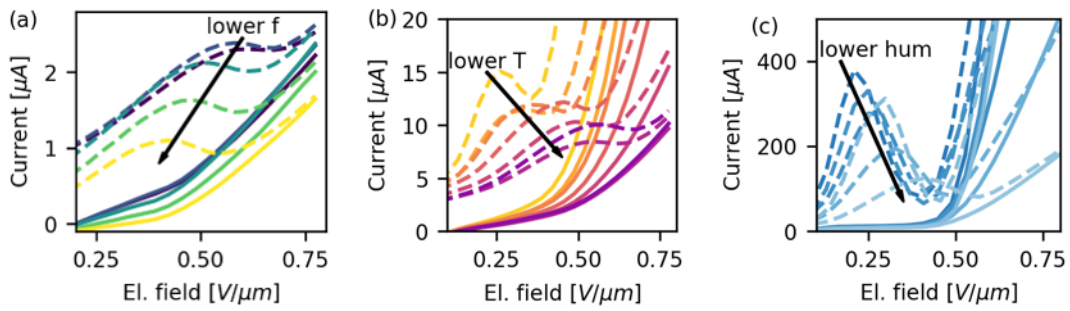

Fig. 35: IV-measurement from frequency-dependent DW-measurements with $f = 0.01$- 0.1 Hz (0.16-1.6 Hz rise frequency). In the first voltage peak, (dashed lines) the frequency-dependent switching peak can be seen. In the second peak, there is no switching, so only background conductivity is measured. The conductivity clearly changes between two different regimes at 2V (0.4V/µm).

measurement frequency or humidity but decreases with increasing temperature. Hence, we attribute the background current to water electrolysis with a temperature-dependent overpotential of about 0.5 V.

C. Temperature and humidity dependent ferroelectric analysis

Having shown how temperature and humidity alter the material's basic electronic properties, it becomes imperative to investigate the ferroelectric properties with changing temperature and humidity. The normalized temperature-dependent CV loops (Fig. 36(a)) show several interesting features. First, all curves show the typical "butterfly peaks" with peak positions, indicating the coercive field, decreasing with higher temperature. The capacitance decreases strongly with increasing field before leveling off, indicating the saturating orientation of paraelectric dipoles as this behavior is not hysteretic. As already indicated in Fig. 33(b), the integrated temperature-dependent CV-loops (Appendix L) only account for a small fraction of the remnant polarization that, importantly, increases with increasing temperature and humidity. This indicates that the ferroelectric switching becomes increasingly reversible, even if it remains, overall, dominated by irreversible domain wall motion. These trends are consistent with the notion that the polarization reversal – ferroelectricity – is somehow connected to the (complex) electronic conductivity.

At 40 and 50% rh, the CV-loops (light blue curves in Fig. 36(b)) look similar to the CV-curves at elevated temperatures (80-90 °C) and show a single dominant peak. The measurement at 70% rh however shows three distinct peaks for increasing and one for decreasing voltage. Signs of these peaks can also be seen at lower temperatures and humidity levels. The third peak, which is mainly visible at 70% rh around 0.6 V/µm, has a corresponding peak for decreasing voltage, which resembles the behavior of an antiferroelectric [205]; there is, however, insufficient data to allow definite conclusions. These findings again show that humidity and temperature have similar effects and that high humidity can push the material into states unreachable by mere thermal activation under dry, or actually drier, conditions as the material starts to show pronounced degradation around 100 °C.

The existence of a double peak structure has been observed for materials with 90° and 180° domain walls due to the ferroelastic switching of the 90° domain walls [206]. As TOZTAF

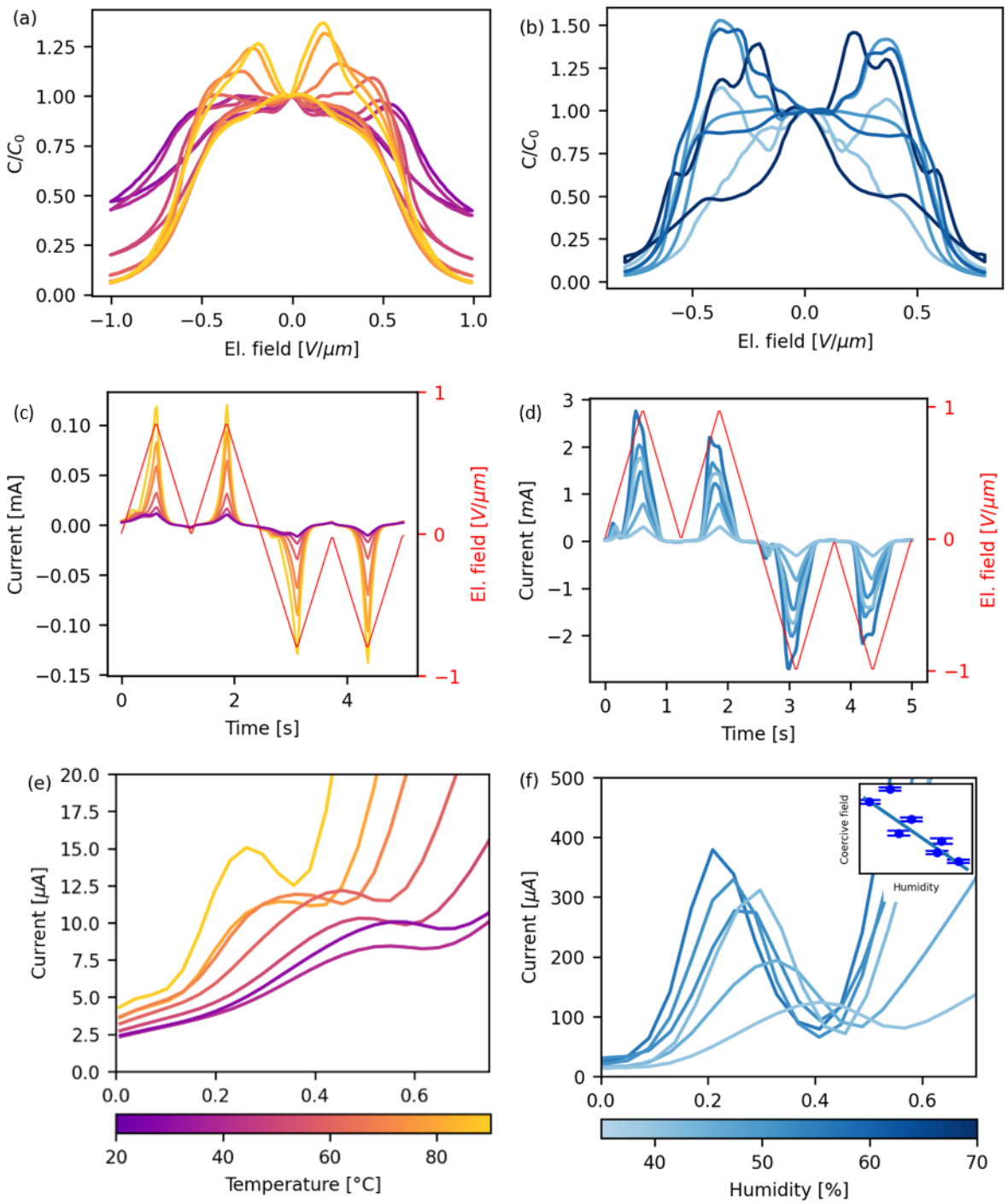

Fig. 36: a) temperature- and b) humidity-dependent CV-loops c) temperature- and d) humidity-dependent double wave measurements, e) and f) zoom-in of c) and d), the inset to f shows the coercive field as function of humidity, the line is a linear fit to guide the eye. T- and % rh-dependent CV-curves are measured at 32% rh and RT respectively, the DW-measurements at 29% rh and 24 °C (RT).

however only allows for 180° switching, the double peak cannot be caused by the ferroeleastic switching. The presence of a double or even triple peak in the CV-loops suggests therefore either a two- or multi-step switching process around RT, where the later steps either require higher electric fields than the first or indicate the presence of two or more independent dipolar lattices. Since neither structure simulations nor XRD data showed

any indication of multiple sublattices, we regard the latter explanation as improbable. Possible multi-step switching paths will be discussed in more detail below.

DW measurements with similar parameters to those for the CV measurements are shown in Fig. 36(c)/(d). As expected on the basis of the finite conductivity discussed above, the switching peak in the first voltage wave is superimposed on a relatively high background current, which increases with temperature and humidity (cf. Fig. 34). A zoom-in on the switching peaks of the DW-measurements (Fig. 36(e)/(f)) shows that the peaks are broader than in the CV-loops, spanning the region where both peaks were observed in the latter. Although they therefore do not allow to resolve any double peak structure, they do follow the same general trends of the coercive field.

At high humidity, there appears an additional peak at higher voltages, sitting roughly at the position of the third peak in the CV-loops. Crucially, this peak appears in both voltage waves, which is not consistent with ferroelectric switching, but could be a sign of antiferroelectric behavior. An antiferroelectric should also have a negative current peak with decreasing voltage, similar to the peak observed in the CV-loop [162]. Even though the downwards curves are somewhat concave, no firm conclusions can be drawn about antiferroelectric behavior that would in any case have to sit beyond the dominant and well-behaved ferroelectric behavior at lower fields.

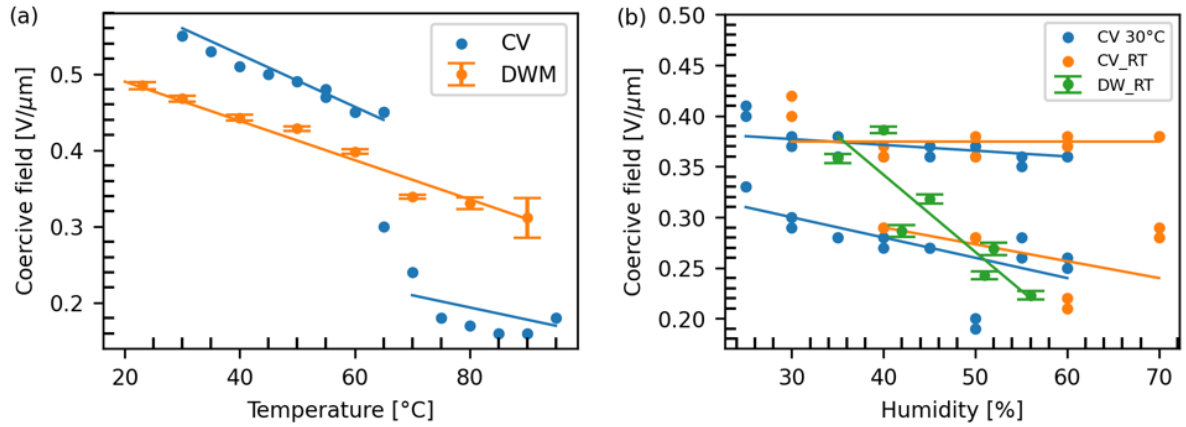

Fig. 37: Coercive field vs temperature at constant humidity of 32 % rh (a) and vs relative humidity at constant temperature as indicated in the legend (b). The DW data and error bars come from gaussian fits to the switching peak, the CV data are manually acquired values of pronounced peaks, the number of which increases with humidity. Lines are guidelines for the eye.

The coercive field for temperature- and humidity-dependent DW and CV measurements is plotted in Fig. 37. At ambient humidity levels, ~25 % rh and above, the coercive field has a similar temperature and humidity dependence as the (protonic) complex conductivity, cf. Fig. 34. As the coercive field analysis in Fig. 33 has shown that switching is nucleation-limited, the former finding indicates that nucleation in all likelihood involves a proton transfer step. This hypothesis is supported by the (tentative) observation that the lower coercive field, corresponding to the nucleation step in Fig. 37(b), shows a decreasing trend with increasing humidity, while the higher coercive field seems to be (almost) independent of humidity beyond ≈ 35 % rh.

Notably, all the measurements shown in Fig. 37 start at 25 % rh, as below that, no switching was observed around room temperature (Appendix M). As also shown there, the material does show indications of ferroelectric switching under vacuum conditions from ~60 °C onward, with a coercive field around 0.1-0.2 V/µm. Interestingly, the CV-data in Fig. 37(a), and to a lesser degree the DW-data in Fig. 33 (d), show a significant drop in coercive field around 60 °C, to a coercive field in the same range. This suggests a transition to another nucleation mechanism that is less reliant on proton mobility. The absence of any noticeable features in the temperature-dependent conductivity data in Fig. 34(a) suggests it is not the proton conduction itself that is qualitatively affected by the higher temperatures, but rather that its role in providing nucleation centers gets taken over by another process. We will not pursue this topic in further detail here and focus on the behavior around RT.

D. Most probable switching mechanism

Following the discussion above, we propose a two-step polarization switching process at room temperature and ambient humidity. Starting from the simulated [67] and measured (chapter IV) crystal structure (Fig. 38, left panel), the first step must involve a proton transfer as switching (nucleation) strongly depends on the ambient humidity, which in turn influences the proton mobility [156]. A possible proton transfer pathway is indicated as step 1 in Fig. 38 and involves an intra-molecular proton transfer in both the DL-malate and the hexamine molecules; despite this step involving two proton jumps, we consider this more likely than independent jumps because of the high electrostatic penalty of the hypothetical intermediate state after just a single proton has jumped. The resulting state is shown in the middle panel of Fig. 38 and is not a mirror image of the initial state.

To achieve full polarization reversal, i.e., a mirror image of the initial state, the second step (2a in Fig. 38) needs to involve the rotation of the malate-ion, in combination with a proton back-transfer and, possibly, a minor sliding motion or rotation of the hexamine molecules. In view of the globular shape of the molecules, which was actually a filter criterion for the data mining approach used to identify this compound [67], we consider such a process plausible. Moreover, the field needed for the rotation(s) is unlikely to depend strongly on the humidity or proton mobility, in agreement with the weak humidity-dependence of the second feature in the CV data in Fig. 37(b). The resulting final state depicted in Fig. 38, upper right, is the mirror image of the initial state.

We note that, starting from the intermediate state, a further inter-molecular proton transfer from the DL-malate to the hexamine in the layer above, and similarly from the hexamine in the layer below to the DL-malate, brings back the original situation, cf. the process 2b in Fig. 38. In combination with the first step, this pathway corresponds to DC proton conductivity. In analogy to (electronic) hopping conduction in disordered organic semiconductors, this process should be possible at arbitrary voltages, that is, also at voltages lower than the first coercive field [207]. In contrast, to enable ferroelectric switching, the intermediate state needs to be stable on the time scale of the molecular rotation(s) in the second step that are much slower than electronic or protonic hopping. We hypothesize that only for fields at or beyond the first

coercive field this stability is given. In passing, we note that the same asymmetric Marcus-type hopping mechanism that gives rise to the polarization-dependent electronic conductivity in semiconducting organic ferroelectrics is likely to also apply to proton hopping. [4], [110], [146].

Although we cannot be sure of the details of the proposed mechanism, we note that this mechanism provides a natural explanation for the coupling between the proton-transport-based electronic properties of the material and the ferroelectric switching. Moreover, we regard alternatives that are fundamentally different as significantly less likely. For example, mechanisms which only involve proton transfers are implausible as these do not result in full unit cell inversion due to the asymmetry of the malate-ion. Likewise, mechanisms only involving rotations do not explain the strong influence of humidity on the ferroelectric properties. Sketches of examples of such processes are shown in Appendix N.

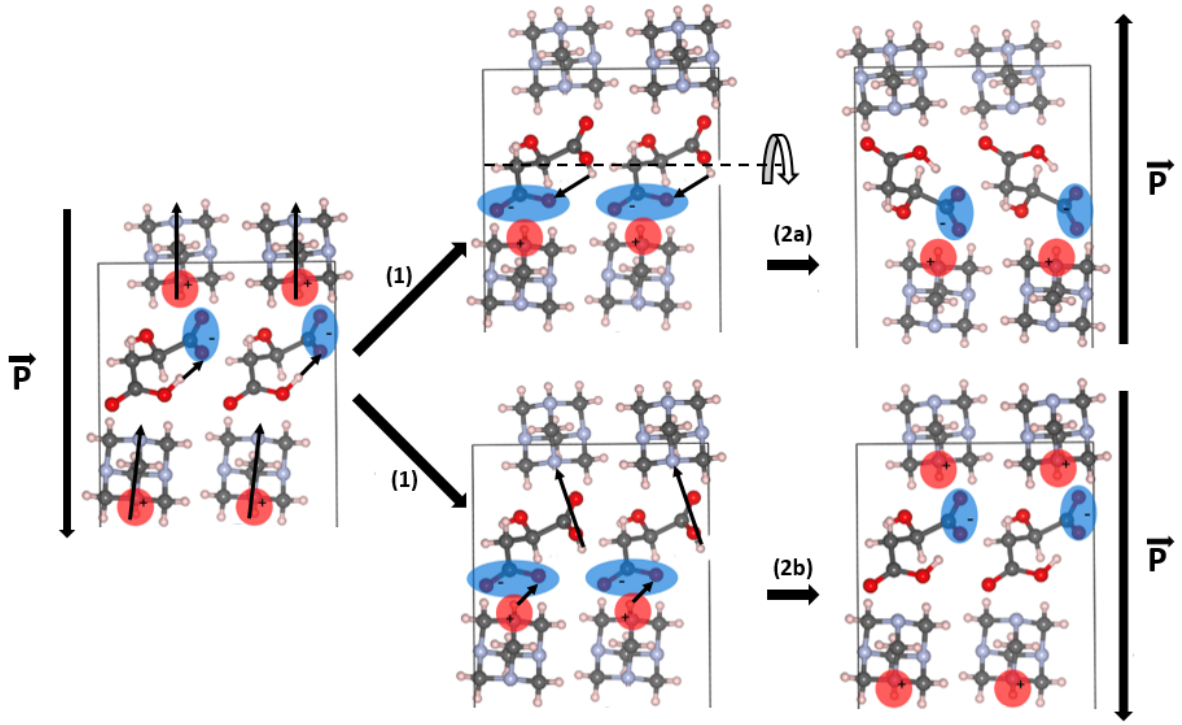

Fig. 38: Schematic of the proposed polarization reversal and proton conduction mechanism. Both processes start with a double intra-molecular proton transfer (black arrows in left image, step 1). Step 2a: Polarization reversal is then induced by a rotation of the malate ion and a proton back-transfer, resulting in a mirror image of the starting point. Step 2b:Proton conduction occurs by two further inter-molecular proton hops, which return the system to the initial state.

E. Summary and outlook

In this chapter, we have provided a detailed characterization of the ferroelectric properties of the organic ionic cocrystal DL-malate:hexamine (TOZTAF) in polycrystalline thin-film form. Our results confirm it as a high-performance ferroelectric, exhibiting all the canonical switching characteristics.

The material delivers a robust remnant polarization of approximately 15 $\mu C/cm^2$, making it competitive with many established materials. The most significant finding is its exceptionally low coercive field, which reaches values as low as ~0.2 V/µm. It is two orders of magnitude lower than typical organic polymers like P(VDF:TrFE) and an order of magnitude lower than the premier organic proton-transfer material, croconic acid. This ultra-low coercive field is highly desirable for applications, as it enables switching voltages in the 1-2 V range with low-cost fabrication techniques that produce channel lengths of several micrometers.

The most scientifically compelling feature of TOZTAF is the strong, intertwined dependence of its ferroelectric switching and complex electrical conductivity on both temperature and ambient humidity. We demonstrate that the material's properties, particularly its coercive field, are strongly modulated by humidity, which we attribute to the material's protonic conductivity.

The observation of a distinct double-peak structure in the capacitance-voltage loops provides clear evidence for a multi-step polarization reversal process. We propose a mechanism where the initial, humidity-dependent step is a proton transfer (which also facilitates long-range charge transport), followed by a humidity-independent molecular rotation to complete the polarization reversal. This coupling — where the ferroelectric switching pathway and the charge transport mechanism share a common physical step — is a rare and significant finding, highlighting a new class of multifunctional material behavior.

The coupling of background conductivity to the polarization has potential for an easy, non-destructive, readout of the polarization state in ferroelectric memory devices, whereas the coupling of the (ferro)electric properties to the ambient humidity shows potential for use in sensors and responsive devices.

Apart from optimization for applications, further work is also needed to understand the thermally activated mechanisms above 60 °C as well as understanding how different fabrication techniques and morphologies influence performance, especially with regard to how deeply and to which degree the humidity penetrates into the bulk material. Definitive proof of the importance of the proton-transfer for ferroelectric switching could be achieved by deuterating the material. However, the strong coupling of the material with ambient humidity necessitates that the entire experiment is conducted under a controlled atmosphere with deuterated water, an experimental challenge that was beyond the scope of this project.

Furthermore, studies on other proton-transfer ferroelectrics are needed to investigate whether they show similar humidity-dependency.

Overall, these results highlight that organic ferroelectrics, discovered through modern data-centric approaches, can exhibit surprisingly complex and rich phenomenology. TOZTAF is a prime example of a material that not only delivers benchmark performance but also provides a novel, tunable functionality that could be exploited in the next generation of smart and responsive devices.

VI. Conclusion

In summary, this thesis investigated four candidate materials selected via database mining to verify their ferroelectric behavior. Three of the four materials exhibited strong evidence of ferroelectricity while the last had inconclusive results, resulting in a high success rate of 75%. Detailed investigation of the first material, TOZTAF, revealed that its ferroelectric properties are intrinsically linked to ambient humidity. This dependence was explained by humidity-modulated proton mobility, which governs both the protonic conductivity and the ferroelectric switching process in this class of proton-transfer ferroelectrics.

The successful outcome of this project validates the proposed experimental framework, centered on dielectric spectroscopy, the double wave method, and CV loops, as a robust and standardizable routine for verifying new ferroelectric candidates. This procedure is generalizable and can be readily applied to the characterization of a wide range of other potentially ferroelectric materials. It however needs to be noted that a negative result in one parameter space does not exclude ferroelectricity under different measurement parameters, processing and environmental conditions.

The high success rate of 75% suggests that among the remaining 62 uninvestigated candidates from the two database searches, there may be more than 40 undiscovered ferroelectrics. While this prospect is promising, the current experimental verification process remains labor-intensive. To streamline future discovery, I propose these improvements to the screening strategy:

Some of the investigated materials were not stable under ambient conditions or decomposed quickly after application of an electric field. Future database mining should therefore incorporate additional assessment criteria such as melting temperature, decomposition pathways, as well as simple estimates of vapor pressure and environmental stability. This would prioritize materials that are stable under ambient conditions, facilitating experimental handling and increasing the feasibility of device applications. Focusing only on commercially available materials made the process in this work easier, but necessarily shrinks the number of possible materials dramatically, which is why it should not be generally applied.

These improvements however do not address a broader underlying problem, being that the simulation in many cases only suggests potential ferroelectrics based on symmetry and polarization without considering the switching mechanism. Without the switching pathway, it is impossible to estimate a coercive field, which also has implications about the polarization retention.

Currently, this is addressed by heuristically generalizing known switching paths, but this method is imprecise. This limitation can be seen for **material 2**, where only ion displacement can invert the polarization, while the molecular rotation assumed by the screening filter cannot achieve ferroelectric switching. Addressing this challenge could also greatly benefit from computational approaches, which would calculate possible switching paths with a

combination of DFT and MD simulations as performed in [110]. This is, however, very computation-intensive and requires the incorporation of electric fields and is therefore probably not suitable for large-scale screening studies.

To not rely on DFT/MD calculations for every material, a generalized database mining study might follow a structure like this:

1. **Screening for Polarity**: Filter the dataset for materials exhibiting a polar space group as well as electronegativity differences, a prerequisite for macroscopic electric polarization.
2. **Practicality filter**: As discussed above, it is advantageous to filter the materials for their practicability with parameters like melting temperature, decomposition pathways, vapor pressure, and environmental stability. Depending on how challenging this proves to be, this can also be employed at a later point.
3. **Polarization Quantification:** Calculate whether the structure has a significant magnitude of polarization.
4. **Source Identification:** Classify the materials by the structural origin of their polarization. While this seems easy in theory, an efficient procedure to automate this still needs to be developed. The categories would be:
    a. Charged ions or molecules in a polar arrangement
    b. One or multiple dipolar bonds within the molecule or a dipolar charge-imbalance across the entire molecule
    c. The proton position within hydrogen bond networks
    d. Not all materials will fall into these three categories. TOZTAF (**material 1**) is an example of this as it has properties of b and c. These materials will have to be analyzed in more detail and probably require a more specialized investigation.
5. **Mechanism Deduction:** Based on the source of the polarization, the likely switching mechanism can be inferred:
    a. **Displacive**: Displacement of the ions or ionic molecules
    b. **Permanent dipole reorientation**: Rotation of the dipolar group or entire molecule
    c. **Proton transfer**
6. **Viability Assessment:** Finally, the energetic feasibility of the proposed switching mechanism must be evaluated. This presents likely the biggest challenge. Advances in machine learning as well as bond breaking simulations in other systems (e.g. collagen fibers [208]) might help develop these methods.

This approach should be able to find most ferroelectrics hidden in the underlying database. It is however probably very challenging to apply this entire process, so focusing on a subset (like only displacive ferroelectrics) might be a more achievable sub goal in this process.

Another possibly more addressable challenge is to understand the ferro-to-paraelectric phase transition in these compounds, which can benefit from the recent machine learning force

fields that can be used in molecular dynamics simulations, as recently done for the $HdabcoClO_4$ ferroelectric molecular crystal [209]. However, understanding complex switching paths, including nucleation effects may also require novel multi-scale approaches, or a combination of computational and heuristic assessments.

Overall, these results highlight that organic ferroelectrics, discovered through modern data-centric approaches, can exhibit surprisingly complex and rich phenomenology. TOZTAF is a prime example of a material that not only delivers benchmark performance but also provides a novel, tunable functionality that could be exploited in the next generation of smart and responsive devices.

VII. Declaration of AI use

I have used Googles Gemini for finding errors in the entire manuscript as well as improving the wording. It was also used to highlight applications of organic electronics and ferroelectrics. It was never used to generate sections from scratch and all information (regarding applications) was confirmed by other sources.

VIII. Acknowledgements

I could not have successfully completed this project alone. While many people have supported me, my special thanks go to:

Prof. Martijn Kemerink for giving me the opportunity to pursue this project as well as all the advice and open door that he always had.

Prof. Alexander Colsmann for being my second adviser and the time he invested in making the entire process possible.

Prof. Milan Kivala and Prof. Wolfram Pernice for taking the time to join the defense committee.

Prof. Christine Selhuber-Unkel and Dr. Clemens Göhler for supervising my project in the thesis advisory committee.

Ramon Jannasch and Dr. Manjunath Balagopalan as well as Elin Dypvik Sødahl, Seyedmojtaba Seyedraoufi, Carl Henrik Gørbitz, Kristian Berland, and Ola Nilsen, for the pleasant and successful cooperation.

All members of the Kemerink group, especially Dr. Dorothea Scheunemann and Henna Tuikka-Graf, who in many cases kept the group running, my fellow co-PhD students Andrey, Heiko, Anton, Constantin, Morty, Priya, Sophia, and Tobias who were always a nice source of practical as well as emotional support.

My family, girlfriend, and friends for supporting me whenever I needed it.

IX. Bibliography

[1] M. Litterst, A. A. Butkevich, and M. Kemerink, “Inconclusive proof of ferroelectricity in peptide-VDF ribbons,” *Nat. 2025 6448075*, vol. 644, no. 8075, pp. E1–E3, Aug. 2025, doi: 10.1038/s41586-025-09314-2.

[2] M. Litterst *et al.*, “Experimentally confirmed ferroelectricity in organic compounds identified by database mining.”

[3] M. Litterst *et al.*, “Humidity-tunable organic ferroelectric with low coercive field.”

[4] H. Mager *et al.*, “A supramolecular ferroelectric with two sublattices and polarization dependent conductivity,” Jul. 2025, Accessed: Jul. 16, 2025. [Online]. Available: https://arxiv.org/abs/2507.11309v1.

[5] World Economic Forum, “Global Risks Report 2025,” 2025. Accessed: Oct. 02, 2025. [Online]. Available: https://www.weforum.org/publications/global-risks-report-2025/.

[6] The Intergovernmental Panel on Climate Change, “AR6 Synthesis Report: Climate Change 2023 — IPCC,” 2023. Accessed: Oct. 02, 2025. [Online]. Available: https://www.ipcc.ch/report/sixth-assessment-report-cycle/.

[7] Q. Wang, N. Huang, Z. Chen, X. Chen, H. Cai, and Y. Wu, “Environmental data and facts in the semiconductor manufacturing industry: An unexpected high water and energy consumption situation,” *Water Cycle*, vol. 4, pp. 47–54, Jan. 2023, doi: 10.1016/J.WATCYC.2023.01.004.

[8] I. McCulloch, M. Chabinyc, C. Brabec, C. B. Nielsen, and S. E. Watkins, “Sustainability considerations for organic electronic products,” *Nat. Mater. 2023 2211*, vol. 22, no. 11, pp. 1304–1310, Jun. 2023, doi: 10.1038/s41563-023-01579-0.

[9] I. Siddiqui *et al.*, “Status and Challenges of Blue OLEDs: A Review,” *Nanomaterials*, vol. 13, no. 18, p. 2521, Sep. 2023, doi: 10.3390/NANO13182521/S1.

[10] “OLED Market Size, Share, Growth & Trends Report, 2030.” https://www.grandviewresearch.com/industry-analysis/oled-market-report (accessed Oct. 02, 2025).

[11] M. Jørgensen *et al.*, “The state of organic solar cells—A meta analysis,” *Sol. Energy Mater. Sol. Cells*, vol. 119, pp. 84–93, Dec. 2013, doi: 10.1016/J.SOLMAT.2013.05.034.

[12] P. G. V. Sampaio and M. O. A. González, “A review on organic photovoltaic cell,” *Int. J. Energy Res.*, vol. 46, no. 13, pp. 17813–17828, Oct. 2022, doi: 10.1002/ER.8456.

[13] “Best Research-Cell Efficiency Chart | Photovoltaic Research | NREL.” https://www.nrel.gov/pv/cell-efficiency (accessed Oct. 02, 2025).

[14] “Oxford PV.” https://www.oxfordpv.com/press-releases/oxford-pv-solar-technology-patent (accessed Oct. 02, 2025).

[15] J. Zhu, J. Xia, Y. Li, and Y. Li, “Perspective on Flexible Organic Solar Cells for Self-Powered Wearable Applications,” *ACS Appl. Mater. Interfaces*, vol. 17, no. 4, pp. 5595–5608, Jan. 2025, doi:

10.1021/ACSAMI.4C12238/ASSET/IMAGES/LARGE/AM4C12238_0005.JPEG.

[16] Z. Wu *et al.*, “Human-friendly semitransparent organic solar cells achieving high performance,” *Energy Environ. Sci.*, vol. 17, no. 16, pp. 6013–6023, Aug. 2024, doi: 10.1039/D4EE01659A.

[17] L. Li, L. Han, H. Hu, and R. Zhang, “A review on polymers and their composites for flexible electronics,” *Mater. Adv.*, vol. 4, no. 3, pp. 726–746, Feb. 2023, doi: 10.1039/D2MA00940D.

[18] K. Liu, B. Ouyang, X. Guo, Y. Guo, and Y. Liu, “Advances in flexible organic field-effect transistors and their applications for flexible electronics,” *npj Flex. Electron. 2022 61*, vol. 6, no. 1, pp. 1–19, Jan. 2022, doi: 10.1038/s41528-022-00133-3.

[19] R. Xiao, X. Zhou, C. Zhang, X. Liu, S. Han, and C. Che, “Organic Thermoelectric Materials for Wearable Electronic Devices,” *Sensors 2024, Vol. 24, Page 4600*, vol. 24, no. 14, p. 4600, Jul. 2024, doi: 10.3390/S24144600.

[20] H. Liu, J. Song, Z. Zhao, S. Zhao, Z. Tian, and F. Yan, “Organic Electrochemical Transistors for Biomarker Detections,” *Adv. Sci.*, vol. 11, no. 27, p. 2305347, Jul. 2024, doi: 10.1002/ADVS.202305347.

[21] S. A. Moiz, M. S. Alshaikh, and A. N. M. Alahmadi, “Organic Bioelectronics: Diversity of Electronics Along with Biosciences,” *Biosens. 2025, Vol. 15, Page 587*, vol. 15, no. 9, p. 587, Sep. 2025, doi: 10.3390/BIOS15090587.

[22] “FRAM Memory Chips’ advantages and applications.” https://kdtic.com/exploring-the-fram-memory-chips/ (accessed Oct. 06, 2025).

[23] “What Is Ferroelectric RAM (FRAM)? History, Uses, Features.” https://www.ic-components.com/blog/what-is-ferroelectric-ram(fram)-history,uses,features.jsp (accessed Oct. 06, 2025).

[24] “FRAM: Ferroelectric Random Access Memory | Lenovo US.” https://www.lenovo.com/us/en/glossary/what-is-fram/ (accessed Oct. 06, 2025).

[25] “FeRAM: Innovative alternative to EEPROM.” https://www.memorysolution.de/en/FeRAM-Innovative-alternative-to-EEPROM.

[26] T. Mikolajick, U. Schroeder, and S. Slesazeck, “The Past, the Present, and the Future of Ferroelectric Memories,” *IEEE Trans. Electron Devices*, vol. 67, no. 4, pp. 1434–1443, Apr. 2020, doi: 10.1109/TED.2020.2976148.

[27] “Ferroelectric RAM Market Size, Share and Growth Report 2032.” https://www.credenceresearch.com/report/ferroelectric-ram-market (accessed Oct. 06, 2025).

[28] A. Sultana, M. M. Alam, T. R. Middya, and D. Mandal, “A pyroelectric generator as a self-powered temperature sensor for sustainable thermal energy harvesting from waste heat and human body heat,” *Appl. Energy*, vol. 221, pp. 299–307, Jul. 2018, doi: 10.1016/J.APENERGY.2018.04.003.

[29] A. Thakre, A. Kumar, H. C. Song, D. Y. Jeong, and J. Ryu, “Pyroelectric Energy Conversion and Its Applications—Flexible Energy Harvesters and Sensors,” *Sensors 2019, Vol. 19, Page 2170*, vol. 19, no. 9, p. 2170, May 2019, doi: 10.3390/S19092170.

[30] Y. Yang, Y. Zhou, J. M. Wu, and Z. L. Wang, “Single micro/nanowire pyroelectric nanogenerators as self-powered temperature sensors,” *ACS Nano*, vol. 6, no. 9, pp. 8456–8461, Sep. 2012, doi: 10.1021/NN303414U/SUPPL_FILE/NN303414U_SI_001.PDF.

[31] X. Wang, Y. Dai, R. Liu, X. He, S. Li, and Z. L. Wang, “Light-Triggered Pyroelectric Nanogenerator Based on a pn-Junction for Self-Powered Near-Infrared Photosensing,” *ACS Nano*, vol. 11, no. 8, pp. 8339–8345, Aug. 2017, doi: 10.1021/ACSNANO.7B03560/ASSET/IMAGES/LARGE/NN-2017-03560X_0004.JPEG.

[32] Z. Wang *et al.*, “Light-induced pyroelectric effect as an effective approach for ultrafast ultraviolet nanosensing,” *Nat. Commun. 2015 61*, vol. 6, no. 1, pp. 1–7, Sep. 2015, doi: 10.1038/ncomms9401.

[33] “Flame detectors - Siemens Global.” https://www.siemens.com/global/en/products/buildings/fire-safety/detection/special-detectors/flame-detectors.html (accessed Oct. 06, 2025).

[34] “Sensor technology & pyroelectric IR sensors.” https://www.infratec-infrared.com/sensor-division/service-support/glossary/sensor-technology/ (accessed Oct. 06, 2025).

[35] “Laser Power and Energy Measurements with Pyroelectric IR Detectors.” https://www.lasercomponents.com/us/photonics-portal/knowledge-center/application-notes/laser-power-and-energy-measurements-with-pyroelectric-ir-detectors/ (accessed Oct. 06, 2025).

[36] W. Wang *et al.*, “Modeling and Compensation of Dynamic Hysteresis with Force-Voltage Coupling for Piezoelectric Actuators,” *Micromachines 2021, Vol. 12, Page 1366*, vol. 12, no. 11, p. 1366, Nov. 2021, doi: 10.3390/MI12111366.

[37] X. Gao *et al.*, “Piezoelectric Actuators and Motors: Materials, Designs, and Applications,” *Adv. Mater. Technol.*, vol. 5, no. 1, p. 1900716, Jan. 2020, doi: 10.1002/ADMT.201900716.

[38] J. Li, Y. Ma, T. Zhang, K. K. Shung, and B. Zhu, “Recent Advancements in Ultrasound Transducer: From Material Strategies to Biomedical Applications,” *BME Front.*, vol. 2022, Jan. 2022, doi: 10.34133/2022/9764501.

[39] “What Are Piezo Diesel Injectors and How Do They Work?” https://www.slturbodiesel.com/what-are-piezo-diesel-injectors-and-how-do-they-work/ (accessed Oct. 07, 2025).

[40] K. Cai, X. He, Y. Tian, X. Liu, D. Zhang, and B. Shirinzadeh, “Design of a XYZ scanner for home-made high-speed atomic force microscopy,” *Microsyst. Technol.*, vol. 24, no. 7, pp. 3123–3132, Jul. 2018, doi: 10.1007/S00542-017-3674-4/FIGURES/13.

[41] D. G. Wakshume and M. Ł. Płaczek, “Optimizing Piezoelectric Energy Harvesting from

Mechanical Vibration for Electrical Efficiency: A Comprehensive Review," *Electron. 2024, Vol. 13, Page 987*, vol. 13, no. 5, p. 987, Mar. 2024, doi: 10.3390/ELECTRONICS13050987.

[42] "The Fundamentals of Piezo Sensors | DigiKey." https://www.digikey.com/en/articles/fundamentals-of-piezoelectric-shock-and-vibration-sensors (accessed Oct. 07, 2025).

[43] Z. Liu, Z. Fu, H. Ma, and D. Jiang, "Piezoelectric Based Touch Sensing for Interactive Displays—A Short Review," *Mater. 2021, Vol. 14, Page 5698*, vol. 14, no. 19, p. 5698, Sep. 2021, doi: 10.3390/MA14195698.

[44] C. Lang, H. Wang, J. Fang, J. Jin, L. Peng, and T. Lin, "Recent advances in acoustoelectric conversion of piezoelectric electrospun nanofibers," *Nano Energy*, vol. 130, p. 110117, Nov. 2024, doi: 10.1016/J.NANOEN.2024.110117.

[45] D. B. Deutz, J. A. Pascoe, B. Schelen, S. Van Der Zwaag, D. M. De Leeuw, and P. Groen, "Analysis and experimental validation of the figure of merit for piezoelectric energy harvesters," *Mater. Horizons*, vol. 5, no. 3, pp. 444–453, May 2018, doi: 10.1039/C8MH00097B.

[46] "GC861/862EW BLE - Wireless Switch - Prolojik." https://www.prolojik.com/datasheet/gc861-862ew-ble-wireless-switch/ (accessed Oct. 07, 2025).

[47] "Piezo igniter - heshuai." https://www.he-shuai.com/piezo-igniter/ (accessed Oct. 07, 2025).

[48] C. Dagdeviren *et al.*, "Conformal piezoelectric energy harvesting and storage from motions of the heart, lung, and diaphragm," *Proc. Natl. Acad. Sci. U. S. A.*, vol. 111, no. 5, pp. 1927–1932, Feb. 2014, doi: 10.1073/pnas.1317233111.

[49] Q. He and J. Briscoe, "Piezoelectric Energy Harvester Technologies: Synthesis, Mechanisms, and Multifunctional Applications," *ACS Appl. Mater. Interfaces* , vol. 16, no. 23, pp. 29491–29520, Jun. 2024, doi: 10.1021/ACSAMI.3C17037/ASSET/IMAGES/LARGE/AM3C17037_0018.JPEG.

[50] E. M. Nia, N. A. W. A. Zawawi, and B. S. M. Singh, "A review of walking energy harvesting using piezoelectric materials," *IOP Conf. Ser. Mater. Sci. Eng.*, vol. 291, no. 1, Jan. 2018, doi: 10.1088/1757-899X/291/1/012026.

[51] "Piezoelectric Materials Market Forecast, Growth, and Future Opportunities." https://www.skyquestt.com/report/piezoelectric-materials-market (accessed Oct. 07, 2025).

[52] "Pyroelectric Material Sales Market Report | Global Forecast From 2025 To 2033." https://dataintelo.com/report/global-pyroelectric-material-sales-market (accessed Oct. 07, 2025).

[53] "Ferroelectric Ram Market Size, Share & Analysis Report, 2032." https://www.gminsights.com/industry-analysis/ferroelectric-ram-market (accessed Oct. 07, 2025).

[54] F. Giraud and C. Giraud-Audine, *Piezoelectric Actuators: Vector Control Method: Basic, Modeling and Mechatronic Design of Ultrasonic Devices*. Elsevier, 2019.

[55] J. Walker *et al.*, "Electromechanical properties of uniaxial polar ionic plastic crystal [(C2H5)4N][FeBrCl3]," *J. Phys. Energy*, vol. 6, no. 2, p. 025026, Apr. 2024, doi: 10.1088/2515-7655/AD405C.

[56] H. Azhari, "Appendix A: Typical Acoustic Properties of Tissues," *Basics Biomed. Ultrasound Eng.*, pp. 313–314, Feb. 2010, doi: 10.1002/9780470561478.APP1.

[57] M. S. Martins *et al.*, "Wideband and Wide Beam Polyvinylidene Difluoride (PVDF) Acoustic Transducer for Broadband Underwater Communications," *Sensors (Basel).*, vol. 19, no. 18, pp. 19–22, Sep. 2019, doi: 10.3390/S19183991.

[58] S. Wang, Y. Wang, Z. Wang, Z. Wu, Y. Xin, and X. Zhou, "A brief review on hydrophone based on PVDF piezoelectric film," *Ferroelectrics*, vol. 603, no. 1, pp. 150–156, 2023, doi: 10.1080/00150193.2022.2159227.

[59] E. D. Sødahl, J. Walker, and K. Berland, "Piezoelectric Response of Plastic Ionic Molecular Crystals: Role of Molecular Rotation," *Cryst. Growth Des.*, vol. 23, no. 2, pp. 729–740, Feb. 2023, doi: 10.1021/ACS.CGD.2C00854.

[60] S. Mohammadpourfazeli, S. Arash, A. Ansari, S. Yang, K. Mallick, and R. Bagherzadeh, "Future prospects and recent developments of polyvinylidene fluoride (PVDF) piezoelectric polymer; fabrication methods, structure, and electro-mechanical properties," *RSC Adv.*, vol. 13, no. 1, pp. 370–387, Jan. 2023, doi: 10.1039/D2RA06774A.

[61] "Our Current Understanding of the Human Health and Environmental Risks of PFAS | US EPA." https://www.epa.gov/pfas/our-current-understanding-human-health-and-environmental-risks-pfas (accessed Oct. 07, 2025).

[62] "EU plans ban on 'forever chemicals' in consumer products | Reuters." https://www.reuters.com/business/environment/eu-plans-ban-forever-chemicals-consumer-products-2025-01-20/ (accessed Oct. 07, 2025).

[63] H. S. Choi *et al.*, "Tailoring the coercive field in ferroelectric metal-free perovskites by hydrogen bonding," *Nat. Commun. 2022 131*, vol. 13, no. 1, pp. 1–7, Feb. 2022, doi: 10.1038/s41467-022-28314-8.

[64] J. Hachmann *et al.*, "Lead candidates for high-performance organic photovoltaics from high-throughput quantum chemistry – the Harvard Clean Energy Project," *Energy Environ. Sci.*, vol. 7, no. 2, pp. 698–704, Jan. 2014, doi: 10.1039/C3EE42756K.

[65] A. Jain *et al.*, "Commentary: The materials project: A materials genome approach to accelerating materials innovation," *APL Mater.*, vol. 1, no. 1, p. 11002, Jul. 2013, doi: 10.1063/1.4812323/119685.

[66] Y. Mo, S. P. Ong, and G. Ceder, "First principles study of the Li 10GeP 2S 12 lithium super ionic conductor material," *Chem. Mater.*, vol. 24, no. 1, pp. 15–17, Jan. 2012, doi: 10.1021/CM203303Y/SUPPL_FILE/CM203303Y_SI_001.PDF.

[67] E. Dypvik Sødahl, S. Seyedraoufi, C. H. Görbitz, and K. Berland, “Ferroelectric Crystals of Globular Molecules: Cambridge Structural Database Mining and Computational Assessment,” *Cryst. Growth Des.*, vol. 23, no. 12, pp. 8607–8619, Dec. 2023, doi: 10.1021/ACS.CGD.3C00713.

[68] S. Seyedraoufi, E. D. Sødahl, C. H. Görbitz, and K. Berland, “Database mining and first-principles assessment of organic proton-transfer ferroelectrics,” *Phys. Rev. Mater.*, vol. 8, no. 5, p. 054413, May 2024, doi: 10.1103/PHYSREVMATERIALS.8.054413.

[69] W. Demtröder, “Dielektrika im elektrischen Feld,” in *Experimentalphysik 2, Elektrizität und Optik*, 2017, pp. 22–28.

[70] W. Demtröder, “Der elektrische Strom,” in *Experimentalphysik 2*, Springer Spektrum, Berlin, Heidelberg, 2017, pp. 41–78.

[71] A. F. Devonshire, “Theory of ferroelectrics,” *Adv. Phys.*, vol. 3, no. 10, pp. 85–130, 1954, doi: 10.1080/00018735400101173.

[72] L. Landau, “ON THE THEORY OF PHASE TRANSITIONS,” *Collect. Pap. L.D. Landau*, pp. 193–216, Jan. 1965, doi: 10.1016/B978-0-08-010586-4.50034-1.

[73] P. Chandra and P. B. Littlewood, “A Landau Primer for Ferroelectrics,” *Top. Appl. Phys.*, vol. 105, pp. 69–116, 2007, doi: 10.1007/978-3-540-34591-6_3.

[74] D. Fasquelle and J. C. Carru, “Electrical characterizations of PZT ceramics in large frequency and temperature ranges,” *J. Eur. Ceram. Soc.*, vol. 28, no. 10, pp. 2071–2074, Jan. 2008, doi: 10.1016/J.JEURCERAMSOC.2008.01.024.

[75] J. F. Legrand, “Structure and ferroelectric properties of P(VDF-TrFE) copolymers,” *Ferroelectrics*, vol. 91, no. 1, pp. 303–317, Mar. 1989, doi: 10.1080/00150198908015747.

[76] A. V. Gorbunov *et al.*, “True ferroelectric switching in thin films of trialkylbenzene-1,3,5-tricarboxamide (BTA),” *Phys. Chem. Chem. Phys.*, vol. 18, no. 34, pp. 23663–23672, 2016, doi: 10.1039/c6cp03835b.

[77] J. F. Scott, “Ferroelectrics go bananas,” *J. Phys. Condens. Matter*, vol. 20, no. 2, pp. 9–11, 2008, doi: 10.1088/0953-8984/20/02/021001.

[78] Y. Wan, Z. Li, Z. Xu, S. Fan, and X. Yao, “Phase transition characteristics of the relaxor-based 0.24PIN–0.51PMN–0.25PT single crystals,” *J. Alloys Compd.*, vol. 558, pp. 244–247, May 2013, doi: 10.1016/J.JALLCOM.2013.01.034.

[79] S. M. Yang *et al.*, “Ac dynamics of ferroelectric domains from an investigation of the frequency dependence of hysteresis loops,” *Phys. Rev. B - Condens. Matter Mater. Phys.*, vol. 82, no. 17, p. 174125, Nov. 2010, doi: 10.1103/PHYSREVB.82.174125/FIGURES/4/THUMBNAIL.

[80] L. Pintilie, M. Lisca, and M. Alexe, “Polarization reversal and capacitance-voltage characteristic of epitaxial Pb (Zr,Ti) O3 layers,” *Appl. Phys. Lett.*, vol. 86, no. 19, pp. 1–3, May 2005, doi: 10.1063/1.1926403/756994.

[81] I. Urbanaviciute *et al.*, “Negative piezoelectric effect in an organic supramolecular ferroelectric,” *Mater. Horizons*, vol. 6, no. 8, pp. 1688–1698, Sep. 2019, doi: 10.1039/C9MH00094A.

[82] A. K. Batra and M. D. Aggarwal, “Fundamentals of Pyroelectric Materials,” in *Pyroelectric Materials: Infrared Detectors, Particle Accelerators, and Energy Harvesters*, vol. PM231, SPIE, 2013, pp. 1–18.

[83] J. Curie and P. Curie, “Développement par compression de l’électricité polaire dans les cristaux hémièdres à faces inclinées,” *Bull. Minéralogie*, vol. 3, no. 4, pp. 90–93, 1880, doi: 10.3406/BULMI.1880.1564.

[84] I. Katsouras *et al.*, “The negative piezoelectric effect of the ferroelectric polymer poly(vinylidene fluoride),” *Nat. Mater. 2015 151*, vol. 15, no. 1, pp. 78–84, Oct. 2015, doi: 10.1038/nmat4423.

[85] Y. Liu, Q. Wang, Y. Liu, and Q. Wang, “Ferroelectric Polymers Exhibiting Negative Longitudinal Piezoelectric Coefficient: Progress and Prospects,” *Adv. Sci.*, vol. 7, no. 6, p. 1902468, Mar. 2020, doi: 10.1002/ADVS.201902468.

[86] H. Ohsato and H. Ohsato, “Origin of Piezoelectricity on Langasite,” *Mater. Sci. Technol.*, Mar. 2012, doi: 10.5772/18077.

[87] E. John W. Anthony, Richard A. Bideaux, Kenneth W. Bladh, and Monte C. Nichols, “Quartz,” in *Handbook of Mineralogy*, 2001, p. 3023.

[88] S. Horiuchi and Y. Tokura, “Organic ferroelectrics,” *Nat. Mater.*, vol. 7, no. 5, pp. 357–366, 2008, doi: 10.1038/nmat2137.

[89] P. K. Panda and B. Sahoo, “PZT to Lead Free Piezo Ceramics: A Review,” *Ferroelectrics*, vol. 474, no. 1, pp. 128–143, Jan. 2015, doi: 10.1080/00150193.2015.997146.

[90] Z. Sun *et al.*, “Exploring a Lead-free Semiconducting Hybrid Ferroelectric with a Zero-Dimensional Perovskite-like Structure,” *Angew. Chemie*, vol. 128, no. 39, pp. 12033–12037, Sep. 2016, doi: 10.1002/ANGE.201606079.

[91] Y. Hu *et al.*, “Ferroelastic-switching-driven large shear strain and piezoelectricity in a hybrid ferroelectric,” *Nat. Mater. 2021 205*, vol. 20, no. 5, pp. 612–617, Jan. 2021, doi: 10.1038/s41563-020-00875-3.

[92] F. Kagawa, S. Horiuchi, M. Tokunaga, J. Fujioka, and Y. Tokura, “Ferroelectricity in a one-dimensional organic quantum magnet,” *Nat. Phys. 2010 63*, vol. 6, no. 3, pp. 169–172, Jan. 2010, doi: 10.1038/nphys1503.

[93] D. Khomskii, “Peierls structural transition,” in *Basic aspects of the quantum theory of solids : order and elementary excitations*, 2010, pp. 188–198.

[94] G. Grüner, “The one-dimensonal elecron gas,” in *Density waves in solids*, 1994, pp. 1–17.

[95] N. A. Spaldin, “A beginners guide to the modern theory of polarization,” *J. Solid State Chem.*, vol. 195, pp. 2–10, 2012, doi: 10.1016/j.jssc.2012.05.010.

[96] “Ferroelectric Materials Market Size To Hit USD 8.43 Bn By 2034.” https://www.precedenceresearch.com/ferroelectric-materials-market (accessed Aug. 26, 2025).

[97] B. S. Kim, J. H. Ji, and J. H. Koh, “Improved strain and transduction values of low-temperature sintered CuO-doped PZT-PZNN soft piezoelectric materials for energy harvester applications,” *Ceram. Int.*, vol. 47, no. 5, pp. 6683–6690, Mar. 2021, doi: 10.1016/J.CERAMINT.2020.11.008.

[98] A. J. Lovinger, “Ferroelectric Polymers,” *Science (80-.).*, vol. 220, no. 4602, pp. 1115–1121, Jun. 1983, doi: 10.1126/SCIENCE.220.4602.1115.

[99] P. Martins, A. C. Lopes, and S. Lanceros-Mendez, “Electroactive phases of poly(vinylidene fluoride): Determination, processing and applications,” *Prog. Polym. Sci.*, vol. 39, no. 4, pp. 683–706, Apr. 2014, doi: 10.1016/J.PROGPOLYMSCI.2013.07.006.

[100] L. Li, M. Zhang, M. Rong, and W. Ruan, “Studies on the transformation process of PVDF from α to β phase by stretching,” *RSC Adv.*, vol. 4, no. 8, pp. 3938–3943, Dec. 2013, doi: 10.1039/C3RA45134H.

[101] W. J. Hu *et al.*, “Universal Ferroelectric Switching Dynamics of Vinylidene Fluoride-trifluoroethylene Copolymer Films,” *Sci. Reports 2014 41*, vol. 4, no. 1, pp. 1–8, Apr. 2014, doi: 10.1038/srep04772.

[102] M. S. Ravisankar and R. B. Gangineni, “Study of relaxation kinetics in PVDF interconnected nanodots using piezo force microscopy,” *J. Mater. Sci. Mater. Electron.*, vol. 34, no. 8, pp. 1–9, Mar. 2023, doi: 10.1007/S10854-023-10122-5.

[103] C. Revenant, S. Toinet, E. Lawrence Bright, and M. Benwadih, “The Longitudinal and Transverse Piezoelectric Effects of the Ferroelectric Polymer P(VDF-TrFE),” *Macromol. Mater. Eng.*, p. 2400420, 2025, doi: 10.1002/MAME.202400420.

[104] X. Wang, B. Qiao, S. Tan, W. Zhu, and Z. Zhang, “Tuning the ferroelectric phase transition of PVDF by uniaxially stretching crosslinked PVDF films with CF[double bond, length as m-dash]CH bonds,” *J. Mater. Chem. C*, vol. 8, no. 33, pp. 11426–11440, Aug. 2020, doi: 10.1039/D0TC02559C.

[105] H. Gong, X. Wang, M. Sun, Y. Zhang, Q. Ji, and Z. Zhang, “Tuning the Ferroelectric Phase Transition of P(VDF-TrFE) through a Simple Approach of Modification by Introducing Double Bonds,” *ACS Omega*, vol. 7, no. 47, pp. 42949–42959, Nov. 2022, doi: 10.1021/ACSOMEGA.2C05172.

[106] I. Urbanaviciute *et al.*, “Tuning the Ferroelectric Properties of Trialkylbenzene-1,3,5-tricarboxamide (BTA),” *Adv. Electron. Mater.*, vol. 3, no. 7, p. 1600530, Jul. 2017, doi: 10.1002/AELM.201600530.

[107] I. Urbanaviciute *et al.*, “Suppressing depolarization by tail substitution in an organic supramolecular ferroelectric,” *Phys. Chem. Chem. Phys.*, vol. 21, no. 4, pp. 2069–2079, Jan. 2019, doi: 10.1039/C8CP06315J.

[108] I. Urbanaviciute, M. Garcia-Iglesias, A. Gorbunov, E. W. Meijer, and M. Kemerink,

"Ferro- and ferrielectricity and negative piezoelectricity in thioamide-based supramolecular organic discotics," *Phys. Chem. Chem. Phys.*, vol. 25, no. 25, pp. 16930–16937, Jun. 2023, doi: 10.1039/D3CP00982C.

[109] N. M. Casellas *et al.*, "Resistive switching in an organic supramolecular semiconducting ferroelectric," *Chem. Commun.*, vol. 55, no. 60, pp. 8828–8831, Jul. 2019, doi: 10.1039/C9CC02466B.

[110] T. Johann, W. Xie, S. Roosta, M. Elstner, and M. Kemerink, "Theory for nonlinear conductivity switching in semiconducting organic ferroelectrics," *Phys. Chem. Chem. Phys.*, vol. 26, no. 27, pp. 18837–18846, Jul. 2024, doi: 10.1039/D4CP01632G.

[111] J. Harada *et al.*, "Directionally tunable and mechanically deformable ferroelectric crystals from rotating polar globular ionic molecules," *Nat. Chem. 2016 810*, vol. 8, no. 10, pp. 946–952, Jul. 2016, doi: 10.1038/nchem.2567.

[112] B. Dickens, E. Balizer, A. S. DeReggi, and S. C. Roth, "Hysteresis measurements of remanent polarization and coercive field in polymers," *J. Appl. Phys.*, vol. 72, no. 9, pp. 4258–4264, 1992, doi: 10.1063/1.352213.

[113] R. S. Pease and G. E. Bacon, "Ferroelectric Structure of Potassium Dihydrogen Phosphate," *Nat. 1954 1734401*, vol. 173, no. 4401, pp. 443–444, 1954, doi: 10.1038/173443b0.

[114] G. A. Samara, "The effects of deuteration on the static ferroelectric properties of kh2p04 (kdp)," *Ferroelectrics*, vol. 5, no. 1, pp. 25–37, Jan. 1973, doi: 10.1080/00150197308235776.

[115] S. Horiuchi, K. Kobayashi, R. Kumai, and S. Ishibashi, "Proton tautomerism for strong polarization switching," *Nat. Commun.*, vol. 8, pp. 1–9, 2017, doi: 10.1038/ncomms14426.

[116] Y. Shimoi, S. Tsuzuki, R. Kumai, M. Sotome, and S. Horiuchi, "Competing ferroelectric polarization: hydroxyl flip-flop versus proton-transfer mechanisms," *J. Mater. Chem. C*, vol. 10, no. 27, pp. 10099–10105, Jul. 2022, doi: 10.1039/D2TC00233G.

[117] V. M. Fridkin and S. Ducharme, "General features of the intrinsic ferroelectric coercive field," *Phys. Solid State*, vol. 43, no. 7, pp. 1320–1324, Jul. 2001, doi: 10.1134/1.1386472/METRICS.

[118] S. Ducharme *et al.*, "Intrinsic Ferroelectric Coercive Field," *Phys. Rev. Lett.*, vol. 84, no. 1, p. 175, Jan. 2000, doi: 10.1103/PhysRevLett.84.175.

[119] J. L. Wang *et al.*, "Transition of the polarization switching from extrinsic to intrinsic in the ultrathin polyvinylidene fluoride homopolymer films," *Appl. Phys. Lett.*, vol. 104, no. 18, p. 182907, May 2014, doi: 10.1063/1.4875907/24129.

[120] E. Paramonova, V. Bystrov, X. Meng, H. Shen, J. Wang, and V. Fridkin, "Polarization Switching in 2D Nanoscale Ferroelectrics: Computer Simulation and Experimental Data Analysis," *Nanomater. 2020, Vol. 10, Page 1841*, vol. 10, no. 9, p. 1841, Sep. 2020, doi: 10.3390/NANO10091841.

[121] M. Mai, S. Ke, P. Lin, and X. Zeng, “Intrinsic and extrinsic effects on the ferroelectric switching of thin poly(vinylidene fluoride/trifluoroethylene) copolymer films,” *APL Mater.*, vol. 4, no. 4, Apr. 2016, doi: 10.1063/1.4947142/120823.

[122] F. Preisach, “Über die magnetische Nachwirkung,” *Zeitschrift für Phys.*, vol. 94, no. 5–6, pp. 277–302, May 1935, doi: 10.1007/BF01349418/METRICS.

[123] I. Urbanavičiūtė, T. D. Cornelissen, X. Meng, R. P. Sijbesma, and M. Kemerink, “Physical reality of the Preisach model for organic ferroelectrics,” *Nat. Commun. 2018 91*, vol. 9, no. 1, pp. 1–11, Oct. 2018, doi: 10.1038/s41467-018-06717-w.

[124] M. Avrami and A. Phys Lett, “Kinetics of Phase Change. II Transformation-Time Relations for Random Distribution of Nuclei,” *J. Chem. Phys.*, vol. 8, no. 2, pp. 212–224, Feb. 1940, doi: 10.1063/1.1750631.

[125] Y. Ishibashi and Y. Takagi, “Note on Ferroelectric Domain Switching,” *https://doi.org/10.1143/JPSJ.31.506*, vol. 31, no. 2, pp. 506–510, Aug. 1971, doi: 10.1143/JPSJ.31.506.

[126] S. Hashimoto, H. Orihara, and Y. Ishibashi, “Study on D-E Hysteresis Loop of TGS Based on the Avrami-Type Model,” *https://doi.org/10.1143/JPSJ.63.1601*, vol. 63, no. 4, pp. 1601–1610, Nov. 2013, doi: 10.1143/JPSJ.63.1601.

[127] A. K. Tagantsev, I. Stolichnov, N. Setter, J. S. Cross, and M. Tsukada, “Non-Kolmogorov-Avrami switching kinetics in ferroelectric thin films,” *Phys. Rev. B*, vol. 66, no. 21, p. 214109, Dec. 2002, doi: 10.1103/PhysRevB.66.214109.

[128] X. Du and I.-W. Chen, “Frequency Spectra of Fatigue of PZT and other Ferroelectric Thin Films,” *MRS Proc.*, vol. 493, no. 1, p. 311, Feb. 1997, doi: 10.1557/PROC-493-311.

[129] S. M. Nam, Y. B. Kil, S. Wada, and T. Tsurumi, “Domain Switching Kinetics of Lead Zirconate Titinate Thin Films,” *Japanese J. Appl. Physics, Part 2 Lett.*, vol. 42, no. 12 B, p. L1519, Dec. 2003, doi: 10.1143/JJAP.42.L1519/XML.

[130] D. Viehland and Y. H. Chen, “Random-field model for ferroelectric domain dynamics and polarization reversal,” *J. Appl. Phys.*, vol. 88, no. 11, pp. 6696–6707, Dec. 2000, doi: 10.1063/1.1325001.

[131] M. Vopsaroiu, J. Blackburn, M. G. Cain, and P. M. Weaver, “Thermally activated switching kinetics in second-order phase transition ferroelectrics,” *Phys. Rev. B - Condens. Matter Mater. Phys.*, vol. 82, no. 2, p. 024109, Jul. 2010, doi: 10.1103/PHYSREVB.82.024109/.

[132] M. Vopsaroiu, P. M. Weaver, M. G. Cain, M. J. Reece, and K. B. Chong, “Polarization Dynamics and Non-Equilibrium Switching Processes in Ferroelectrics,” *IEEE Trans. Ultrason. Ferroelectr. Freq. Control*, vol. 58, no. 9, pp. 1867–1873, 2011, doi: 10.1109/TUFFC.2011.2025.

[133] D. Antoniadis, T. Kim, and J. A. Del Alamo, “Nucleation-Limited Switching Dynamics Model for Efficient Ferroelectrics Circuit Simulation,” *IEEE Trans. Electron Devices*, vol. 69, no. 1, pp. 395–399, Jan. 2022, doi: 10.1109/TED.2021.3131290.

[134] R. Gross and A. Marx, “8 Energiebänder,” in *Festkörperphysik*, De Gruyter, 2022, pp. 317–370.

[135] J. L. Brédas, D. Beljonne, V. Coropceanu, and J. Cornil, “Charge-transfer and energy-transfer processes in π-conjugated oligomers and polymers: A molecular picture,” *Chem. Rev.*, vol. 104, no. 11, pp. 4971–5003, Nov. 2004, doi: 10.1021/CR040084K.

[136] V. Coropceanu, J. Cornil, D. A. da Silva Filho, Y. Olivier, R. Silbey, and J. L. Brédas, “Charge transport in organic semiconductors,” *Chem. Rev.*, vol. 107, no. 4, pp. 926–952, Apr. 2007, doi: 10.1021/CR050140X.

[137] N. Lu, L. Li, W. Banerjee, P. Sun, N. Gao, and M. Liu, “Charge carrier hopping transport based on Marcus theory and variable-range hopping theory in organic semiconductors,” *J. Appl. Phys.*, vol. 118, no. 4, p. 48, Jul. 2015, doi: 10.1063/1.4927334.

[138] A. Köhler and H. Bässler, “Electronic processes in organic semiconductors: An introduction,” *Electron. Process. Org. Semicond. An Introd.*, pp. 1–405, Mar. 2015, doi: 10.1002/9783527685172.

[139] H. Abdalla, “Charge and Energy Transport in Disordered Organic Semiconductors,” Linköping University, Linköping, Sweden, 2018.

[140] A. Miller and E. Abrahams, “Impurity Conduction at Low Concentrations,” *Phys. Rev.*, vol. 120, no. 3, p. 745, Nov. 1960, doi: 10.1103/PhysRev.120.745.

[141] R. A. Marcus, “Electron Transfer Reactions in Chemistry: Theory and Experiment (Nobel Lecture),” *Angew. Chemie Int. Ed. English*, vol. 32, no. 8, pp. 1111–1121, Aug. 1993, doi: 10.1002/ANIE.199311113.

[142] C. R. Crowell and S. M. Sze, “Current transport in metal-semiconductor barriers,” *Solid. State. Electron.*, vol. 9, no. 11–12, pp. 1035–1048, Nov. 1966, doi: 10.1016/0038-1101(66)90127-4.

[143] V. I. Arkhipov, U. Wolf, and H. Bässler, “Current injection from a metal to a disordered hopping system. II. Comparison between analytic theory and simulation,” *Phys. Rev. B*, vol. 59, no. 11, p. 7514, Mar. 1999, doi: 10.1103/PhysRevB.59.7514.

[144] D. M. Evans, V. Garcia, D. Meier, and M. Bibes, “Domains and domain walls in multiferroics,” *Phys. Sci. Rev.*, vol. 5, no. 9, Sep. 2020, doi: 10.1515/PSR-2019-0067.JPG.

[145] D. Meier and S. M. Selbach, “Ferroelectric domain walls for nanotechnology,” *Nat. Rev. Mater. 2021 73*, vol. 7, no. 3, pp. 157–173, Oct. 2021, doi: 10.1038/s41578-021-00375-z.

[146] A. V. Gorbunov *et al.*, “Ferroelectric self-assembled molecular materials showing both rectifying and switchable conductivity,” *Sci. Adv.*, vol. 3, no. 9, 2017, doi: 10.1126/SCIADV.1701017.

[147] H. Mager *et al.*, “Long-range electrical conductivity in non-π-conjugated organic molecular materials,” Jun. 2025, Accessed: Jun. 04, 2025. [Online]. Available:

https://arxiv.org/abs/2506.02673v1.

[148] M. Kemerink, K. Asadi, P. W. M. Blom, and D. M. De Leeuw, “The operational mechanism of ferroelectric-driven organic resistive switches,” *Org. Electron.*, vol. 13, no. 1, pp. 147–152, Jan. 2012, doi: 10.1016/J.ORGEL.2011.10.013.

[149] H. T. Yi, T. Choi, S. G. Choi, Y. S. Oh, and S. W. Cheong, “Mechanism of the Switchable Photovoltaic Effect in Ferroelectric BiFeO3,” *Adv. Mater.*, vol. 23, no. 30, pp. 3403–3407, Aug. 2011, doi: 10.1002/ADMA.201100805.

[150] V. Khikhlovskyi, R. Wang, A. J. J. M. Van Breemen, G. H. Gelinck, R. A. J. Janssen, and M. Kemerink, “Nanoscale organic ferroelectric resistive switches,” *J. Phys. Chem. C*, vol. 118, no. 6, pp. 3305–3312, Feb. 2014, doi: 10.1021/JP409757M/SUPPL_FILE/JP409757M_SI_001.PDF.

[151] T. Cornelissen, “Switching Kinetics and Charge Transport in Organic Ferroelectrics,” 2020.

[152] J. H. Christie, S. H. Krenek, and I. M. Woodhead, “The electrical properties of hygroscopic solids,” *Biosyst. Eng.*, vol. 102, no. 2, pp. 143–152, Feb. 2009, doi: 10.1016/J.BIOSYSTEMSENG.2008.09.023.

[153] J. H. Christie and I. M. Woodhead, “A New Model of DC Conductivity of Hygroscopic Solids,” *Text. Res. J.*, vol. 72, no. 3, pp. 273–278, 2002, doi: 10.1177/004051750207200315.

[154] C. E. Mortimer and U. Müller, “13 Strukturaufklärung,” in *Chemie: Das Basiswissen der Chemie*, Georg Thieme Verlag, 2020.

[155] D. C. Ailion, “Conventional Relaxation Time Methods,” in *Methods in Experimental Physics*, vol. 21, no. C, 1983, pp. 441–453.

[156] Y. Matsuo, J. Hatori, Y. Yoshida, and S. Ikehata, “Humidity dependence of proton conductivity in DNA film studied by NMR and AC conductivity,” *J. Phys. Soc. Japan*, vol. 79, no. SUPPL. A, pp. 12–14, 2010, doi: 10.1143/JPSJS.79SA.12.

[157] N. Domingo, E. Pach, K. Cordero-Edwards, V. Pérez-Dieste, C. Escudero, and A. Verdaguer, “Water adsorption, dissociation and oxidation on SrTiO 3 and ferroelectric surfaces revealed by ambient pressure X-ray photoelectron spectroscopy,” *Phys. Chem. Chem. Phys.*, vol. 21, no. 9, pp. 4920–4930, Feb. 2019, doi: 10.1039/C8CP07632D.

[158] I. Spasojevic, A. Verdaguer, G. Catalan, and N. Domingo, “Effect of Humidity on the Writing Speed and Domain Wall Dynamics of Ferroelectric Domains,” *Adv. Electron. Mater.*, vol. 8, no. 6, p. 2100650, Jun. 2022, doi: 10.1002/AELM.202100650.

[159] Y. Huang, J. L. Gottfried, A. Sarkar, G. Zhang, H. Lin, and S. Ren, “Proton-controlled molecular ionic ferroelectrics,” *Nat. Commun. 2023 141*, vol. 14, no. 1, pp. 1–8, Aug. 2023, doi: 10.1038/s41467-023-40825-6.

[160] J. Yanagisawa *et al.*, “Strongly Enhanced Polarization in a Ferroelectric Crystal by Conduction-Proton Flow,” *J. Am. Chem. Soc.*, vol. 146, no. 2, pp. 1476–1483, Jan.

2024, doi: 10.1021/JACS.3C10841/ASSET/IMAGES/LARGE/JA3C10841_0005.JPEG.

[161] S. Horiuchi, R. Kumai, and Y. Tokura, “High-temperature and pressure-induced ferroelectricity in hydrogen-bonded supramolecular crystals of anilic acids and 2,3-Di(2-pyridinyl)pyrazine,” *J. Am. Chem. Soc.*, vol. 135, no. 11, pp. 4492–4500, Mar. 2013, doi: 10.1021/JA400318V/SUPPL_FILE/JA400318V_SI_009.CIF.

[162] M. Fukunaga and Y. Noda, “New Technique for Measuring Ferroelectric and Antiferroelectric Hysteresis Loops,” *https://doi.org/10.1143/JPSJ.77.064706*, vol. 77, no. 6, May 2008, doi: 10.1143/JPSJ.77.064706.

[163] D. Damjanovic, “Ferroelectric, dielectric and piezoelectric properties of ferroelectric thin films and ceramics,” *Reports Prog. Phys.*, vol. 61, no. 9, p. 1267, Sep. 1998, doi: 10.1088/0034-4885/61/9/002.

[164] Indre Urbanaviciute et al, “Negative piezoelectric effect in an organic supramolecular ferroelectric,” *Mater. Horizons*, vol. 6, pp. 1688–1698, 2019, doi: 10.1039/C9MH00094A.

[165] F. Peter, A. Rüdiger, and R. Waser, “Mechanical crosstalk between vertical and lateral piezoresponse force microscopy,” *Rev. Sci. Instrum.*, vol. 77, no. 3, p. 036103, Mar. 2006, doi: 10.1063/1.2176081.

[166] R. K. Vasudevan, N. Balke, P. Maksymovych, S. Jesse, and S. V. Kalinin, “Ferroelectric or non-ferroelectric: Why so many materials exhibit ‘ferroelectricity’ on the nanoscale,” *Appl. Phys. Rev.*, vol. 4, no. 2, Jun. 2017, doi: 10.1063/1.4979015.

[167] D. Seol, B. Kim, and Y. Kim, “Non-piezoelectric effects in piezoresponse force microscopy,” *Curr. Appl. Phys.*, vol. 17, no. 5, pp. 661–674, May 2017, doi: 10.1016/J.CAP.2016.12.012.

[168] N. Balke *et al.*, “Differentiating Ferroelectric and Nonferroelectric Electromechanical Effects with Scanning Probe Microscopy,” *ACS Nano*, vol. 9, no. 6, pp. 6484–6492, Jun. 2015, doi: 10.1021/ACSNANO.5B02227.

[169] B. Kim, D. Seol, S. Lee, H. N. Lee, and Y. Kim, “Ferroelectric-like hysteresis loop originated from non-ferroelectric effects,” *Appl. Phys. Lett.*, vol. 109, no. 10, p. 102901, Sep. 2016, doi: 10.1063/1.4962387.

[170] B. Ohler, A. Labuda, J. Li, and J. Lefever, “Interferometric AFM: redefining atomic force microscopy - 2024 - Wiley Analytical Science.”

[171] R. W. Boyd, “The Nonlinear Optical Susceptibility,” in *Nonlinear Optics*, 2020, pp. 1–64.

[172] Y. Yang, H. Sai, S. A. Egner, R. Qiu, L. C. Palmer, and S. I. Stupp, “Peptide programming of supramolecular vinylidene fluoride ferroelectric phases,” *Nat. 2024 6348035*, vol. 634, no. 8035, pp. 833–841, Oct. 2024, doi: 10.1038/s41586-024-08041-4.

[173] K. Norrman, A. Ghanbari-Siahkali, and N. B. Larsen, “6 Studies of spin-coated polymer films,” *Annu. Reports Sect. “C” (Physical Chem.*, vol. 101, no. 0, pp. 174–201, Oct. 2005, doi: 10.1039/B408857N.

[174] “Interdigitated Electrodes (IDE) | MicruX.” https://www.micruxfluidic.com/product/interdigitated-electrodes-ide/ (accessed Sep. 15, 2025).

[175] R. Nigon, T. M. Raeder, and P. Muralt, “Characterization methodology for lead zirconate titanate thin films with interdigitated electrode structures,” *J. Appl. Phys.*, vol. 121, no. 20, p. 14, May 2017, doi: 10.1063/1.4983772/153690.

[176] M. W. Den Otter, “Approximate expressions for the capacitance and electrostatic potential of interdigitated electrodes,” *Sensors Actuators A Phys.*, vol. 96, no. 2–3, pp. 140–144, Feb. 2002, doi: 10.1016/S0924-4247(01)00783-X.

[177] G. W. Farnell, P. Silvester, S. K. Wong, and I. A. Cermak, “Capacitance and Field Distributions for Interdigital Surface-Wave Transducers,” *IEEE Trans. Sonics Ultrason.*, vol. SU-17, no. 3, pp. 188–195, 1970, doi: 10.1109/T-SU.1970.29560.

[178] N. J. Kidner, A. Meier, Z. J. Homrighaus, B. W. Wessels, T. O. Mason, and E. J. Garboczi, “Complex electrical (impedance/dielectric) properties of electroceramic thin films by impedance spectroscopy with interdigital electrodes,” *Thin Solid Films*, vol. 515, no. 11, pp. 4588–4595, Apr. 2007, doi: 10.1016/J.TSF.2006.11.038.

[179] M. Litterst, “Dielectric spectroscopy of potentially ferroelectric molecules,” Heidelberg, 2022.

[180] C. Multiphysics, “Modeling Resistive and Capacitive Devices in COMSOL®.” https://www.comsol.de/video/modeling-resistive-and-capacitive-devices-in-comsol (accessed Sep. 15, 2025).

[181] “HFS600E-PB4 - Temperature control from -195 to 600°C with probes and electrical connections — Linkam Scientific.” https://www.linkam.co.uk/hfs600e-pb4 (accessed Sep. 17, 2025).

[182] “M 5504 Compact Glovebox | Temperature and Humidity Control.” https://www.electrotechsystems.com/shop/m-5504-compact-temperature-and-humidity-control-glovebox/ (accessed Sep. 17, 2025).

[183] “MFIA 500 kHz / 5 MHz Impedanz-Analysator | Zurich Instruments.” https://www.zhinst.com/europe/de/products/mfia-impedance-analyzer (accessed Sep. 17, 2025).

[184] “TF 2000 E | aixACCT Systems.” https://www.aixacct.com/en/testsysteme/tf-analyzer-family/tf-analyzer-2000-e/ (accessed Sep. 17, 2025).

[185] “aixDBLI - Dünnschichten charakterisieren.” https://www.aixacct.com/testsysteme/systemloesungen/aixdbli/ (accessed Sep. 17, 2025).

[186] D. A. Jacobs *et al.*, “Hysteresis phenomena in perovskite solar cells: the many and varied effects of ionic accumulation,” *Phys. Chem. Chem. Phys.*, vol. 19, no. 4, pp. 3094–3103, Jan. 2017, doi: 10.1039/C6CP06989D.

[187] A. Czapik and M. Gdaniec, “Cocrystals of 2,3,5,6-tetra-fluoro-benzene-1,4-diol with

diaza aromatic compounds," *Acta Crystallogr. Sect. C Cryst. Struct. Commun.*, vol. 66, no. 7, pp. o356–o360, Jun. 2010, doi: 10.1107/S0108270110021736/HTTPS://JOURNALS.IUCR.ORG/SERVICES/RSS.HTML.

[188] Z. Zikmund *et al.*, "Search for new molecular organic ferroelectrics," *Ferroelectrics*, vol. 158, no. 1, pp. 223–228, Aug. 1994, doi: 10.1080/00150199408216020.

[189] S. Chandrasekhar and S. Mukherjee, "Salts of hexamethylenetetramine with organic acids: Enhanced anomeric interactions with a lowering of molecular symmetry revealed by crystal structures," *J. Mol. Struct.*, vol. 1082, pp. 188–194, Feb. 2015, doi: 10.1016/J.MOLSTRUC.2014.11.013.

[190] A. Katrusiak and A. Katrusiak, "Crystal-stabilisation of an elusive 4,6-pyrimidinedione dimer," *Tetrahedron Lett.*, vol. 48, no. 11, pp. 1935–1938, Mar. 2007, doi: 10.1016/J.TETLET.2007.01.096.

[191] E. Fluck and W. Schwarz, "NH4BF4 (CH2)N4," *Zeitschrift für Anorg. und Allg. Chemie*, vol. 444, no. 1, pp. 121–124, Sep. 1978, doi: 10.1002/ZAAC.19784440114.

[192] C. S. Yang *et al.*, "Exceptional second harmonic generation responses, switchable dielectric behaviours, and ferroelectric property in an adduct of hexamethylene-tetramine·bisnopinic acid," *Chem. Phys.*, vol. 502, pp. 66–71, Mar. 2018, doi: 10.1016/J.CHEMPHYS.2018.01.014.

[193] S. Aldridge *et al.*, "Structures and aggregation of the methylamine-borane molecules, Me nH3-nN BH3 (n = 1-3), studied by X-ray diffraction, gas-phase electron diffraction, and quantum chemical calculations," *J. Am. Chem. Soc.*, vol. 131, no. 6, pp. 2231–2243, Feb. 2009, doi: 10.1021/JA807545P.

[194] S. Geller, R. E. Hughes, and J. L. Hoard, "Note on the crystalline structure of trimethylamine–borine, (H3C)3N–BH3," *urn:issn:0365-110X*, vol. 4, no. 4, pp. 380–380, Jul. 1951, doi: 10.1107/S0365110X51001215.

[195] A. Mondal *et al.*, "Metal-like Ductility in Organic Plastic Crystals: Role of Molecular Shape and Dihydrogen Bonding Interactions in Aminoboranes," *Angew. Chemie Int. Ed.*, vol. 59, no. 27, pp. 10971–10980, Jun. 2020, doi: 10.1002/ANIE.202001060.

[196] Y. Zhang *et al.*, "Harnessing Plasticity in an Amine-Borane as a Piezoelectric and Pyroelectric Flexible Film," *Angew. Chemie Int. Ed.*, vol. 59, no. 20, pp. 7808–7812, May 2020, doi: 10.1002/ANIE.202001798.

[197] A. Katrusiak and A. Katrusiak, "Ionic disparity of identical molecules in polymorphs," *Org. Lett.*, vol. 5, no. 11, pp. 1903–1905, May 2003, doi: 10.1021/OL034494R.

[198] S. W. Kennedy, P. K. Schultz, P. G. Slade, and E. R. T. Tiekink, "Triethylenediamine dihydrochloride," *Zeitschrift für Krist. - Cryst. Mater.*, vol. 180, no. 1–4, pp. 211–218, Nov. 1987, doi: 10.1524/ZKRI.1987.180.14.211.

[199] L. Jin, F. Li, and S. Zhang, "Decoding the Fingerprint of Ferroelectric Loops: Comprehension of the Material Properties and Structures," *J. Am. Ceram. Soc.*, vol. 97, no. 1, pp. 1–27, Jan. 2014, doi: 10.1111/JACE.12773.

[200] P. W. M. Blom, R. M. Wolf, J. F. M. Cillessen, and M. P. C. M. Krijn, “Ferroelectric Schottky diode,” *Phys. Rev. Lett.*, vol. 73, no. 15, pp. 2107–2110, Oct. 1994, doi: 10.1103/PhysRevLett.73.2107.

[201] D. Bolten, U. Böttger, and R. Waser, “Reversible and irreversible polarization processes in ferroelectric ceramics and thin films,” *J. Appl. Phys.*, vol. 93, no. 3, pp. 1735–1742, Feb. 2003, doi: 10.1063/1.1535748.

[202] S. Mantri, J. Oddershede, D. Damjanovic, and J. E. Daniels, “Ferroelectric domain continuity over grain boundaries,” *Acta Mater.*, vol. 128, pp. 400–405, Apr. 2017, doi: 10.1016/J.ACTAMAT.2017.01.065.

[203] S. Seyedraoufi and K. Berland, “Improved proton-transfer barriers with van der Waals density functionals: Role of repulsive non-local correlation,” *J. Chem. Phys.*, vol. 156, no. 24, p. 244106, Jun. 2022, doi: 10.1063/5.0095128/2841341.

[204] F. Zhuo *et al.*, “Perspective on antiferroelectrics for energy storage and conversion applications,” *Chinese Chem. Lett.*, vol. 32, no. 7, pp. 2097–2107, Jul. 2021, doi: 10.1016/J.CCLET.2020.11.070.

[205] C. A. Randall, Z. Fan, I. Reaney, L. Q. Chen, and S. Trolier-McKinstry, “Antiferroelectrics: History, fundamentals, crystal chemistry, crystal structures, size effects, and applications,” *J. Am. Ceram. Soc.*, vol. 104, no. 8, pp. 3775–3810, Aug. 2021, doi: 10.1111/JACE.17834.

[206] N. Bar-Chaim *et al.*, “Electric field dependence of the dielectric constant of PZT ferroelectric ceramics,” *J. Appl. Phys.*, vol. 45, no. 6, pp. 2398–2405, Jun. 1974, doi: 10.1063/1.1663605.

[207] H. Bässler, “Charge Transport in Disordered Organic Photoconductors a Monte Carlo Simulation Study,” *Phys. status solidi*, vol. 175, no. 1, pp. 15–56, Jan. 1993, doi: 10.1002/PSSB.2221750102.

[208] B. Rennekamp *et al.*, “Collagen breaks at weak sacrificial bonds taming its mechanoradicals,” *Nat. Commun. 2023 141*, vol. 14, no. 1, pp. 2075-, Apr. 2023, doi: 10.1038/s41467-023-37726-z.

[209] E. Dypvik Sødahl, J. Carrete, G. K. H. Madsen, and K. Berland, “Dynamical Disorder in the Mesophase Ferroelectric HdabcoClO4: A Machine-Learned Force Field Study,” *J. Phys. Chem. C*, vol. 129, no. 1, pp. 484–494, Jan. 2025, doi: 10.1021/ACS.JPCC.4C06615.

[210] H. Tian, X. Li, and I. Burda, “Virtual Quartz Crystal Microbalance: Bioinspired Resonant Frequency Tracking,” *Biomimetics 2022, Vol. 7, Page 156*, vol. 7, no. 4, p. 156, Oct. 2022, doi: 10.3390/BIOMIMETICS7040156.

[211] M. Li *et al.*, “Revisiting the δ-phase of poly(vinylidene fluoride) for solution-processed ferroelectric thin films,” *Nat. Mater. 2013 125*, vol. 12, no. 5, pp. 433–438, Mar. 2013, doi: 10.1038/nmat3577.

[212] M. Yuan *et al.*, “Enhancing the Alpha-To-Gamma Phase Transition of Poly(vinylidene fluoride) via Dehydrofluorination Modification,” *Cryst. Growth Des.*, vol. 24, no. 3, pp.

1485–1494, Feb. 2024, doi: 10.1021/ACS.CGD.3C01431/ASSET/IMAGES/LARGE/CG3C01431_0008.JPEG.

[213] V. Srinivasan and D. Sebastiani, “The isotope-effect in the phase transition of KH2PO4: New insights from Ab initio path-integral simulations,” *J. Phys. Chem. C*, vol. 115, no. 25, pp. 12631–12635, Jun. 2011, doi: 10.1021/JP202584P/ASSET/IMAGES/LARGE/JP-2011-02584P_0003.JPEG.

[214] K. M. Rabe, M. Dawber, C. Lichtensteiger, C. H. Ahn, and J. M. Triscone, “Modern Physics of Ferroelectrics: Essential Background,” in *Topics in Applied Physics*, vol. 105, Springer, Berlin, Heidelberg, 2007, pp. 1–30.

[215] R. Gross and A. Marx, “Ferroelektrizität,” in *Festkörperphysik*, 2018, pp. 643–655.

[216] T. Miyamoto *et al.*, “Ultrafast polarization control by terahertz fields via π-electron wavefunction changes in hydrogen-bonded molecular ferroelectrics,” *Sci. Reports 2018 81*, vol. 8, no. 1, pp. 1–8, Oct. 2018, doi: 10.1038/s41598-018-33076-9.

[217] G. Schaumburg, “Novocontrol Introduces High Quality Low Cost Interdigitated Comb Electrodes,” *Dielectric newsletter 22*, pp. 5–7, 2006.

X. Appendix

A. Data empty IDEs

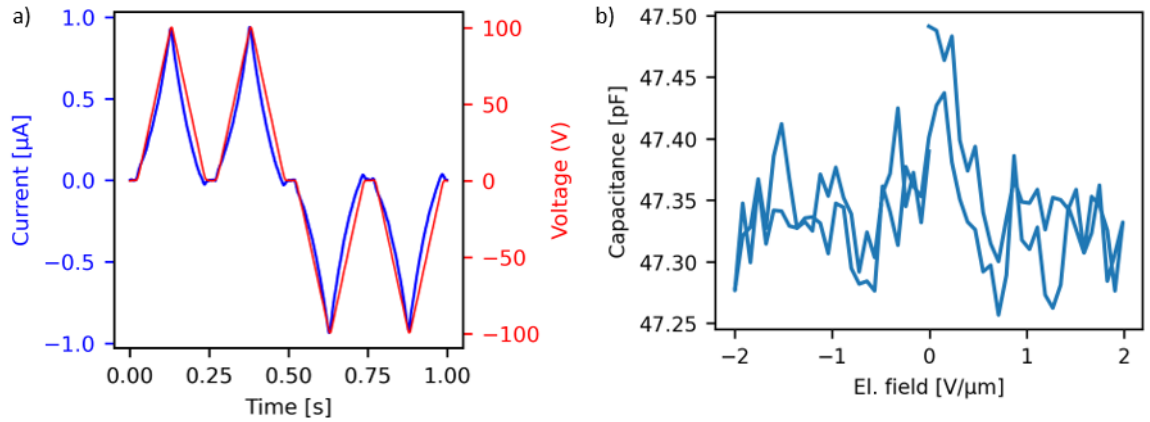

Appendix 1: a) DW and b) CV signal of an empty, homemade IDE

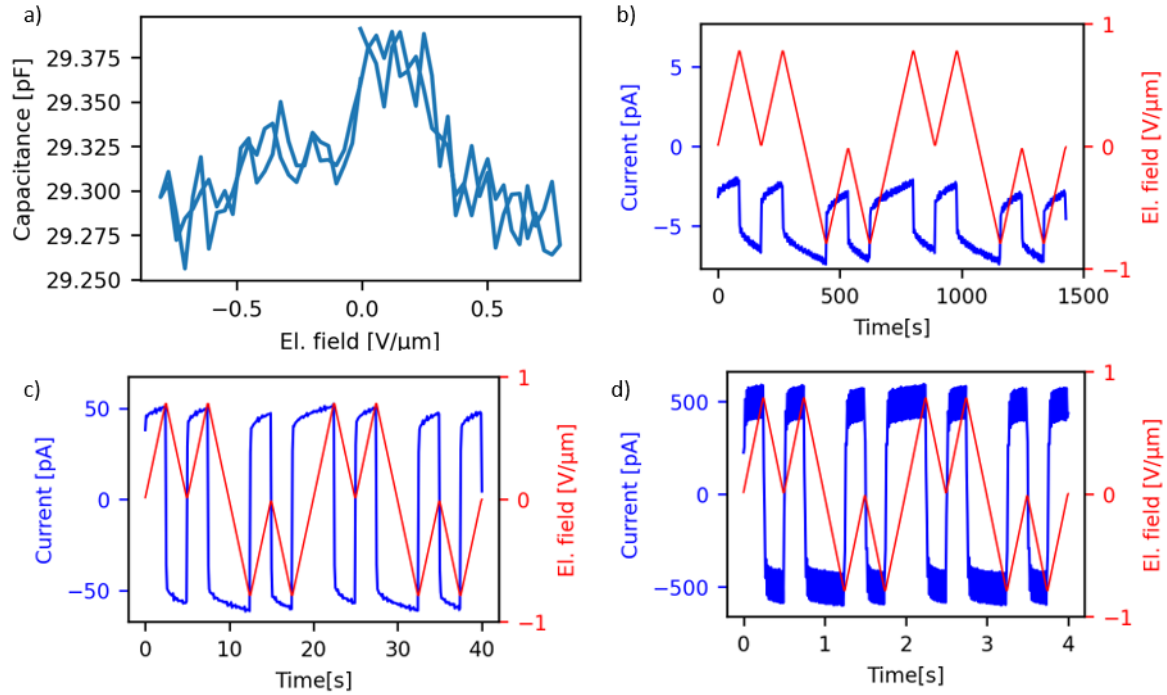

Appendix 2: a) CV of an empty MicruX IDE, b-d) Current response to the DWM Voltage at b) 0.7mHz, c) 25mHZ and d) 250mHz; The current sensor has an offset of about 4pA

B. Thickness measurements BTA

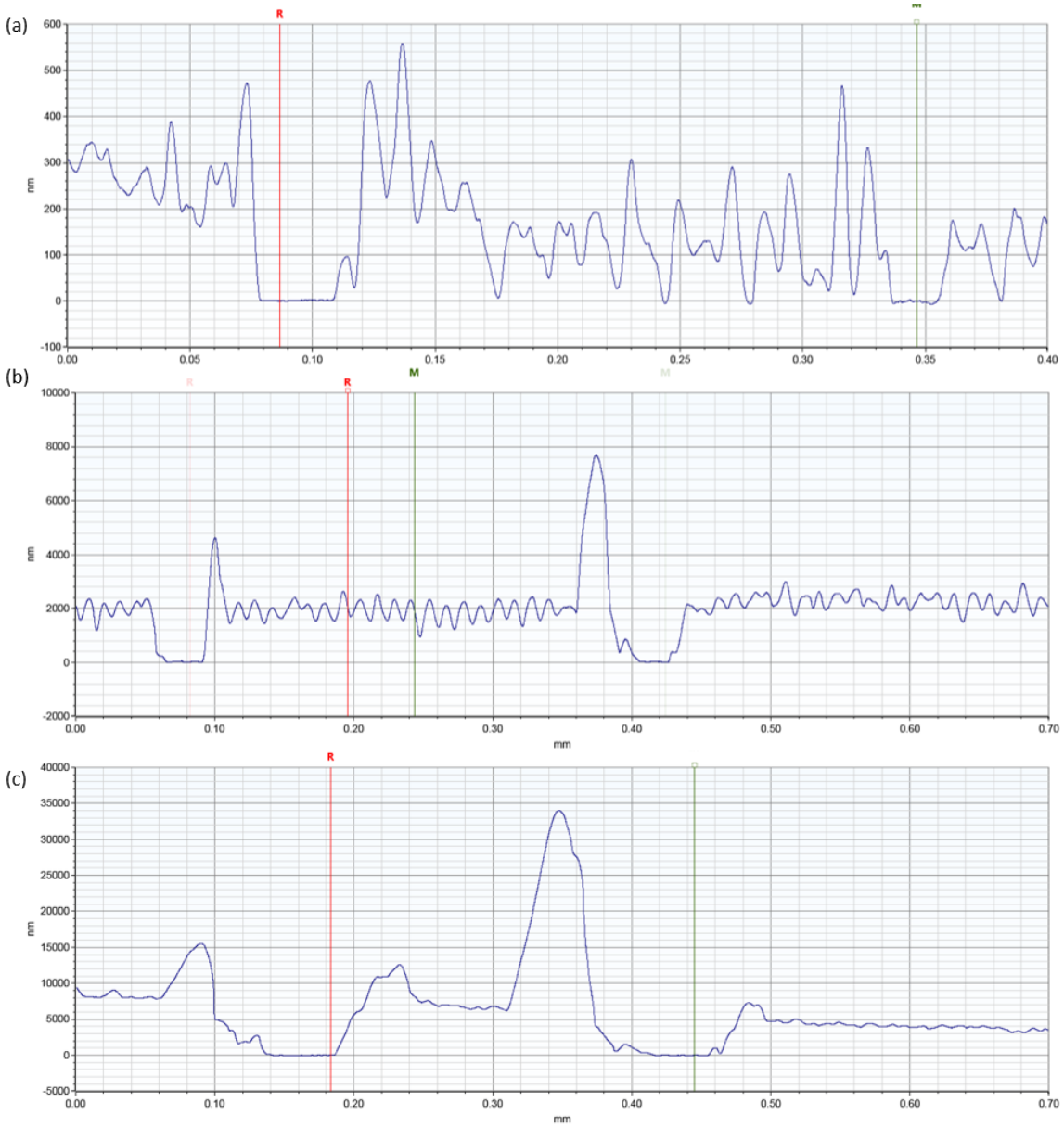

Appendix 3: Thickness of BTA-C10 samples; (a) 40mg/ml spin coated at 1000rpm showing a thickness of 100-200 nm; (b) 5µl of 10 mg/ml drop casted, showing a thickness of 2 µm; (c) 5µl of 40 mg/ml drop casted, showing a thickness of 5-7 µm. All measured were performed with a Dektak XT profilometer

C. Dielectric spectroscopy

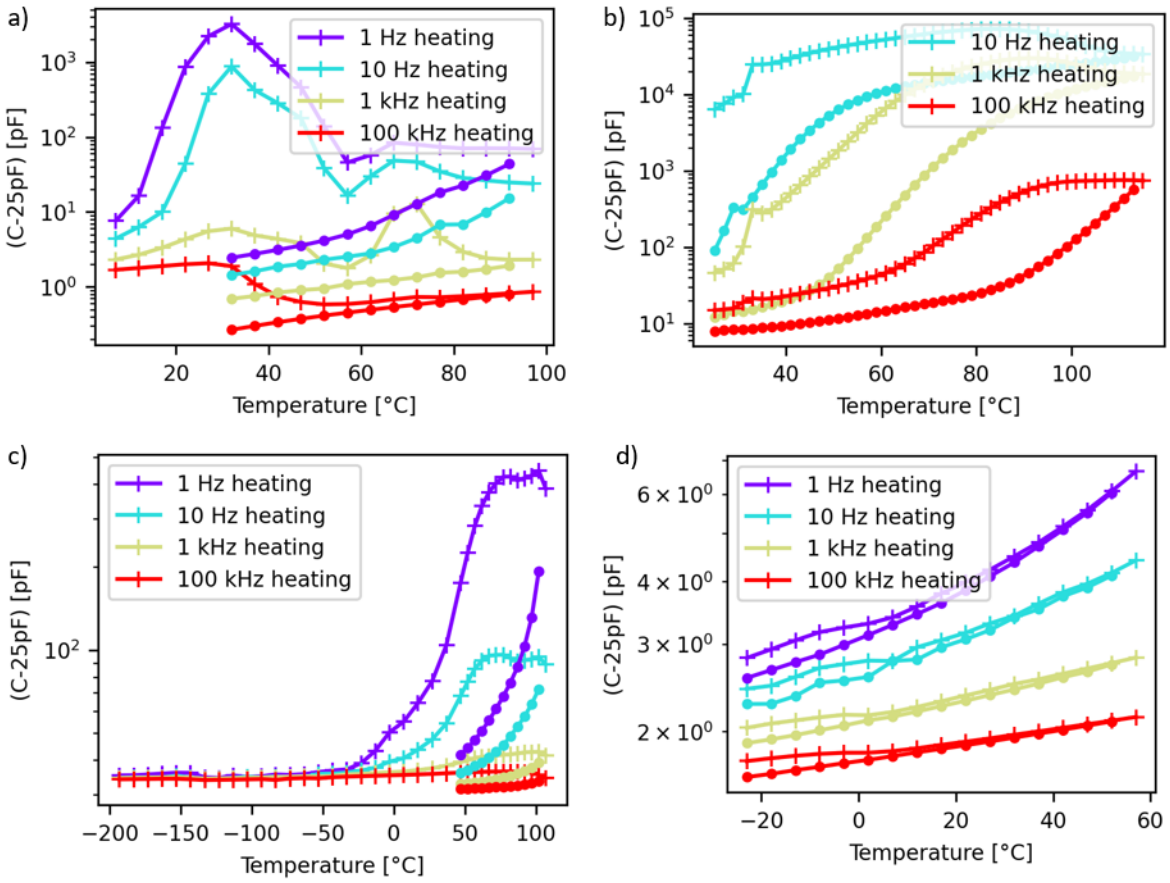

Appendix 4: Dielectric spectroscopy of different compounds; (a) ***material 1*** *in vacuum; (b)* ***material 1*** *in air; (c)* ***material 2*** *in vacuum; (d)* ***material 4*** *in vacuum; dotted data shows the measurement for cooling after the initial heating.*

Dielectric spectroscopy data of **material 1**,**2** and **4** is plotted in Appendix 4. For **material 1**, the results showed strong variations. While the measurements in vacuum (Appendix 4 (a)) show peaks around 35 °C and 70 °C, which could not be reproduced in air (Appendix 4(b)). In vacuum, these peaks only appear when heating first, afterwards the capacitance is much smaller. This can be explained by crystal water remaining in the material even when evacuating the chamber which only gets removed when heating up sufficiently. This does not easily explain why there are peaks at certain temperatures but as this does not appear to be an intrinsic material property and was not observable under ambient conditions and did not affect the ferroelectric properties, this phenomenon was not further investigated. The fact that the cooling line in Appendix 4(b) does not match the heating curve can be explained by material degradation as the color of the material also changed during the measurement. The measurements for **material 2** are shown in Appendix 4 (c). While there is an increase when heating above room temperature, the decrease when cooling is much faster. For this reason, the increase is attributed to thermally mobilized dipoles and the decrease to material degradation. The data for **material 4** ((Appendix 4 (d)) does not show any relevant peaks which indicate any phase transition. As **material 3** already sublimates at room temperature, it was

not possible to make any measurements in vacuum or with any heating, so there were no dielectric spectroscopy measurements performed.

D. Data material1

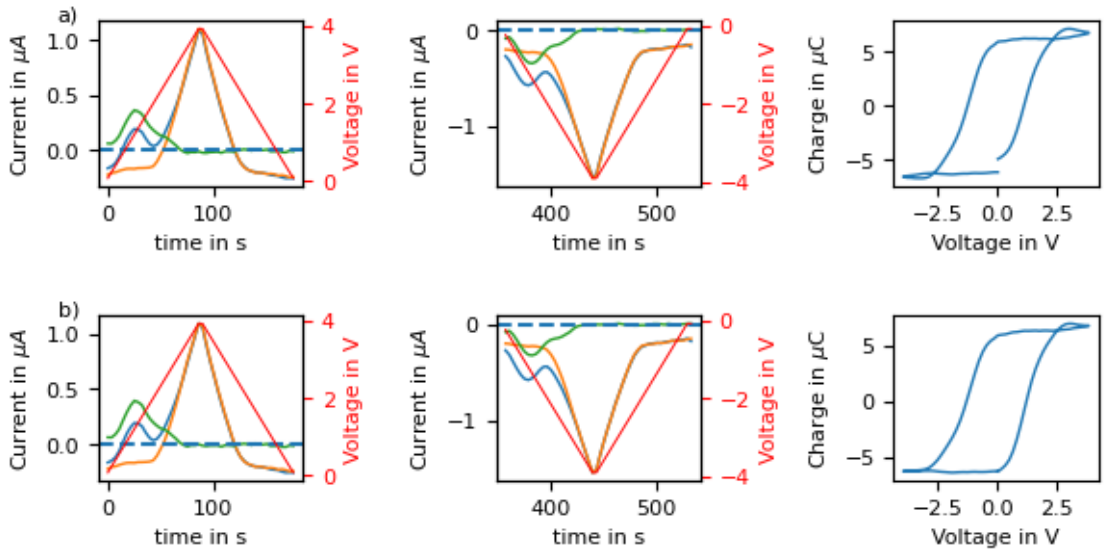

Appendix 5: a) raw data for material 1, measured at 0.7 mHz, evaluated to the original double wave method [162], *b) data modified according to chapter III.C.1; As a) shows the raw data, the voltage is shown, while for b), the voltage is converted to the electric field (see III.A.2); the blue curve shows the current in the first voltage pulse, the orange the current in the second voltage pulse and green the difference between the two. Red shows the applied voltage.*

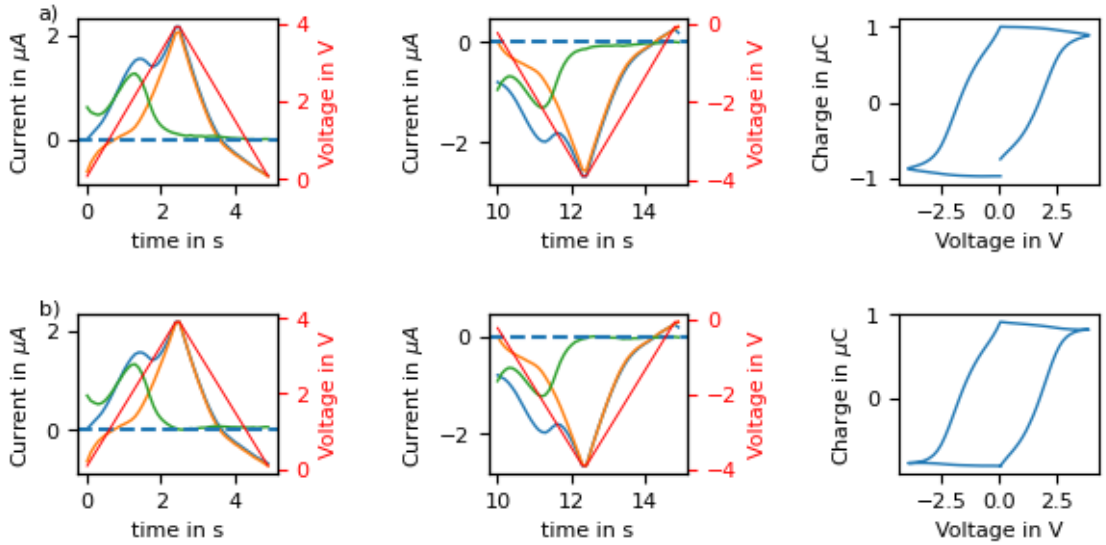

Appendix 6: a) raw data for material 1, measured at 25 mHz, b) data modified according our evaluation method (chapter III.C.1), same color coding as in Appendix 5

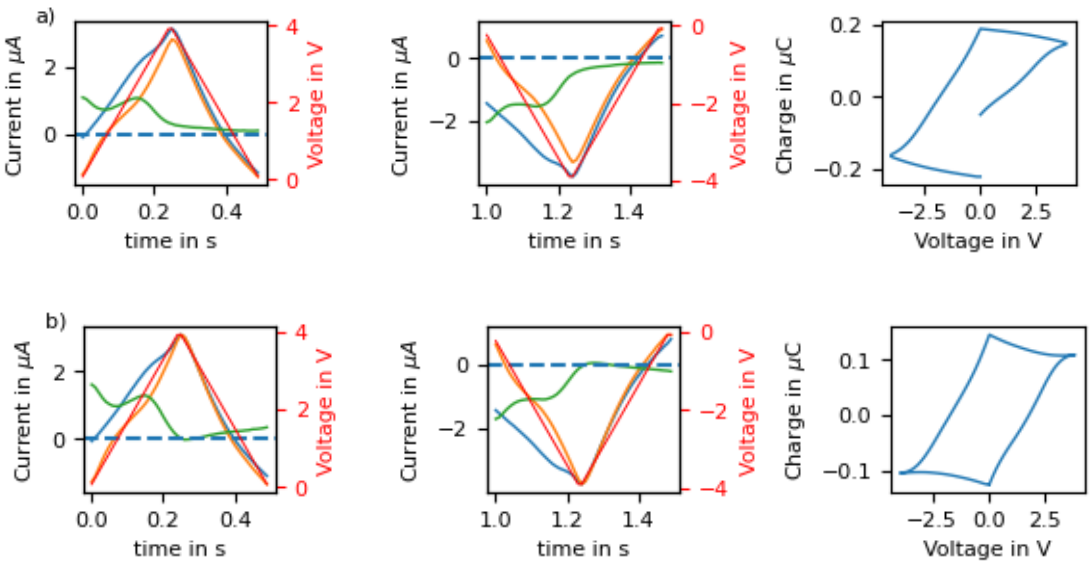

Appendix 7: a) raw data for material 1, measured at 250 mHz b) data modified according our evaluation method (chapter III.C.1), same color coding as in Appendix 5

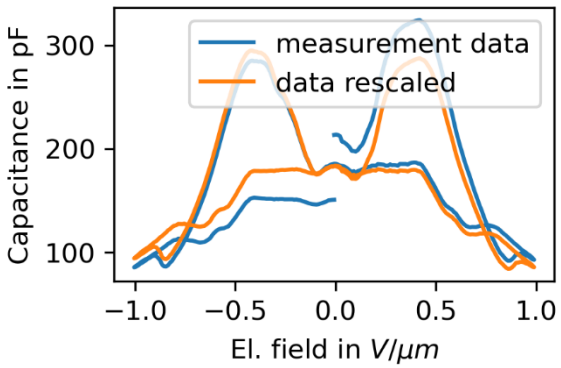

Appendix 8: CV measurement for material 1, raw data in orange, blue shows the data rescaled according to III.C.2

E. Explanation of sharp edges

For the hysteresis curve shown in Appendix 6, as well as in Appendix 10 for **material 2**, there appear sharp edges at 0 V. This is an artifact of the missing flat space between the two voltage pulses:

The core assumption of the DWM is that both voltage waves induce mostly the same currents, with only the ferroelectric switching current being different. While this is mostly true, there are deviations in the first couple datapoints due to the different voltage history (the first curve starts from opposite voltage, thus having positive displacement current, while the second pulse has the same voltage history and thus negative displacement current). This can be seen by the blue and orange curves in Fig. S4 having different starting currents at 0V, resulting in a noticeable difference (green). This is shown in more detail Appendix 9 where each datapoint is shown individually. The same cannot be said for the end of the voltage wave, where there has been the same history, resulting in the same current and therefore the difference (green) being very close to 0. The green curve of the two parts are combined and integrated for the hysteresis curve, resulting in the edge at 0V.

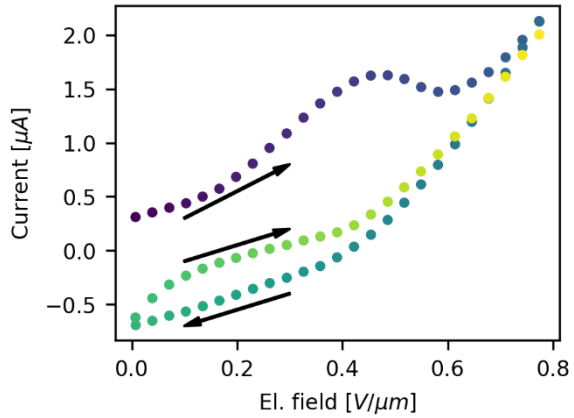

Appendix 9: Current vs. electric field for the double wave measurement of material 1 at 25 mHz (same data as Appendix 6)

F. Data material 2

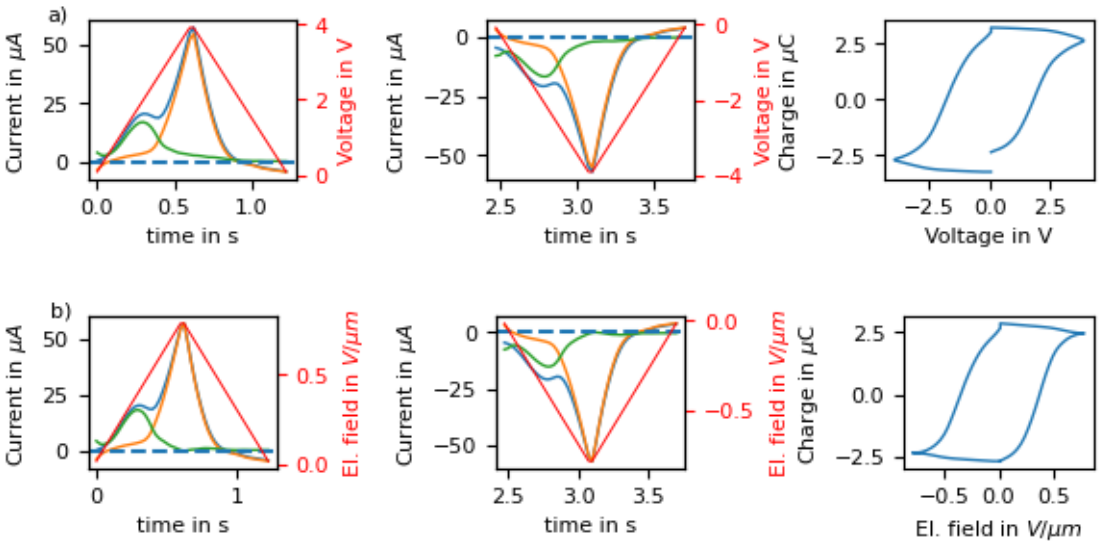

Appendix 10: a) raw data for material 2, measured at 100 mHz, mHz b) data modified according our evaluation method (chapter III.C.1), same color coding as in Appendix 5

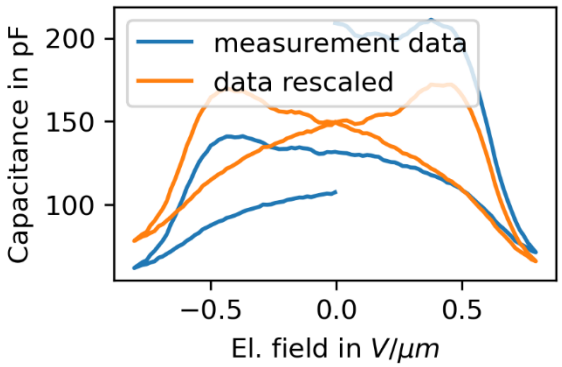

Appendix 11: CV measurement for material 2, raw data in orange, blue shows the data rescaled according to III.C.2

G. Data material 3

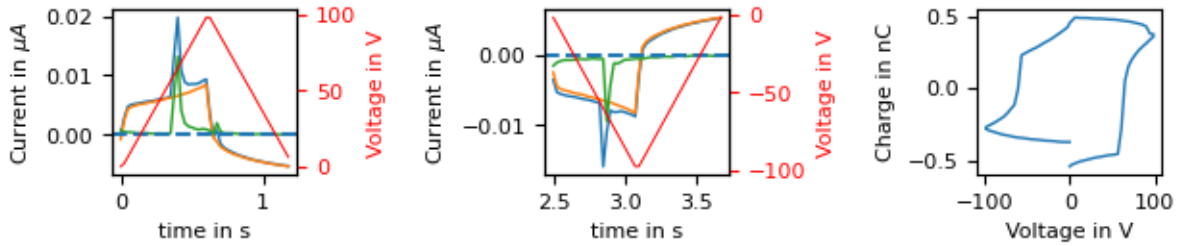

Appendix 12: raw data for material 3, measured at 100 mHz, the data is not evaluated according to (chapter III.C.1) as it the curve is not that of a typical ferroelectric, same color coding as in Appendix 5

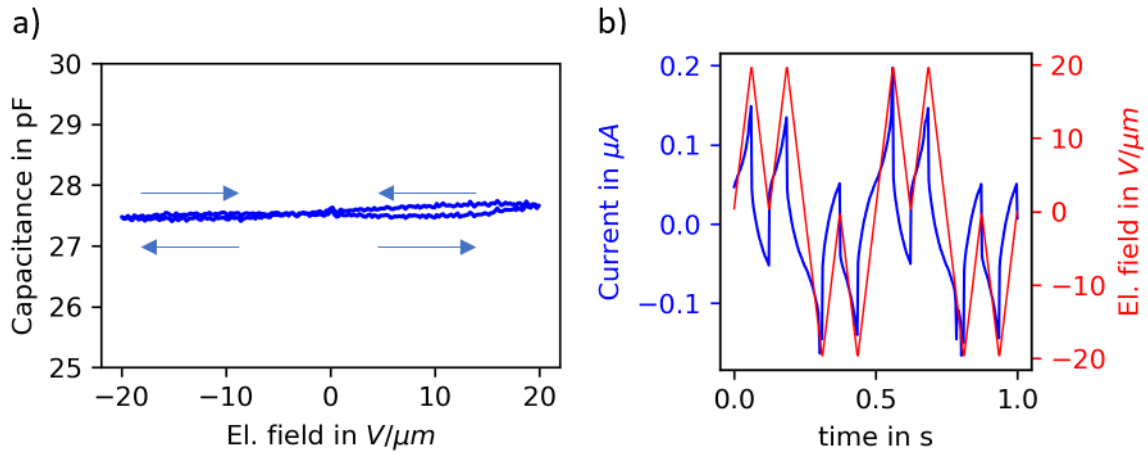

Appendix 13: a) Raw CV measurement for material 3 (same sample as in Appendix 12), arrows indicate the measurement direction; b) other sample, showing similar peaks in DW measurement

H. Data for material 4

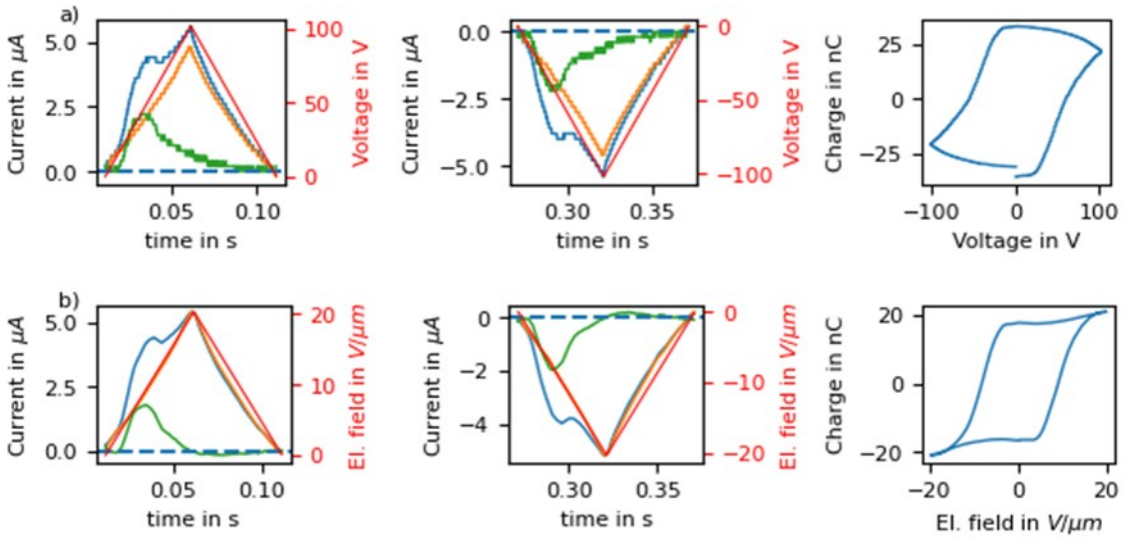

Appendix 16: a) raw data for material 4, measured at 2 Hz, b) data modified according our evaluation method (chapter III.C.1) and smoothed, same color coding as in Appendix 5.

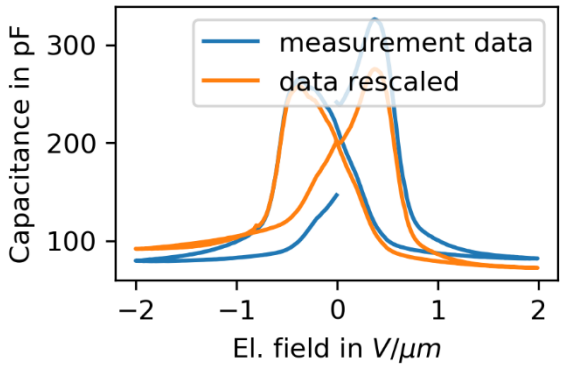

Appendix 15: CV measurement for normal behaving material 4, raw data in orange, blue shows the data rescaled according to III.C.2

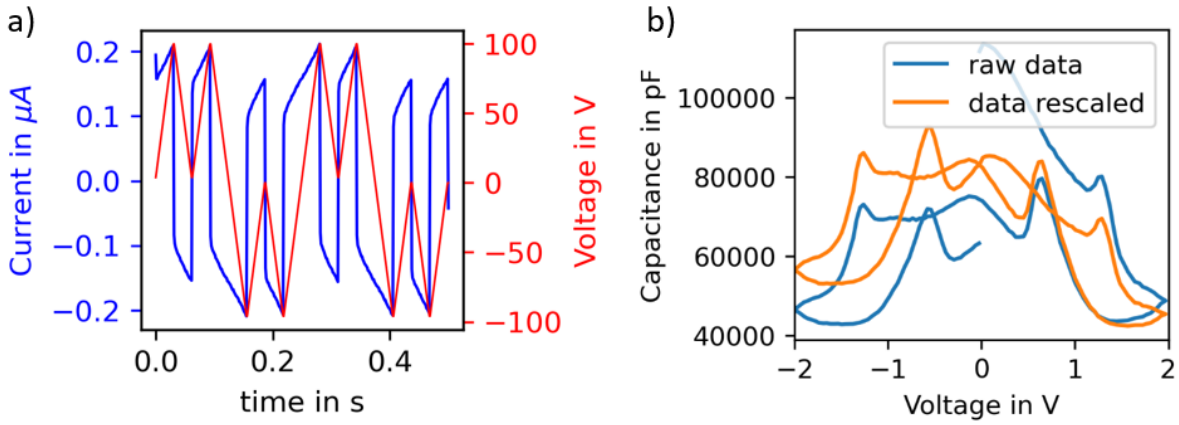

Appendix 14: a) DWM and b) CV measurement of strangely behaving material 4 samples, raw data in orange, blue shows the data rescaled according to III.C.2

I. Material 5 (VAGVAA)

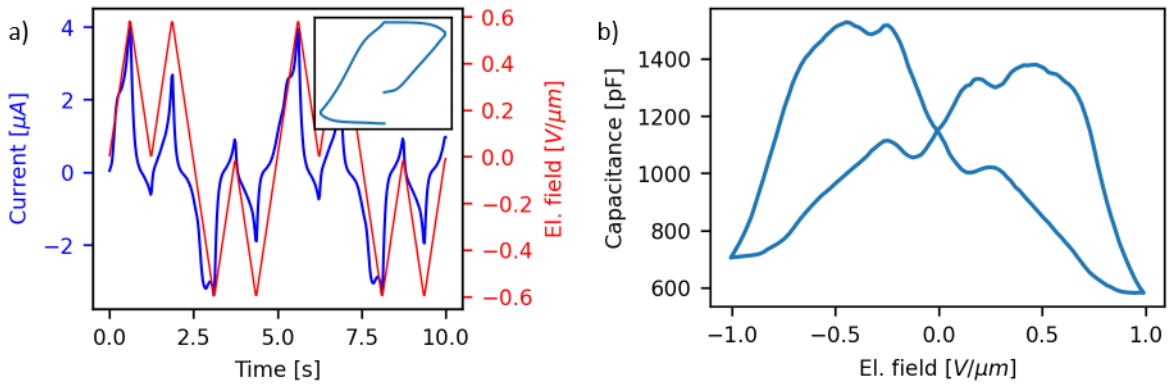

Appendix 17: (a) Double wave signal of material 5, inset shows the resulting, not-rescaled hysteresis curve; (b)Capacitance voltage curve of material 5, both measured at 258 K.

Material 5 was initially also included in the screening study. As already discussed for the XRD data, the measurements showed a different crystal structure than expected for the synthesis method. First ferroelectric measurements (with unfortunately unknown crystal structure), are however promising. The DW-measurement (Appendix 17 (a)) show distinctive shoulders in the first voltage wave which did not appear in the second wave. The background current in the first wave is also considerably higher than in the second curve which might be indicative of strong ionic hysteresis. Consequently, the hysteresis curve, plotted in the inset of Appendix 17**Fehler! Verweisquelle konnte nicht gefunden werden.** (a), is dominated by this non-ferroelectric hysteresis and does not show saturation above the coercive field. The CV curve is shown in Appendix 17 (b) and shows the typical butterfly shape. It also shows an interesting substructure. While not perfect, this data strongly suggest that the material is ferroelectric. As it was however not clear, which crystal structure lead to these results, the experiments were stopped at this point until a reliable crystallization process can be found.

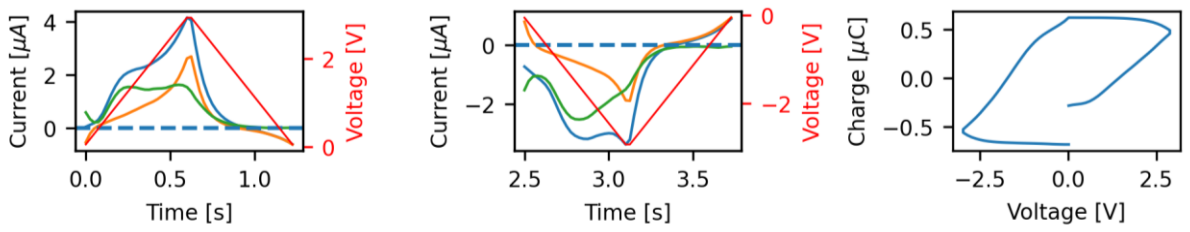

Appendix 18: raw data for material 5, measured at 100 mHz, 258 K. The rescaled data is omitted due to the large asymmetry between the two sides as well as the bad saturation of the curve

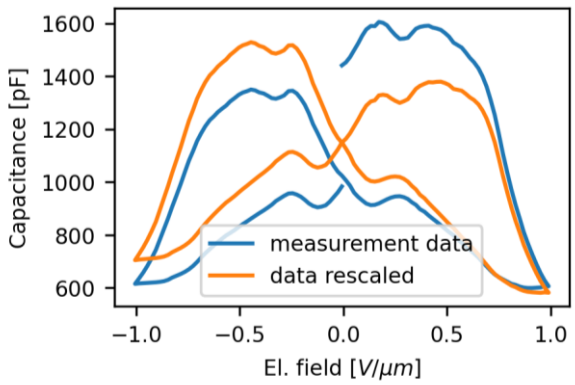

Appendix 19: CV measurement for material 5, raw data in orange, blue shows the data rescaled according to III.C.2

J. Coercive field fits

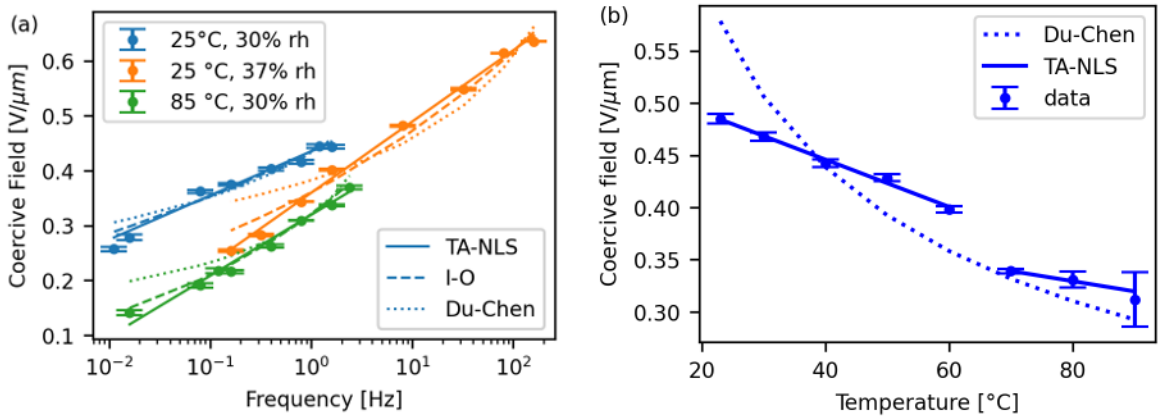

Appendix 20: a) Frequency dependent Coercive field at 25 °C and 30% rh (blue), at 25 °C and 37% rh (orange), and 85 °C and 30% rh (green) from DWM, fits are with thermally activated, nucleation-limited switching (TA-NLS, solid line) [131]*, Ishibashi-Orihara (I-O, dashed line)* [126] *and DU-Chen (dotted line)* [128] *model; b) temperature dependent coercive field, measured at 0.2 Hz (rise time= 0.625 s). Error bars result from gaussian fits to the switching peak and therefore underestimate the total error.*

Fit parameters are:

Freq, 25 °C, 30 % rh

TA-NLS: w_b=1585 ± 100 µeV/nm^3, V=693 ±59 nm^3, E=w_b*V=1.098 ± 0.116 eV

I-O: C=0.4351 ± 0.0083 V/µm, d=0.548 ± 0.064

Du-Chen: f_0=88 ± 81 Hz; B=(5.88 ± 0.52)*10^{-5} V/(m* J$^{0.5}$)

Freq, 25 °C, 37 % rh

TA-NLS: w_b=2194 ± 47 µeV/nm^3, V=429 ±13 nm^3, E=w_b*V=0.941 ± 0.034 eV

I-O: C=0.3603 ± 0.0123 V/µm, d=0.701 ± 0.046

Du-Chen: f_0=2000 ± 1200 Hz; B=(6.77 ± 0.65)*10^{-5} V/(m* J$^{0.5}$)

Freq 85°C

TA-NLS: w_b=1889 ± 87 µeV/nm^3, V=603 ±34 nm^3, E=w_b*V=1.139 ± 0.083 eV

I-O C=0.3205 ± 0.0020 V/µm, d=1.103 ± 0.081

Du-Chen: f_0=13.7 ± 6.7 Hz; B=(3.63 ± 0.32)*10^{-5} V/(m* J$^{0.5}$)

Temp

TA-NLS 20-60 °C: w_b=569 ± 7 µeV/nm^3, V=1070 ±69 nm^3, E=w_b*V=0.609 ± 0.040 eV

TA-NLS 70-90 °C: w_b=432 ± 18 µeV/nm^3, V=2475 ±610 nm^3, E=w_b*V=1.07 ± 0.28 eV

Du-Chen: f_0=9.86 ± 50339549.83 Hz; B=1.39e-05 ± 19.5223737 V/(m* J$^{0.5}$), the error is several orders of magnitude higher than the fit-value indicating the bad fit

In all cases TA-NLS fits the data best (lowest χ^2_{red}).

K. Long-term-DC-measurements

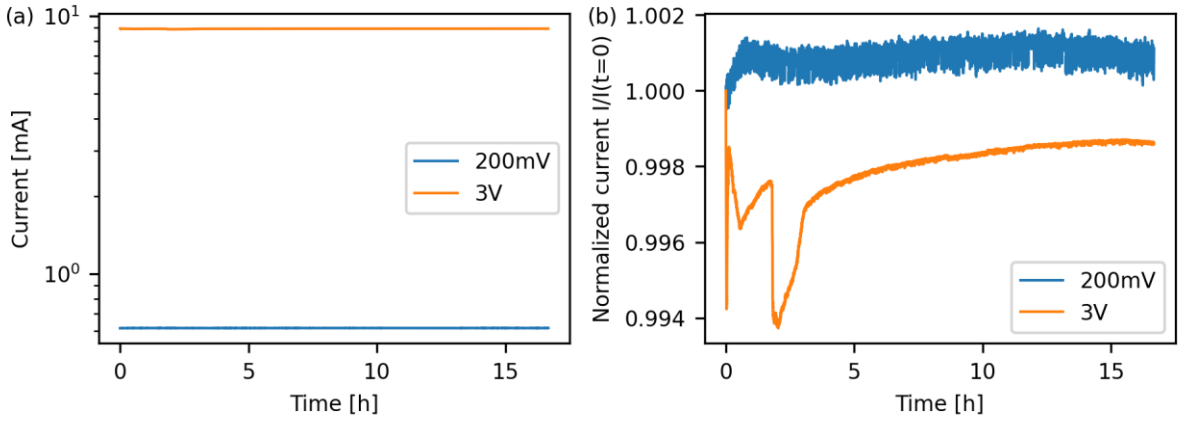

Appendix 21: Long-term current measurements at voltages below (200mV) and above (3V) the voltage needed to reduce water (≈1.5 V). (a) Shows the absolute value over time, while (b) shows the relative changes. The observed minimal changes (<1%) are attributed to Joule heating in the beginning and then minor changes in ambient conditions over the measurement period.

L. Integrated CV-loops

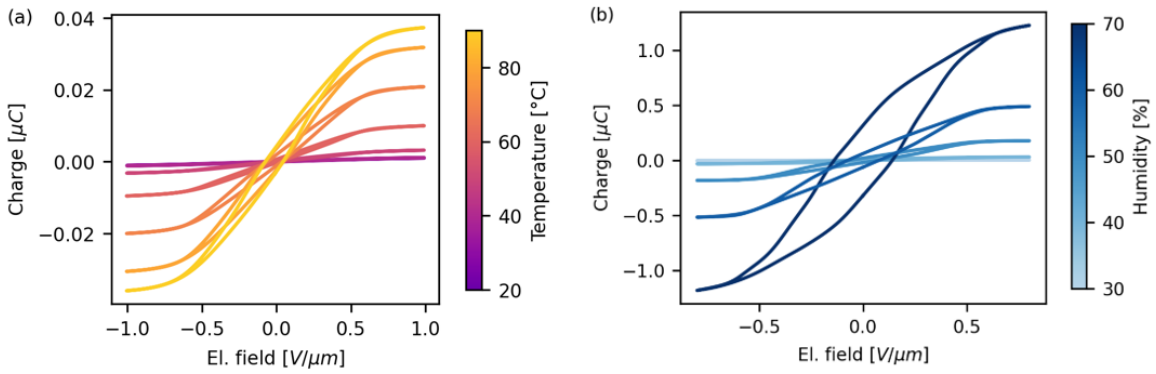

Appendix 22: a) integrated, temperature-dependent CV-loops, b) integrated, humidity-dependent CV-loops.

M. Measurements below 25%rh

Below approx. 25% rh the measurements did not show ferroelectricity around room temperature (Appendix 23), above ~60 °C clear signs of ferroelectricity reappeared (Appendix 24).

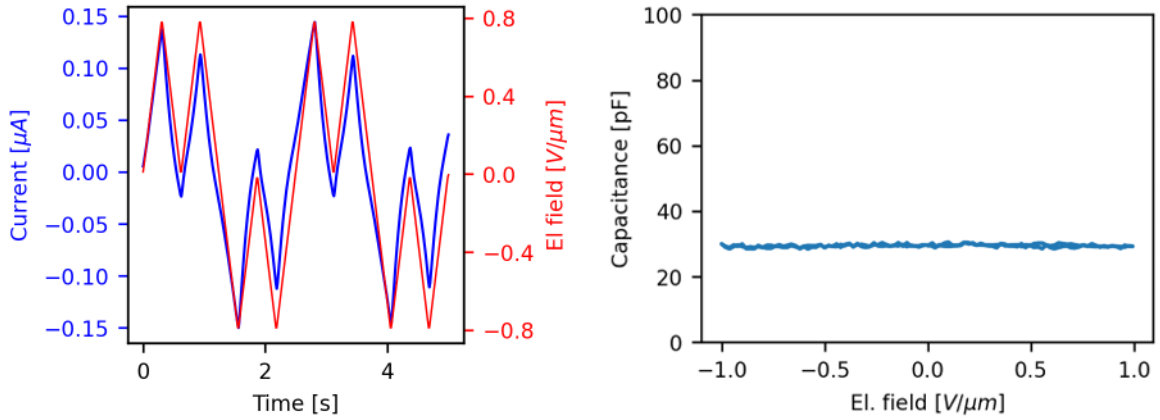

Appendix 23: Room temperature a) DW and b) CV measurement at 19% rh, showing no signs of ferroelectricity.

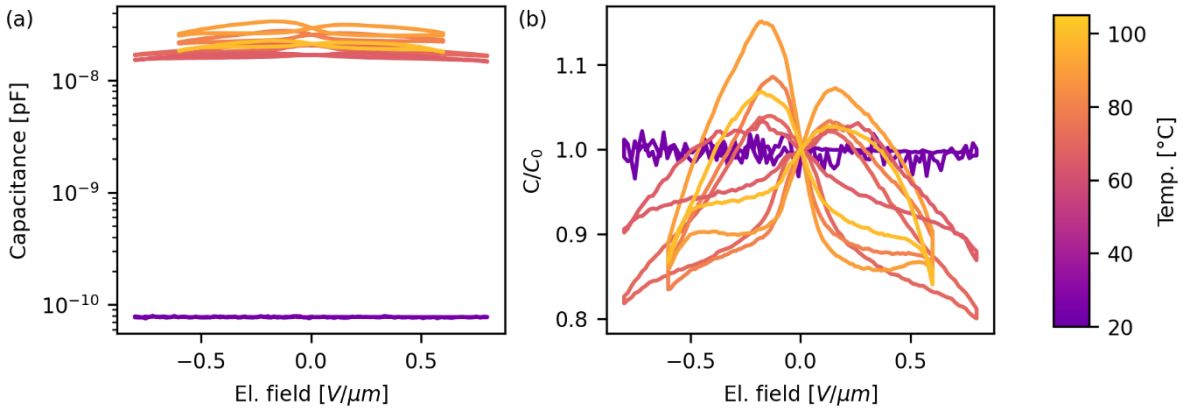

Appendix 24: CV-measurements in vacuum at 23 °C and above 60 °C. a) absolute values and b) relative changes

N. Alternative switching mechanisms

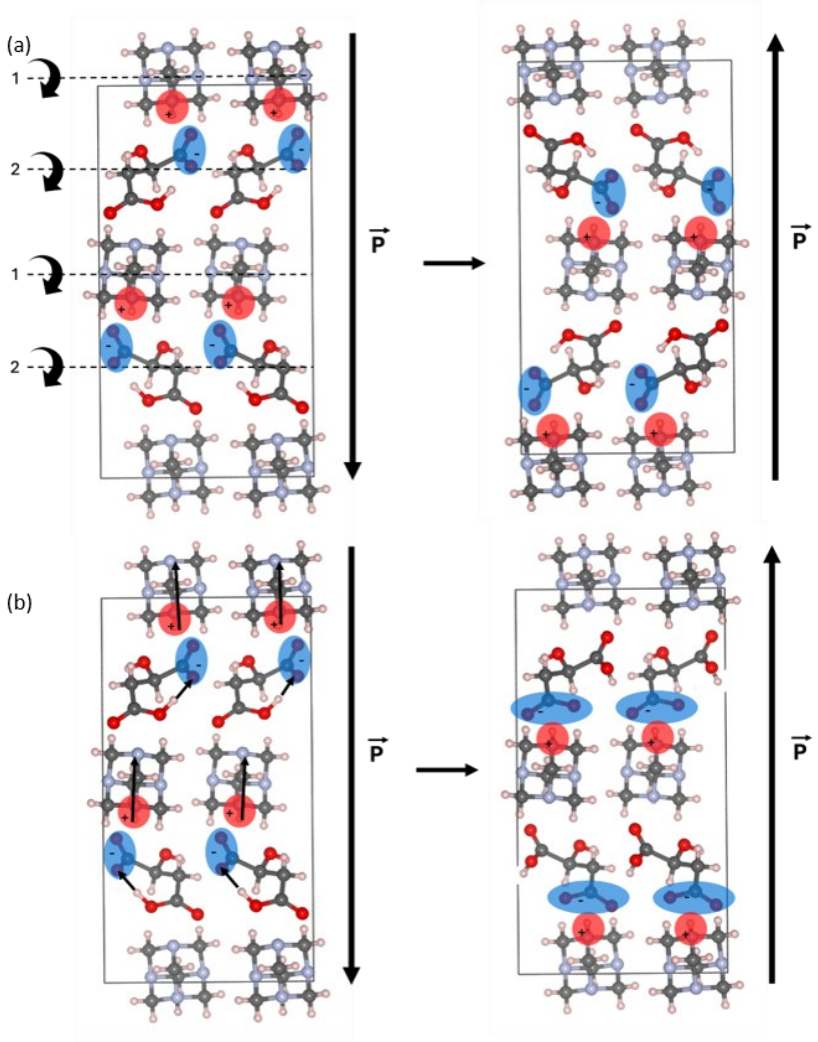

Appendix 25: Alternative switching mechanisms. a) fully rotational. Here, both molecules rotate by 180°, the charged areas (marked in blue and red) follow the rotation and do not change in any other way. It is unclear how this mechanism would depend on humidity and as such, it does not explain the importance of ambient humidity; b) fully proton-transfer. The molecules do not move, only protons change their position, which is marked by arrows. This changes the charged regions which are marked in blue and red but does not lead to full inversion of the unit cell.